Efficient electronic structure methods applied to metal nanoparticles

Ask Hjorth Larsen

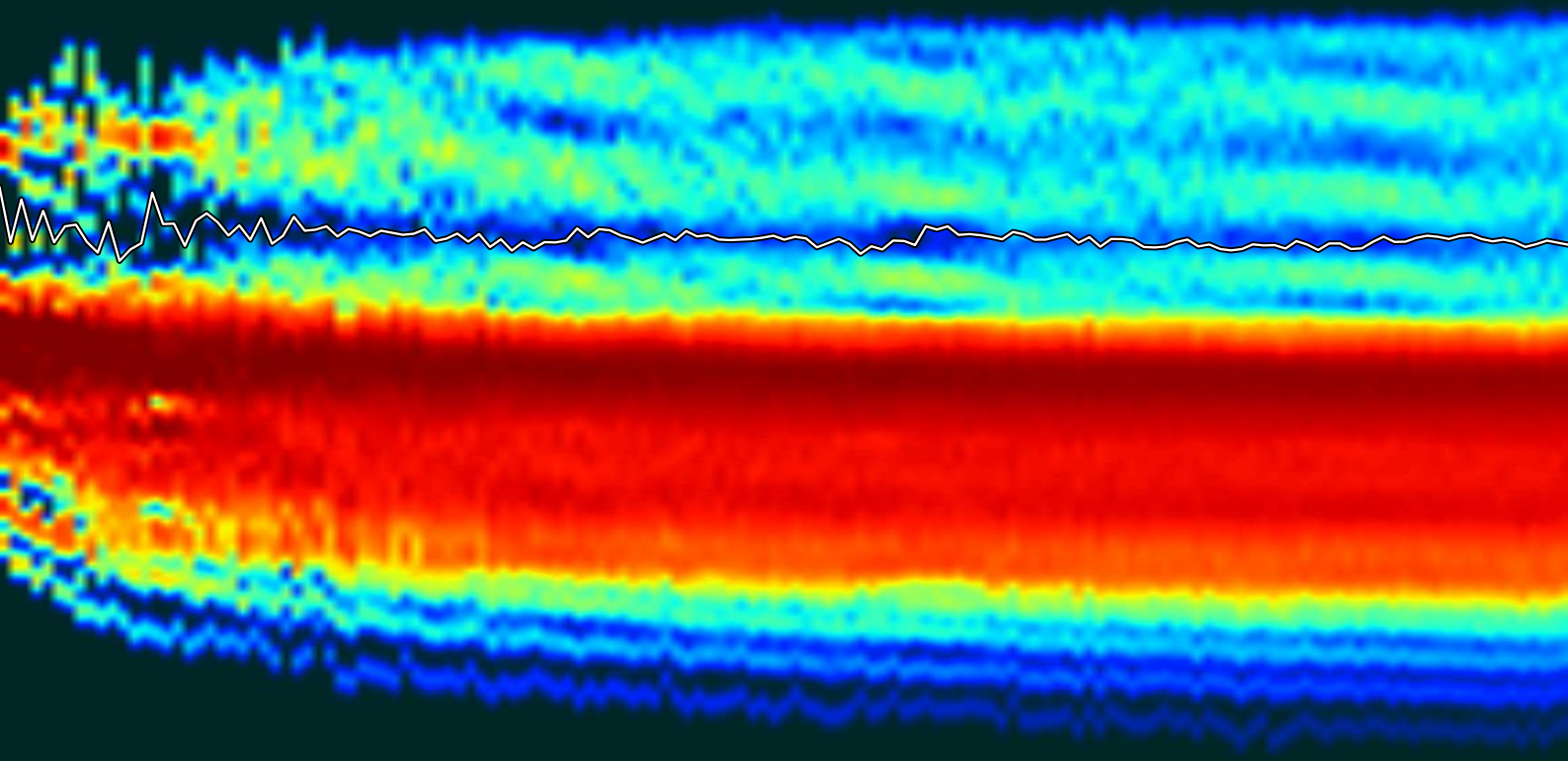

Ph.D. Thesis

Center for Atomic-scale Materials Design
Department of Physics
Technical University of Denmark

February 2012,

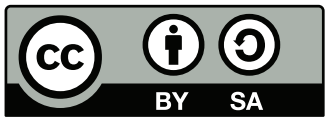

Front cover: A visualization of the distribution of electronic energy levels of gold clusters as a function of number of atoms (6–150 atoms on the horizontal axis) and energy (vertical axis). The line is the energy level such that all states with lower energy are filled. See also Figure 10.4. The 20-atom gold cluster, a tetrahedron, is displayed below.

Abstract

Nano-scale structures are increasingly applied in the design of catalysts and electronic devices. A theoretical understanding of the basic properties of such systems is enabled through modern electronic structure methods such as density functional theory. This thesis describes the development of efficient approaches to density functional theory and the application of these methods to metal nanoparticles.

We describe the formalism and implementation of localized atom-centered basis sets within the projector augmented wave method. Basis sets allow for a dramatic increase in performance compared to plane-wave or real-space methods, but sacrifice accuracy in doing so. This approach is implemented in the GPAW code where it complements the existing real-space approach. For both the real-space and basis set methods we implement parallel code to adapt GPAW for large-scale calculations on the BlueGene/P architecture.

Real-space calculations are performed to investigate the convergence of chemical properties of Au and Pt clusters toward the bulk limit. Specifically we study chemisorption of O and CO on cuboctahedral clusters up to 1415 atoms using up to 65536 CPU cores. Small clusters almost universally bind more strongly than large ones. This can be understood mostly as a geometric effect. Convergence of chemisorption energies within 0.1 eV of bulk values happens at about 200 atoms for Pt and 600 atoms for Au. Particularly for O on Au, large variations due to electronic effects are seen for smaller clusters.

The basis set method is used to study the electronic effects for the contiguous range of clusters up to several hundred atoms. The s-electrons hybridize to form electronic shells consistent with the jellium model, leading to electronic "magic numbers" for clusters with full shells. Large electronic gaps and jumps in Fermi level near magic numbers can lead to alkali-like or halogen-like behaviour when main-group atoms adsorb onto gold clusters.

A non-self-consistent Newns–Anderson model is used to more closely study the chemisorption of main-group atoms on magic-number Au clusters. The behaviour at magic numbers can be understood from the location of adsorbate-induced states relative to the Fermi level.

The relationship between geometric and electronic effects in Au is studied by rough first-principles simulated annealings with up to 150 atoms. Non-magic clusters are found to deform considerably, reducing the total energy through the creation of gaps. Clusters larger than 100 atoms can elongate systematically by up to 15 %. This demonstrates a complex interdependence between electronic and geometric structure in a size regime which in most cases has been studied semiempirically.

Resumé

Strukturer i nanoskala finder i stigende grad anvendelse inden for design af katalysatorer og elektroniske enheder. En grundlæggende teoretisk forståelse af sådanne systemer muliggøres af moderne elektronstrukturmetoder såsom tæthedsfunktionalteori. Denne afhandling omhandler udviklingen af effektive metoder inden for tæthedsfunktionalteori samt anvendelsen af disse metoder på metalnanopartikler.

Vi beskriver formalismen og implementationen af lokaliserede atomare basissæt i PAW-metoden. Basissæt muliggør betydeligt hurtigere udregninger end planbølge- eller realrumsgittermetoder, dog på bekostning af beregningsnøjagtighed. Metoden implementeres i programmet GPAW, hvor den supplerer den eksisterende gittermetode. For både realrums- og basissætmetoden implementeres parallelle metoder med henblik på afvikling af store beregninger på BlueGene/P-arkitekturen.

Ved hjælp af gitterbaserede beregninger undersøges konvergensen af kemiske egenskaber for store Au- og Pt-klynger. Specifikt udregnes kemisorptionsenergier for O og CO på kuboktahedrale klynger med op til 1415 atomer ved brug af 65536 CPU-kerner. Små klynger binder næsten universelt stærkere end store, hvilket kan forstås som en primært geometrisk effekt. Kemisorptionsenergien konvergerer inden for 0,1 eV af krystalgrænsen ved henholdsvis 200 og 600 atomer for Pt og Au. Der ses særligt for O på Au store variationer for de mindre klynger, som kan henføres til elektroniske effekter.

Basissætmetoden bruges til at undersøge disse elektroniske effekter for en sammenhængende følge af klynger op til flere hundrede atomer. s-elektronerne hybridiserer i elektronskaller i overensstemmelse med jelliummodellen, og disse fører til elektroniske "magiske tal" for klynger med fyldte skaller. Store elektroniske gab og hop i Fermienergi ved magiske tal kan medføre alkali- eller halogenagtig opførsel, når hovedgruppeatomer binder til guldklynger.

Der formuleres en ikke-selvkonsistent Newns–Anderson-model, som bruges til nærmere at undersøge kemisorptionen af hovedgruppeatomer på magiske guldklynger. Opførslen kan forstås ud fra placeringen af adsorbatinducerede tilstande i forhold til Ferminiveauet.

Forholdet mellem geometriske og elektroniske effekter i guldklynger undersøges ved hjælp af simulerede afkølinger baseret på tæthedsfunktionalteori med grove parametre op til 150 atomer. Energien af ikke-magiske klynger mindskes gennem en betydelig deformation hvorved der åbnes et elektronisk gab. Klynger på mere end 100 atomer kan således systematisk deformere med op til 15 %. Dermed vises en kompleks gensidig afhængighed af elektronisk og geometrisk struktur i et størrelsesregime som ellers primært har været behandlet med semiempiriske metoder.

Preface

This thesis is submitted for the degree of Ph.D. from the Technical University of Denmark. The work presented herein was carried out at the Center for Atomic-scale Materials Design between September 2008 and October 2011, with the exception that work on the localized basis set implementation was commenced in 2007. I am grateful for the help of my supervisors Karsten Wedel Jacobsen and Kristian Sommer Thygesen. The many long and helpful discussions with Karsten Wedel Jacobsen are deeply appreciated. I would further like to thank Jesper Kleis, Jens Jørgen Mortensen and Marco Vanin with whom I have worked at different stages of this project. Thanks to Marco Vanin, Jess Wellendorff and Kenneth Nielsen for proofreading parts of the thesis.

List of papers

The below publications include results of the work presented in this thesis.

Paper I. Localized atomic basis set in the projector augmented wave method.

A. H. Larsen, M. Vanin, J. J. Mortensen, K. S. Thygesen, and K. W. Jacobsen.
Physical Review B, vol. **80**, p. 195112, 2009.

Paper II. Electronic structure calculations with GPAW: a real-space implementation of the projector augmented-wave method.

J. Enkovaara, C. Rostgaard, J. J. Mortensen, J. Chen, M. Dułak, L. Ferrighi, J. Gavnholt, C. Glinsvad, V. Haikola, H. A. Hansen, H. H. Kristoffersen, M. Kuisma, A. H. Larsen, L. Lehtovaara, M. Ljungberg, O. Lopez-Acevedo, P. G. Moses, J. Ojanen, T. Olsen, V. Petzold, N. A. Romero, J. Stausholm-Møller, M. Strange, G. A. Tritsaris, M. Vanin, M. Walter, B. Hammer, H. Häkkinen, G. K. H. Madsen, R. M. Nieminen, J. K. Nørskov, M. Puska, T. T. Rantala, J. Schiøtz, K. S. Thygesen, and K. W. Jacobsen.
Journal of Physics: Condensed Matter, vol. **22**, no. 25, p. 253202, 2010.

Paper III. Finite size effects in chemical bonding: From small clusters to solids.

J. Kleis, J. Greeley, N. Romero, V. Morozov, H. Falsig, A. Larsen, J. Lu, J. Mortensen, M. Dułak, K. Thygesen, J. Nørskov, and K. Jacobsen.
Catalysis Letters, vol. **141**, pp. 1067–1071, 2011. 10.1007/s10562-011-0632-0.

Paper IV. Electronic shell structure and chemisorption on gold nanoparticles.

A. H. Larsen, J. Kleis, K. Thygesen, J. Nørskov, and K. W. Jacobsen.
Submitted.

Paper V. In situ XAS of Pt monolayer model fuel cell catalysts: balance of nanostructure and bimetallic interactions.

D. Friebel, D. J. Miller, T. Anniyev, H. Ogasawara, V. Viswanathan, A. H. Larsen, C. P. O'Grady, J. Nørskov, and A. Nilsson.
In preparation.

Contents

Part I

Computational methods in quantum mechanics

Chapter 1

Introduction

This thesis concerns the chemical properties of metal nanoparticles and the development of theoretical methods to describe them. In this work, a *nanoparticle* or *cluster* refers to an assembly of a few to a few thousand atoms of a chemical element which would normally form a bulk crystalline phase. A typical size of such a particle may be a few nanometres, small enough that quantum mechanical effects cause the particle to behave differently from the bulk material.

With modern computers and numerical methods it is possible to predict the behaviour of quantum mechanical systems using *ab initio* methods such as density functional theory (DFT).[1,2] The term ab initio or *first principles* signifies that a method is based on solving fundamental physical equations such as the Schrödinger equation. For systems with more than a few particles, the Schrödinger equation itself is too computationally demanding to solve directly, and computational methods must rely on a range of reformulations and approximations to make computations tractable. We describe one such approach, where an atomic orbital basis set is combined with the projector augmented wave method.[3,4] This approach is implemented in GPAW, an electronic structure code based on a more accurate but also more computationally expensive real-space representation of wavefunctions.[5–7] The localized basis set is similar to the SIESTA code, with the difference that SIESTA is based on simpler norm-conserving pseudopotentials.[8,9] The combination in GPAW of the high-performance localized basis set with the more accurate real-space method provides a number of advantages. In particular, the basis set is useful for calculating structures efficiently, while the real-space code can be used to evaluate binding energies which are less accurate with the basis set. The basis set is also useful for applications that mathematically emphasize a finite or localized basis set. For example the basis set is now used for Green's function based electron transport calculations.[10] Another development for the GPAW code is the parallelization of the real-space code for massively parallel calculations. The main advantage of real-space methods is the ability to parallelize over many quantities at the same time, which allows the calculations to scale efficiently up to thousands of processors.

The second part of this thesis applies these methods with the main objective of understanding the chemical behaviour of nanoparticles, focusing on gold. Gold is normally thought of as inert, but this really applies to *bulk* gold. The chemistry of gold is in fact extremely diverse.[11–13] Due to the large nuclear

charges, core electrons of the late transition metals exhibit relativistic behaviour, which alters the electrostatic screening felt by the remaining electrons. The relativistic effects lead to a contraction of the s electrons compared to d electrons, which in the end is responsible for most of the unusual properties of gold.[14–16] These relativistic effects, along with the full d-shell which places less energetic emphasis on atomic packing, cause gold clusters to form structures that differ not only from those of other late transition metal clusters, but also those of the other noble metals.[17] Small gold clusters of different size have been predicted to form a large variety of structures including flakes and cages.[18,19] A significant electronic effect of gold clusters is the organization of the s-electrons into global electronic shells that extend over the entire cluster. Such shell structure is found in many free-electron-like materials, particularly the alkali metals, and gives rise to electronic *magic numbers* where clusters have increased stability and large electronic gaps.[20–23] Many properties of clusters depend sensitively on the electronic shell structure including their chemistry.[24] However, limitations in available computational power has prevented thorough modelling of larger clusters.

The efficiency of the localized basis set allows us to study, at modest computational cost, such effects for contiguous ranges of typically 20–200 atoms. We find that large size-dependent variations in binding energy are associated with the shell structure of gold clusters. These calculations are performed for many different adsorbates, and comparisons are made between clusters of several different metals. A recurring theme in these calculations is the study of overall trends from large numbers of systems, although this happens at the sacrifice of accuracy of the individual calculations. This is probably the first computational study from first principles of such large ensembles of systems.

The thesis is structured as follows.

- Chapter 2 gives a brief introduction of computational methods in quantum theory, including density functional theory which practically all results in this work are based on.
- Chapter 3 describes the projector augmented wave method and the mathematical formalism of the atomic basis set expansion. An initial implementation was written in cooperation with Marco Vanin and documented in Refs. 25, 26, although many further developments have taken place since.
- The generation of basis functions from atomic reference calculations is described in Chapter 4 along with other issues of practical interest to basis sets.
- Chapter 5 discusses the efficiency and parallelization of the basis set code, and explains the implementation of some of the more important steps in a calculation. Performance benchmarks are included. Adaptation of the real-space code for massively parallel calculations is further described.
- Chapter 6 acts as an introduction to Part II of this thesis, wherein the properties of nanoparticles are investigated. Brief descriptions are given of the geometric structures of clusters and relevant theoretical methods.
- Large-scale DFT calculations of adsorption of O and CO on Au and Pt clusters with up to 1415 atoms are presented in Chapter 7, and the effect of facet size is discussed.

- The effect of electronic shell structure on the chemistry of clusters, focusing on gold, is studied in detail in Chapter 8 by considering adsorption of a range of adsorbates.
- In Chapter 9 a non-selfconsistent Newns–Anderson model is used to analyze the bonding of several adsorbates using Hamiltonian matrices obtained from DFT calculations.
- In Chapter 10, gold cluster structures are optimized using simulated annealing with simple EMT and DFT.
- Chapter 11 summarizes and concludes the work.

Chapter 2

Theoretical methods

This chapter gives a brief review of quantum mechanics from the perspective of computationally predicting the properties of an interacting system of electrons and nuclei.

2.1 Quantum mechanics

The properties of matter at small scales are described by the Schrödinger equation. For a system with N particles, the (time-independent) Schrödinger equation is a differential equation for the *many-body wavefunction* $\Psi(\mathbf{r}_1, \mathbf{r}_2, \ldots, \mathbf{r}_N)$ with a total of $3N$ spatial parameters, and this function entirely characterizes the system. The storage required to explicitly represent such an object in a computer is therefore exponential in the number of particles, making numerical calculations in this form impossible beyond a small number of particles. This is commonly referred to as the "exponential wall".[27] Computational approaches to quantum mechanics are therefore generally based on methods that recast the Schrödinger equation into more tractable forms by applying several approximations.

Because of the large ratio between electronic and nuclear masses, electrons and nuclei exhibit quantum mechanical behaviour on different length and time scales. The Born–Oppenheimer approximation assumes that the wavefunction of a combined electronic and nuclear system can be expressed as a product of an electronic and a nuclear wavefunction. Going one step further, the nuclei can for most purposes be assumed to behave like classical point particles. This reduces a quantum mechanical calculation to a purely electronic problem, which will be the subject of the next several sections.

2.2 The Hartree–Fock method

Electrons are by the symmetrization postulate *fermions*, meaning that electronic wavefunctions are antisymmetric with respect to the interchange of any two position variables $\mathbf{r}_i$ and $\mathbf{r}_j$. From any set of orthogonal single-particle states, an appropriately antisymmetric many-body wavefunction can be formed as a *Slater determinant* from the single-particle states. Any many-body wavefunction can be written as a linear combination of such determinants. In the

Hartree–Fock method it is assumed that the many-body wavefunction can be written as a single such determinant. This assumption leads to a set of equations, the Hartree–Fock equations, for each single-particle state minimizing the total energy. These equations can be solved numerically by iteratively adjusting wavefunctions and potential until obtaining self-consistent single-particle states and potential.

In the Hartree–Fock method, the electronic interaction energy can be understood as being comprised of two terms: the *direct* or *Hartree* term, and the *exchange* term. The Hartree term is the Coulomb energy of the full charge density, so it incorporates the Coulomb repulsion of every electron with every electron. Clearly, each electron interacts with every *other* electron, but not with the specific part of the charge distribution that it itself contributed. One term in the exchange contribution can be understood as a correction which compensates for this self-interaction part in the Hartree energy. The exchange term as a whole is a manifestation of Pauli exclusion.

While the Hartree–Fock approach is suited for numerical calculations, it is still an approximate many-body method. As mentioned, a general many-body wavefunction must be described as a linear combination of multiple Slater determinants. Any discrepancy between exact Hartree–Fock theory as compared to a full linear combination of Slater determinants, which yields the exact many-body wavefunction, is somewhat vaguely called *correlation*. Methods that improve on Hartree–Fock theory through various ways to include correlation are called *post-Hartree–Fock methods*. Within these methods, accuracy generally comes at the price that the computational cost scales with high powers of the number of electrons, and so these accurate methods are limited to small systems.

2.3 Density functional theory

Density functional theory (DFT) is an approach to solving the many-body problem using the electron density instead of the many-body wavefunctions. DFT evolved from the Thomas–Fermi theory, a more intuitive approach; Hohenberg and Kohn later developed the concept as a formally correct many-body method.[1]

The foundation of DFT is the insight that the ground-state electron density $n(\mathbf{r})$ of an electronic system is sufficient to entirely characterize that system. Thus any property which can be derived from the many-body wavefunction can in fact be derived knowing only the ground-state density. The total energy of a system of interacting electrons in a potential can be expressed as a functional of the electron density, and the ground-state density variationally minimizes this functional. All one has to do is, in principle, to perform such a minimization. This turns out to be tricky, since it is not known how to evaluate quantities such as the energy directly from an electron density without first using it to calculate the wavefunctions.

Kohn and Sham suggested an approach to solve this problem by introducing a fictional system of non-interacting particles represented by single-particle wavefunctions in a shared *effective potential*.[2] In this picture the potential must account for all interactions. Subject to a few representability issues, such as whether the true ground-state electron density *can* be expressed from single-particle wavefunctions, a universal form of the effective potential can be shown to exist which makes the method formally exact. Explicit expressions for phys-

ical quantities can then be written down in terms of the Kohn–Sham wavefunctions and the electron density, such as the energy:

$$E_{\mathrm{KS}} = \sum_n f_n \langle \psi_n | \hat{T} | \psi_n \rangle + \iint \frac{\rho(\mathbf{r})\rho(\mathbf{r}')}{\|\mathbf{r} - \mathbf{r}'\|} \,\mathrm{d}\mathbf{r}\,\mathrm{d}\mathbf{r}' + E_{\mathrm{xc}}[n]. \tag{2.1}$$

Here the energy is split into three terms. The first term is the single-particle kinetic energy of the Kohn–Sham states $|\psi_n\rangle$ weighted by their occupation numbers f_n. The second term is the Coulomb energy of the total charge distribution $\rho(\mathbf{r})$ in the system, including the electron density and the nuclear point charges. The third term $E_{\mathrm{xc}}[n]$ is a density functional which must describe the effect of the particle interactions otherwise neglected in the single-particle picture, and should therefore account for exchange, as considered in Hartree–Fock theory, and correlation. It is called the *exchange–correlation* (XC) functional. No one knows the true XC functional, and so it is generally approximated. This is a fundamental point of DFT as it is the only "uncontrolled" approximation.

From the energy expression one can, similarly to the Hartree–Fock method, derive a variational equation for the Kohn–Sham states. These Kohn–Sham equations can then be solved on a computer using an iterative procedure. Roughly speaking this involves choosing an initial electron density and repeating three steps:

- Calculate potential from density
- Calculate wavefunctions from potential by solving Kohn–Sham equations
- Calculate density by occupying the states with lowest energy

The procedure stops when density, potential and wavefunctions are self-consistent, in the sense that things no longer change on every iteration. At that point one has obtained the true ground-state density and energy of the system, at least if using the exact XC functional.

2.4 Exchange–correlation functionals

As previously mentioned, there exists a general XC density functional which makes the Kohn–Sham approach exact. No one knows what the exact functional looks like, so it is instead approximated.

A natural starting point for such an approximation is the homogeneous electron gas, which is entirely characterized by the constant density. In this simple case the exchange and correlation functional can be obtained. This case leads to the local density approximation (LDA): The assumption that each point in space contributes an XC energy which depends only on the density $n(\mathbf{r})$ in that point, and that this energy is the same as that of an electron gas with the same density.

A better approximation can be obtained by extending the LDA so that each point contributes an amount to the energy depending both on the value and the gradient of the density in that point. These approximations are called generalized gradient approximations (GGAs). The most widely used one is probably the Perdew–Burke–Ernzerhof (PBE) functional.[28]

A modification of the PBE functional, RPBE, is specifically designed to provide a better description of metal surfaces and adsorption (at the expense of a slightly worse description of bulk metals).[29] Throughout this work, calculations generally employ the RPBE functional.

2.5 Pseudopotentials

For all except the smallest atoms, electrons can be divided into tightly bound *core* states and loosely bound *valence* states. The strong Coulomb attraction from the nucleus localizes the core states so that they do not interact much with states on other atoms. Core states are therefore not essential to a numerical description of chemistry. However the valence states must be orthogonal to the core states, and therefore oscillate rapidly within the core region. Such oscillations are shown on Figure 2.1 for the 4s atomic orbital of iron (black line). The accurate representation of core states and oscillatory valence states in terms of real-space grids or plane-waves is expensive, and unnecessary in the sense that the chemical properties of an atom depend mostly on the behaviour of electrons far from the nucleus. *Pseudopotential* methods deal with this problem by replacing the steep potential of the nuclei as well as the core electrons with a smooth effective potential felt by the valence electrons. The exclusion of core states from the calculation procedure is called the *frozen core approximation*. Within the smooth potential, the oscillatory behaviour of valence states can be eliminated, resulting in smooth, nodeless *pseudowavefunctions* which are cheap to represent numerically. This is shown for the HGH pseudopotentials[30] on Figure 2.1 (green). The pseudowavefunctions are identical to the real ("all-electron" or AE) wavefunctions far from the nucleus, but are replaced by smooth functions close to it.

Clearly the pseudopotential approach makes sense only if it can be guaranteed that the pseudopotentials accurately reflect the behaviour of real atoms. A common way to do this is to add *Kleinman–Bylander projectors* to the Hamiltonian.[31] These are fixed functions which, by their scalar products with the pseudowavefunctions, adjust the energy of different states depending on their angular momentum and radial structure. These can be chosen to ensure that the atomic states have the correct energies and response to perturbations. The latter ensures better transferability of the pseudopotential between different systems.[32] While the pseudopotential approximation is conceptually simple, the generation of good pseudopotentials can be quite complicated due to the large number of parameters involved.[33]

There are two main kinds of pseudopotentials: norm-conserving and more recently "ultrasoft". With norm-conserving pseudopotentials it is expensive to represent highly localized states, such as the d-states of transition metals. From the figure, the 3d pseudowavefunction is significantly less smooth than the 4s one because the 3d state must be normalized to contain one electron. Ultrasoft pseudopotentials avoid the norm-conservation restriction through more complicated mathematics.[34] This allows smooth wavefunctions to be used also for localized states. The projector augmented wave method (red curves on Figure 2.1) is similar to ultrasoft pseudopotentials, but uses a transformation to also retain the all-electron information, thus eliminating pseudopotential transferability errors.

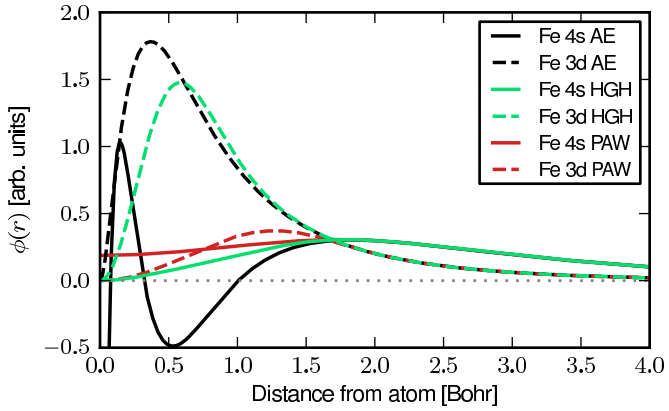

Figure 2.1: *Pseudopotential approaches for the 4s and 3d valence states of iron. Atomic orbitals (black) are replaced by smooth, norm-conserving pseudowave-functions (green). Localized states such as the 3d state can be made more smooth by ultrasoft pseudopotentials or the projector augmented wave method (red).*

2.6 Basis sets

To perform a DFT calculation one must choose a representation of the Kohn–Sham states, and this choice has significant implications on performance.

One way is to expand the wavefunctions as linear combinations of plane-waves, then variationally optimize the coefficients. Plane-waves are economical in the sense that relatively few plane-waves can represent a typical wavefunction well. Plane-waves are also complete, and a single parameter, namely the energy cutoff, can be used to control the quality of the basis set without any upper limit on precision. The number of plane-waves is generally large enough that iterative methods must be employed to solve the Kohn–Sham equations.[35] A disadvantage of plane-waves methods is that each plane-wave overlaps with atoms no matter their distance. Fast Fourier transforms, an integral element of plane-wave methods, are known to parallelize poorly, limiting the number of processors that can efficiently contribute to the same calculation.

More scalable methods must rely on localization to some extent. GPAW normally uses real-space grids to represent the wave-functions. These require significantly more memory than a plane-wave basis of equivalent quality, but are well suited for parallelization.[5,6] This allows efficient division of the system into spatial domains, with limited communication between adjacent domains. The real-space representation is similar to plane-waves since its quality can increased to any desired precision by reducing the grid spacing.

A different approach is to use atomic basis sets, where a limited set of fixed basis functions is assigned to each atom. Each function is chosen carefully so only few basis functions are required to represent the wavefunctions. This greatly speeds up the solution of the Kohn–Sham equations, and several operations which scale quadratically in plane-wave or real-space methods will scale linearly due to the localization of the basis functions. The main disadvantage of basis set approaches is that no single parameter can practically control the

accuracy, and the precision can only approach that of plane-wave or real-space methods. Atomic basis sets can be based on numerical atomic orbitals (NAO), where the actual orbitals are sampled on a grid and used as basis functions. They can also be based on simple analytic functions such as Gaussians or exponentials; commonly referred to as Gaussian-type orbitals (GTO) and Slater-type orbitals (STO). The advantage of such methods is that matrix elements can be calculated analytically, although more basis functions are needed than with NAO-based approaches.

The specific subject in the following is the implementation of a basis set of numerical atomic orbitals in GPAW, based on the projector augmented wave method.

Chapter 3

The projector augmented wave method

One of the main developments discussed in this thesis is the use of localized atomic orbitals as a basis set to describe electronic wave functions within the projector augmented wave method (PAW). In the light of the brief review in the previous chapter, it should be clear how this combination fits among the existing methods. A more complete and technical derivation of this specific method is given in this chapter.

The PAW method by Blöchl[3,4] is an approach to solving the Kohn-Sham equations which is based on a transformation $\hat{\mathcal{T}}$ between smooth, computationally convenient pseudowavefunctions $|\tilde{\psi}_n\rangle$ and the rapidly oscillating all-electron wavefunctions $|\psi_n\rangle$:

$$|\psi_n\rangle = \hat{\mathcal{T}}\,|\tilde{\psi}_n\rangle\,. \tag{3.1}$$

Numerical calculations are performed using the pseudowavefunctions $|\tilde{\psi}_n\rangle$, while the transformation $\hat{\mathcal{T}}$ ensures that the all-electron information is retained. This makes PAW calculations in many ways similar to ultrasoft pseudopotentials,[36] while PAW is in fact an all-electron method.

3.1 Transformation operator

The transformation operator $\hat{\mathcal{T}}$ is defined as the identity operator plus a local contribution around each atom a. It is defined to map a set of chosen smooth functions $|\tilde{\phi}_i^a\rangle$ for each atomic valence state i to the all-electron eigenstates $|\phi_i^a\rangle$:

$$\hat{\mathcal{T}} = \hat{1} + \sum_{ai} (|\phi_i^a\rangle - |\tilde{\phi}_i^a\rangle)\,\langle\tilde{p}_i^a|\,. \tag{3.2}$$

The functions $|\phi_i^a\rangle$ and $|\tilde{\phi}_i^a\rangle$ are called all-electron partial waves and pseudo partial waves, respectively. They are chosen to be equal outside a certain radius of a, so that the PAW transformation as a whole has no effect in regions far from atoms. The functions $\langle\tilde{p}_i^a|$ are Kleinman–Bylander projectors. They are localized, and the region in which they are nonzero is called the *augmentation*

region. Together with the pseudo partial waves they should form a complete orthonormal basis within this region:

$$\sum_i \langle \mathbf{r}|\tilde{\phi}_i^a\rangle \langle \tilde{p}_i^a|\mathbf{r}'\rangle = \delta(\mathbf{r}-\mathbf{r}') \quad \text{where} \quad \langle \tilde{p}_i^a|\tilde{\phi}_j^a\rangle = \delta_{ij}. \tag{3.3}$$

As an all-electron method, the PAW method is exact if projectors and partial waves form a complete basis around each atom, and the augmentation regions of distinct atoms do not overlap.*

3.2 Atomic corrections and expectation values

The expectation value of a local operator $\hat{O}$ can be written in terms of the pseudowavefunctions by inserting the PAW transformation (3.2) and industriously applying the completeness relation (3.3). Eventually

$$\begin{aligned}\langle \hat{O}\rangle &= \sum_n f_n \langle \tilde{\psi}_n|\hat{\mathcal{T}}^\dagger \hat{O}\hat{\mathcal{T}}|\tilde{\psi}_n\rangle \\ &= \sum_n f_n \langle \tilde{\psi}_n|\hat{O}|\tilde{\psi}_n\rangle + \sum_{aij}\left(\langle \phi_i^a|\hat{O}|\phi_j^a\rangle - \langle \tilde{\phi}_i^a|\hat{O}|\tilde{\phi}_j^a\rangle\right) D_{ji}^a + O_{\text{core}}\end{aligned} \tag{3.4}$$

where

$$D_{ji}^a = \sum_n \langle \tilde{p}_j^a|\tilde{\psi}_n\rangle f_n \langle \tilde{\psi}_n|\tilde{p}_i^a\rangle \tag{3.5}$$

are called *atomic density matrices*. The first term in (3.4) involves only the pseudowavefunctions and can be calculated efficiently with real-space grids or plane-waves. The second term involves the fixed atomic quantities $\langle \phi_i^a|O|\phi_j^a\rangle$ and $\langle \tilde{\phi}_i^a|O|\tilde{\phi}_j^a\rangle$. These calculations involve the rapidly oscillating all-electron wavefunctions, but they can be performed in a spherical coordinate system and stored once and for all for each type of atom. The only quantities in the second and third terms which depend on the system are D_{ij}^a. The scalar products $\langle \tilde{p}_i^a|\tilde{\psi}_n\rangle$ are cheap to evaluate since the projectors are localized, and since both functions are smooth. The last term in (3.4) is an extra, fixed contribution O_{core} due to the frozen core states.

The important implication of expression (3.4) is that the calculations are divided into an extended *pseudo*-part suitable for grid or plane-wave representations, which will account for most computational cost associated with the method, coupled to a set of constant, pre-evaluated *atomic corrections* only through the atomic density matrices D_{ij}^a. Most importantly the electron density is decomposed as

$$n(\mathbf{r}) = \tilde{n}(\mathbf{r}) + \sum_a n^a(\mathbf{r}-\mathbf{R}^a) - \sum_a \tilde{n}^a(\mathbf{r}-\mathbf{R}^a), \tag{3.6}$$

*Usually a couple of projectors are used for each atomic valence state. The necessary additional all-electron partial waves can be generated by radially integrating the atomic Kohn–Sham equations using an energy which is not an eigenvalue.

where

$$\tilde{n}(\mathbf{r}) = \sum_n f_n \langle \tilde{\psi}_n | \mathbf{r} \rangle \langle \mathbf{r} | \tilde{\psi}_n \rangle + \sum_a \tilde{n}_c^a(\mathbf{r} - \mathbf{R}^a), \tag{3.7}$$

$$n^a(\mathbf{r}) = \sum_{ij} \langle \phi_i^a | \mathbf{r} \rangle \langle \mathbf{r} | \phi_j^a \rangle D_{ji}^a + n_c^a(\mathbf{r}), \tag{3.8}$$

$$\tilde{n}^a(\mathbf{r}) = \sum_{ij} \langle \tilde{\phi}_i^a | \mathbf{r} \rangle \langle \mathbf{r} | \tilde{\phi}_j^a \rangle D_{ji}^a + \tilde{n}_c^a(\mathbf{r}). \tag{3.9}$$

Here an arbitrary pseudo-core density $\tilde{n}_c^a(\mathbf{r})$ has been included in (3.7) which is cancelled by the atomic correction (3.9).

3.3 Compensation charges

A recurring feature in the PAW method is the addition of something to a quantity, which is cancelled out by subtracting the atomic expansion of the same quantity. The reason for doing so is to make the wavefunctions, density and potential as smooth and well-behaved as possible. In this way, *compensation charges* $\tilde{Z}(\mathbf{r})$ are added around each atom to the charge distribution to eliminate the direct electrostatic interaction between atoms in favour of having a single smooth charge distribution which can be treated on a grid. Considering again the Kohn–Sham energy expression, the charge density is the sum

$$\rho(\mathbf{r}) = n(\mathbf{r}) + Z(\mathbf{r}) \tag{3.10}$$

of the all-electron density $n(\mathbf{r})$ and the atomic point charges $Z(\mathbf{r})$. The compensation charges are used to regroup the charge into two neutral distributions

$$\rho(\mathbf{r}) = \tilde{\rho}(\mathbf{r}) + \underbrace{\sum_a \rho^a(\mathbf{r} - \mathbf{R}^a) - \sum_a \tilde{\rho}^a(\mathbf{r} - \mathbf{R}^a)}_{\text{neutral}}, \tag{3.11}$$

such that the electrostatic singularities near the nuclei disappear in $\tilde{\rho}(\mathbf{r})$. The atomic charges are

$$\rho^a(\mathbf{r}) = n^a(\mathbf{r}) + Z^a(\mathbf{r}), \tag{3.12}$$

$$\tilde{\rho}^a(\mathbf{r}) = \tilde{n}^a(\mathbf{r}) + \tilde{Z}^a(\mathbf{r}). \tag{3.13}$$

Going one step further, the compensation charges are defined as a linear combination

$$\tilde{Z}^a(\mathbf{r}) = \sum_L Q_L^a \tilde{g}_L^a(\mathbf{r}) \tag{3.14}$$

of smooth localized functions $\tilde{g}_L^a(\mathbf{r})$ with real spherical harmonics $Y_L(\theta, \phi)$ as angular parts. L is a composite index for the usual angular indices (l, m). The coefficients Q_L^a are uniquely defined by requiring that the compensation charges must cancel out the multipole moments of the charges represented on radial grids. Thereby *all* electrostatic interactions between atoms are contained in $\tilde{\rho}(\mathbf{r})$ up to any chosen order. This makes the expansion coefficients Q_L^a a function of the atomic density matrices D_{ij}^a. A complete derivation is given by Rostgaard.[37]

3.4 Total energy

With these modifications, the total Kohn–Sham energy (2.1) can be written as three rather elaborate terms

$$E = \tilde{E} + \sum_a E^a - \sum_a \tilde{E}^a \tag{3.15}$$

with

$$\begin{aligned}\tilde{E} &= \sum_n f_n \langle \tilde{\psi}_n | \hat{T} | \tilde{\psi}_n \rangle + \frac{1}{2} \iint \frac{\tilde{\rho}(\mathbf{r}) \tilde{\rho}(\mathbf{r}')}{\|\mathbf{r} - \mathbf{r}'\|} \,\mathrm{d}\mathbf{r}\,\mathrm{d}\mathbf{r}' \\ &\quad + \sum_a \int \tilde{n}(\mathbf{r}) \bar{v}^a(\mathbf{r} - \mathbf{R}^a) \,\mathrm{d}\mathbf{r} + E_{\mathrm{xc}}[\tilde{n}], \end{aligned} \tag{3.16}$$

$$\begin{aligned}E^a &= \sum_{ij} \langle \phi_i^a | \hat{T} | \phi_j^a \rangle \, D_{ji}^a + \frac{1}{2} \iint \frac{\rho^a(\mathbf{r}) \rho^a(\mathbf{r}')}{\|\mathbf{r} - \mathbf{r}'\|} \,\mathrm{d}\mathbf{r}\,\mathrm{d}\mathbf{r}' \\ &\quad + E_{\mathrm{xc}}[n^a] + E_{\mathrm{kin}}^{\mathrm{core}}, \end{aligned} \tag{3.17}$$

$$\begin{aligned}\tilde{E}^a &= \sum_{ij} \langle \tilde{\phi}_i^a | \hat{T} | \tilde{\phi}_j^a \rangle \, D_{ji}^a + \frac{1}{2} \iint \frac{\tilde{\rho}^a(\mathbf{r}) \tilde{\rho}^a(\mathbf{r}')}{\|\mathbf{r} - \mathbf{r}'\|} \,\mathrm{d}\mathbf{r}\,\mathrm{d}\mathbf{r}' \\ &\quad + E_{\mathrm{xc}}[\tilde{n}^a] + \int \tilde{n}^a(\mathbf{r}) \bar{v}^a(\mathbf{r}) \,\mathrm{d}\mathbf{r}. \end{aligned} \tag{3.18}$$

Here $E_{\mathrm{kin}}^{\mathrm{core}}$ is the fixed kinetic energy of the frozen core states, and $\bar{v}^a(\mathbf{r})$ is an arbitrary localized potential which is "added and subtracted" similarly to compensation charges to make the total potential as smooth as possible. Note how the XC energy can be divided in this way only if it is assumed to be local, so that Eq. (3.4) applies. Non-local XC functionals can be incorporated but are considerably more complicated.[38]

A set of Kohn–Sham equations can be derived by requiring that the pseudowavefunctions should be simultaneously orthogonal and minimize the total energy, which will be done in the context of localized basis sets in the following.

3.5 Basis set formalism

The pseudowavefunctions $|\tilde{\psi}_n\rangle$ are expanded as linear combinations

$$|\tilde{\psi}_n\rangle = \sum_\mu |\Phi_\mu\rangle \, c_{\mu n} \tag{3.19}$$

of atom-centered, localized basis functions $|\Phi_\mu\rangle$ with coefficients $c_{\mu n}$. The coefficients shall be variational parameters, while the basis functions are fixed. To have a working ground-state calculation procedure, we must implement each of the Kohn–Sham steps, i.e. we must be able to calculate density from the wavefunctions, calculate the potential from the density (this step is unrelated to the basis), and be able to solve the Kohn–Sham equations. Most quantities are conveniently expressed in terms of the density matrix

$$\rho_{\mu\nu} = \sum_n c_{\mu n} f_n c_{\nu n}^* \tag{3.20}$$

The total energy, which we want to minimize, depends on the wavefunctions through the pseudodensity $\tilde{n}(\mathbf{r})$, the atomic density matrices D^a_{ij}, and explicitly through the smooth part $\tilde{T}$ of the kinetic energy in (3.16). These quantites are straightforwardly rewritten in terms of the density matrix:

$$\tilde{n}(\mathbf{r}) = \sum_{\mu\nu} \Phi^*_\mu(\mathbf{r})\Phi_\nu(\mathbf{r})\rho_{\nu\mu} + \sum_a \tilde{n}^a_c(\mathbf{r} - \mathbf{R}^a), \tag{3.21}$$

$$D^a_{ij} = \sum_{\mu\nu} P^a_{i\mu}\rho_{\mu\nu}P^{a*}_{j\nu}, \tag{3.22}$$

$$\tilde{T} = \sum_n f_n \langle\tilde{\psi}_n|\hat{T}|\tilde{\psi}_n\rangle = \sum_{\mu\nu} T_{\mu\nu}\rho_{\nu\mu}, \tag{3.23}$$

where we have defined

$$T_{\mu\nu} = \langle\Phi_\mu|\hat{T}|\Phi_\nu\rangle\,, \tag{3.24}$$

$$P^a_{i\mu} = \langle\tilde{p}^a_i|\Phi_\mu\rangle\,. \tag{3.25}$$

These are two-center integrals that can be evaluated before the start of a calculation once the atomic positions are known.

The Kohn–Sham equations can be obtained by requiring that the total energy (3.15) must be stationary with respect to the coefficients, and that the all-electron Kohn–Sham states must be orthogonal. The orthogonality condition is

$$\delta_{nm} = \langle\psi_n|\psi_m\rangle = \langle\tilde{\psi}_n|\hat{\mathcal{T}}^\dagger\hat{\mathcal{T}}|\tilde{\psi}_m\rangle = \sum_{\mu\nu} c^*_{\mu n}S_{\mu\nu}c_{\nu m}, \tag{3.26}$$

where $S_{\mu\nu}$ is the *overlap matrix*

$$S_{\mu\nu} = \langle\Phi_\mu|\hat{\mathcal{T}}^\dagger\hat{\mathcal{T}}|\Phi_\nu\rangle = \Theta_{\mu\nu} + \sum_{aij} P^{a*}_{i\mu}\Delta S^a_{ij}P^a_{j\nu}. \tag{3.27}$$

Here $\Theta_{\mu\nu} = \langle\Phi_\mu|\Phi_\nu\rangle$ are two-center integrals, and the numbers ΔS^a_{ij} are atomic constants depending on the partial waves. The orthogonality criterion is incorporated using the method of Lagrange multipliers. Differentiating the total energy plus Lagrange term by $c^*_{\mu n}$ leads to a generalized eigenvalue equation which can be solved for the coefficients $c_{\nu n}$ and eigenvalues ϵ_n:

$$\sum_\nu H_{\mu\nu}c_{\nu n} = \sum_\nu S_{\mu\nu}c_{\nu n}\epsilon_n. \tag{3.28}$$

Here we have defined the Hamiltonian matrix as the total derivative

$$H_{\mu\nu} = \frac{\mathrm{d}E}{\mathrm{d}\rho_{\nu\mu}} = \frac{\partial E}{\partial\rho_{\nu\mu}} + \int \frac{\delta E}{\delta\tilde{n}(\mathbf{r})}\frac{\partial\tilde{n}(\mathbf{r})}{\partial\rho_{\nu\mu}}\,\mathrm{d}\mathbf{r} + \sum_{aij}\frac{\partial E}{\partial D^a_{ji}}\frac{\partial D^a_{ji}}{\partial\rho_{\nu\mu}}, \tag{3.29}$$

which eventually leads to

$$H_{\mu\nu} = T_{\mu\nu} + V_{\mu\nu} + \sum_{aij} P^{a*}_{i\mu}\Delta H^a_{ij}P^a_{j\nu}. \tag{3.30}$$

The first term is the constant kinetic matrix (3.24). The second term is the matrix

$$V_{\mu\nu} = \int \Phi_\mu^*(\mathbf{r})\tilde{v}(\mathbf{r})\Phi_\nu(\mathbf{r})\,\mathrm{d}\mathbf{r} \tag{3.31}$$

of the total effective potential

$$\tilde{v}(\mathbf{r}) \equiv \frac{\delta E}{\delta \tilde{n}(\mathbf{r})} = \tilde{v}_{\mathrm{Ha}}(\mathbf{r}) + \tilde{v}_{\mathrm{xc}}(\mathbf{r}) + \sum_a \bar{v}^a(\mathbf{r} - \mathbf{R}^a). \tag{3.32}$$

The Hartree, XC and zero potential above emerge straightforwardly as derivatives of the corresponding energy terms in Eq. (3.16), with the Hartree potential obeying the Poisson equation

$$\nabla^2 \tilde{v}_{\mathrm{Ha}}(\mathbf{r}) = -4\pi\tilde{\rho}(\mathbf{r}). \tag{3.33}$$

The last term in (3.30) involves the *atomic Hamiltonian matrices* defined as

$$\Delta H_{ij}^a \equiv \frac{\partial E}{\partial D_{ji}^a}. \tag{3.34}$$

This derivative is horribly complicated[37] due amongst other things to atomic XC corrections. However it is basis set independent, and it suffices to note that ΔH_{ij}^a depend only on D_{ji}^a plus a large number of purely atomic constants. It is a special feature of PAW calculations compared to ultrasoft pseudopotential Hamiltonians that the atomic corrections can vary dynamically through changes in D_{ji}^a.

3.6 Overview

By now we can account for the entire self-consistency cycle. All two-center integrals such as $T_{\mu\nu}$ and $P_{i\mu}^a$ can be evaluated at the beginning, and a starting density (both $\tilde{n}(\mathbf{r})$ and D_{ij}^a) can be defined from the contributions of the isolated atoms. Then:

- The XC potential $\tilde{v}_{\mathrm{xc}}(\mathbf{r})$ is calculated from the density $\tilde{n}(\mathbf{r})$ depending on the relevant XC approximation.
- The total pseudocharge density $\tilde{\rho}(\mathbf{r})$ from (3.11) is calculated by adding the compensation charges $\tilde{Z}^a(\mathbf{r})$ using (3.14) chosen to cancel atomic multipole moments.
- The Hartree potential $\tilde{v}_{\mathrm{Ha}}(\mathbf{r})$ is calculated by solving the Poisson equation (3.33).
- The potential matrix $V_{\mu\nu}$ (3.31) is calculated by integrating the effective potential $\tilde{v}(\mathbf{r})$ (3.32) with the basis functions.
- The Hamiltonian matrix $H_{\mu\nu}$ (3.30) is calculated by adding kinetic, potential and atomic terms.
- The generalized eigenvalue problem (3.28) is solved for the coefficients $c_{\mu n}$ and energies ϵ_n, and the lowest states are occupied using a Fermi distribution.

- The density matrix $\rho_{\mu\nu}$ (3.20) is calculated from the coefficients and occupations.
- The pseudodensity $\tilde{n}(\mathbf{r})$ (3.21) and atomic density matrices D^a_{ij} (3.23) are recalculated.

Pulay mixing is generally used to stabilize changes in density, preventing "charge sloshing".[39]

3.7 Atomic forces

Aside from the self-consistency loop, structure optimizations and molecular dynamics simulations are formulated in terms of the force on an atom. The force on atom a is defined as the negative gradient

$$\mathbf{F}^a = -\frac{\partial E}{\partial \mathbf{R}^a} \tag{3.35}$$

of the total energy with respect to the position $\mathbf{R}^a$ of that atom. An expression for this gradient can be derived analytically from the energy expression. The gradient must be taken self-consistently in the sense that it should reflect the actual change in energy if two different energy evaluations were made with slightly different atomic positions, and it must differentially obey the orthogonality condition. Using the Hellman–Feynman force theorem and the chain rule carefully, the full force expression is

$$\begin{aligned}
\mathbf{F}^a = {} & 2\,\mathrm{Re}\sum_{\mu\in a;\nu}\frac{\mathrm{d}T_{\mu\nu}}{\mathrm{d}\mathbf{R}_{\mu\nu}}\rho_{\nu\mu} - 2\,\mathrm{Re}\sum_{\mu\in a;\nu}\left[\int\frac{\mathrm{d}\Phi^*_\mu(\mathbf{r})}{\mathrm{d}\mathbf{R}^a}\tilde{v}(\mathbf{r})\Phi_\nu(\mathbf{r})\,\mathrm{d}\mathbf{r}\right]\rho_{\nu\mu} \\
& - 2\,\mathrm{Re}\sum_{\mu\in a;\nu}\frac{\mathrm{d}\Theta_{\mu\nu}}{\mathrm{d}\mathbf{R}_{\mu\nu}}E_{\nu\mu} + 2\,\mathrm{Re}\sum_{\mu\nu}Z^a_{\mu\nu}E_{\nu\mu} - 2\,\mathrm{Re}\sum_{b;\mu\in a;\nu}Z^b_{\mu\nu}E_{\nu\mu} \\
& - 2\,\mathrm{Re}\sum_{\mu\nu}A^a_{\mu\nu}\rho_{\nu\mu} + 2\,\mathrm{Re}\sum_{b;\mu\in a;\nu}A^b_{\mu\nu}\rho_{\nu\mu} \\
& - \int\tilde{v}(\mathbf{r})\frac{\mathrm{d}\tilde{n}^a_c(\mathbf{r}-\mathbf{R}^a)}{\mathrm{d}\mathbf{R}^a}\,\mathrm{d}\mathbf{r} - \int\tilde{n}(\mathbf{r})\frac{\mathrm{d}\bar{v}^a(\mathbf{r}-\mathbf{R}^a)}{\mathrm{d}\mathbf{R}^a}\,\mathrm{d}\mathbf{r} \\
& - \int\tilde{v}_{\mathrm{Ha}}(\mathbf{r})\sum_L Q^a_L\frac{\mathrm{d}\tilde{g}^a_L(\mathbf{r}-\mathbf{R}^a)}{\mathrm{d}\mathbf{R}^a}\,\mathrm{d}\mathbf{r}
\end{aligned} \tag{3.36}$$

with

$$Z^a_{\mu\nu} = \sum_{ij}\frac{\mathrm{d}P^{a*}_{i\mu}}{\mathrm{d}\mathbf{R}_{a\mu}}\Delta S^a_{ij}P^a_{j\nu}, \tag{3.37}$$

$$A^a_{\mu\nu} = \sum_{ij}\frac{\mathrm{d}P^{a*}_{i\mu}}{\mathrm{d}\mathbf{R}_{a\mu}}\Delta H^a_{ij}P^a_{j\nu}, \tag{3.38}$$

$$E_{\mu\nu} = \sum_n c_{\mu n}f_n\epsilon_n c^*_{\nu n}. \tag{3.39}$$

The formula contains several extra terms compared to grid-based or plane-wave-based PAW force expressions[3,5] because an atomic displacement alters the atomic basis; such forces are called *Pulay forces*. A complete derivation of the formula can be found in the appendix of Paper I.[7]

Chapter 4

Atomic basis sets

By now we know how the self-consistency cycle in PAW works with a localized basis set. This chapter deals with the generation of basis sets and a few topics of more general utility.

4.1 Generation of basis sets

This section describes how basis functions are generated. Quite generally we use the form of a radial function times an angular function which is a spherical harmonic:

$$\Phi(\mathbf{r}) = \varphi(r)Y_L(\widehat{r}). \tag{4.1}$$

The spherical harmonics are the angular eigenfunctions of the laplacian operator, and emerge as factors in the solutions for any purely radial system. A perturbation of this potential changes both the radial and angular parts of a solution. Extra radial and angular degrees of freedom are therefore required to describe the perturbed atom well. Basis sets therefore consist of the following types of functions:

- One atomic orbital for each valence state. This is the minimal sensible basis set, called *single-ζ*.
- For each atomic orbital, extra functions can be added with the same angular part, but different radial parts. These are called "multiple-ζ" functions; these names comes from the tradition of enumerating them by their cutoff radius, called ζ.
- Polarization functions, which are extra functions with angular parts that are not present among the valence states.

The procedure by which these functions are chosen is explained below.

4.2 Atomic orbitals

In a radial coordinate system the Kohn–Sham equations are separable into a radial and an angular equation, with the angular equation having spherical harmonic solutions as mentioned. Due to the strong Coulomb attraction for the

heavier elements, particularly Au, the core electrons move at relativistic speeds, and must be described by the Dirac equation. In the scalar-relativistic approximation, the spin–orbit-coupling is neglected, which simplifies the solution procedure.[40] This results in the following radial equation:

$$-\frac{\mathrm{d}^2u(r)}{\mathrm{d}r^2}-\frac{1}{2Mc^2}\frac{\mathrm{d}v(r)}{\mathrm{d}r}\left[\frac{\mathrm{d}u(r)}{\mathrm{d}r}-\frac{u(r)}{r}\right] + \left[\frac{l(l+1)}{r^2}+2M(v(r)-\epsilon)\right]u(r)=0 \tag{4.2}$$

with

$$M=1-\frac{1}{2c^2}(v(r)-\epsilon), \tag{4.3}$$

where $v(r)$ is the effective potential, and $u(r)$ is related to the actual all-electron wavefunction $\mathrm{X}(r)$ by

$$u(r)=r\mathrm{X}(r). \tag{4.4}$$

GPAW already contains a radial atomic Kohn–Sham solver which is used to generate PAW setups. Eq. (4.2) is solved using non-equidistant grid representation with very fine grid spacing near 0. An initial guess for the energy is used to radially integrate the equation outward from 0 and inward from the outermost point. The two solutions must join smoothly in the middle; the energy guess is adjusted until they do. This way a solution is found for every atomic orbital $\mathrm{X}_{ln}(r)$, and a self-consistent density and potential are obtained.

The atomic orbitals in principle extend to infinity. Two things must be done before they can be used as basis functions: The functions must be localized, and they must look like pseudowavefunctions rather than all-electron wavefunctions. The simplest way to localize the solution is to solve the atomic problem with the outer boundary at the desired cutoff. This will however make the basis function non-differentiable at the boundary, which may cause the kinetic energy to depend sensitively on the exact location of grid points compared to the boundary. This is avoided by adding a smooth radial potential to the self-consistent potential. We use the same functional form as in SIESTA:[41]

$$v_{\mathrm{conf}}(r)=\begin{cases}0, & r\le r_{\mathrm{inner}}\\ \frac{A}{r_{\mathrm{cut}}-r}\exp\left(-\frac{r_{\mathrm{cut}}-r_{\mathrm{inner}}}{r-r_{\mathrm{inner}}}\right), & r_{\mathrm{inner}}<r\le r_{\mathrm{cut}}\\ \infty, & r_{\mathrm{cut}}<r\end{cases} \tag{4.5}$$

The radial equation is then non-self-consistently reintegrated to obtain functions that are localized. Since the different atomic orbitals have quite different range, they should have different cutoffs r_{cut} as well. Requiring a fixed increase $\Delta\epsilon$ of the confined orbital energy compared to the free atom universally defines reasonable cutoffs for all elements. In normal calculations we choose the confinement energy $\Delta\epsilon=0.1\,\mathrm{eV}$, which results in typical basis function cutoffs of 6–10 Bohr radii.

Next step is to convert the localized functions to pseudowavefunctions. The procedure is illustrated on Figure 4.1. It is done by solving

$$|\mathrm{X}\rangle=\hat{\mathcal{T}}\,|\Phi\rangle=|\Phi\rangle+\sum_i(|\phi_i\rangle-|\tilde{\phi}_i\rangle)\,\langle\tilde{p}_i|\Phi\rangle \tag{4.6}$$

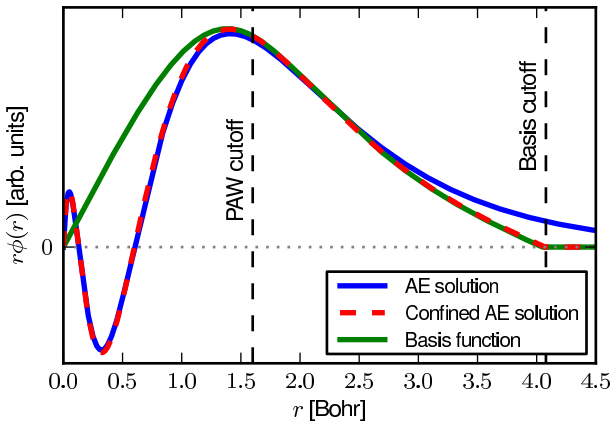

Figure 4.1: *Generation of atomic orbital basis function for S 2s-state. The all-electron partial wave is confined to a finite range ($\Delta\epsilon = 0.3\,\mathrm{eV}$), then transformed to a nodeless pseudowavefunction.*

for the basis function $|\Phi\rangle$ given the confined all-electron solution $|\mathrm{X}\rangle$, effectively inverting the PAW transformation. Applying a projector $\langle\tilde{p}_i|$ and using the completeness of the projector–partial wave basis within the augmentation region,

$$\langle\tilde{p}_i|\mathrm{X}\rangle = \sum_j \langle\tilde{p}_i|\phi_j\rangle \langle\tilde{p}_j|\Phi\rangle \,. \tag{4.7}$$

This equation can be solved for the partial-wave expansion coefficients $\langle\tilde{p}_j|\Phi\rangle$ which completely determine $|\Phi\rangle$ within the augmentation region. Note that if the coefficients $\langle\tilde{p}_j|\Phi\rangle$ are plugged directly into (4.6), the behaviour will be unstable near $r = 0$. This happens because the partial-wave basis is in reality slightly incomplete and does not entirely filter out the all-electron oscillations when inverted. It is more correct to use the partial-wave expansion of $|\Phi\rangle$ within the augmentation region and join it smoothly with $|\mathrm{X}\rangle$ at the boundary:

$$\Phi(\mathbf{r}) = \sum_i \phi_i(\mathbf{r}) \langle\tilde{p}_i|\Phi\rangle \quad \text{for small } r. \tag{4.8}$$

The basis function generation procedure is illustrated on Figure 4.1.

4.3 Multiple-ζ functions

The basis is improved by adding extra functions for each valence state. Fundamentally the goal is to have a basis set which is as complete as possible and at the same time cheap, with the basis functions being as localized as possible. It is natural to choose the confined pseudoatomic orbital $\Phi^0(r)$ as the longest-ranged basis function, since this function is physically justified. We then make up some

more functions $\Phi^\zeta(r)$ with smaller cutoffs. Define the function

$$\Delta\Phi^\zeta(r) = \begin{cases} r^l(a + br^2) & r < r_{\mathrm{cut}}^\zeta, \\ \Phi^0(r) & r_{\mathrm{cut}}^\zeta \leq r. \end{cases} \tag{4.9}$$

The prefactor r^l ensures that $\Delta\Phi^\zeta(r)$ has the correct radial behaviour of a wavefunction near $r = 0$ with angular momentum l. The parameters a and b are uniquely defined by requiring $\Delta\Phi^\zeta(r)$ to be continuous and differentiable at r_{cut}^ζ. The then define the actual basis function as

$$\Phi^\zeta(r) = \Phi^0(r) - \Delta\Phi^\zeta(r), \tag{4.10}$$

which is smooth and localized within r_{cut}^ζ. More functions can be added by selecting multiple cutoffs r_{cut}^ζ. We have found that a sensible first cutoff is obtained by defining r_{cut}^ζ such that 16 % of the norm of $\Phi^0(r)$ lies outside.

4.4 Polarization functions

Consider the lowest angular momentum l which does not correspond to any occupied valence state. This is typically a d-state for main-group elements or a p-state for transition metals. A perturbation of the valence state with angular momentum $l - 1$ will generally have a significant l-component (while it might have an $l - 1$ component, there would already be basis functions for this angular momentum channel). For this reason we add a *polarization function* with angular momentum l which, as we say, *polarizes* the preceding $l-1$ valence state.

The function is chosen to have the same cutoff as the orbital it polarizes. The approach used in SIESTA is to construct it as an actual perturbation.[9] Previous tests have not revealed any overwhelmingly importance of the exact form, and so we (still) use the rather primitive approach of defining a Gaussian-like function

$$\Phi_l^{\mathrm{pol}}(r) = Ar^l \exp(-\alpha r^2). \tag{4.11}$$

The decay constant α is chosen in terms of the norm of the tail of the polarized function. As the analytic form is not essential for our purposes, the function is modified slightly so it smoothly approaches zero at a finite range given in terms of the α.

Increasing the basis set will variationally decrease the energy of a system, with the lower limit being reachable by a grid-based GPAW calculation. Total energies tend to be much higher, while energy differences such as binding energies converge more quickly with the completeness of the basis set. Tests can be found in Paper I.[7] In general, a good compromise between efficiency and accuracy is obtained by a double-ζ polarized (dzp) basis set. This consists of the atomic orbitals plus one extra radial function each, and a single polarization function. As an example, the standard dzp basis set of gold is shown on Figure 4.2. Within a self-consistent calculation each radial function defined here contributes $2l + 1$ different spherical harmonics. Most elements have 13 or 15 such basis functions with a dzp basis set.

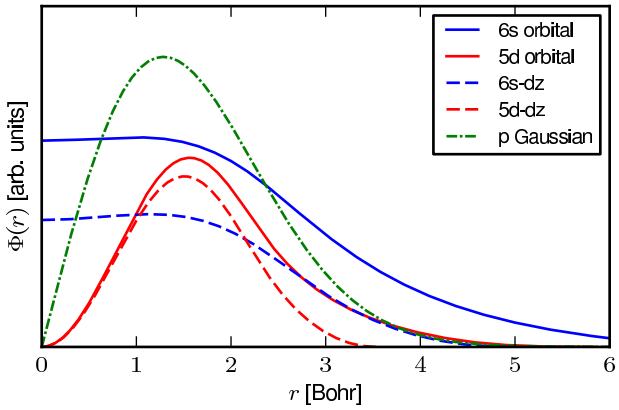

Figure 4.2: *Radial parts of basis functions of gold. Colours indicate angular momentum. Line styles indicate generation procedure. The total number of basis functions per gold atom is 15 if we count the azimuthal quantum number m.*

4.5 Basis set superposition error correction

The binding energy of some composite system with respect to its constituents is calculated by subtracting the sum of the energies of the isolated constituents from the energy of the composite system. In an atomic basis set, this introduces a *basis set superposition error* (BSSE): In the regions where basis functions overlap, atoms in the composite system effectively borrow unused degrees of freedom from one another, which artificially stabilizes the composite system. In other words, basis sets tend to produce too large binding energies.

The BSSE can be corrected by ensuring that the basis set of the composite system matches that of the isolated constituent systems. Therefore the calculation of the constituent systems should include basis functions on the sites where extra atoms would have been in the composite system. In GPAW this is implemented by adding an atom at that site equipped with the appropriate basis set, but without a pseudopotential. Such atoms are frequently called *ghost* atoms.

The BSSE is particularly large for isolated atoms. Since the basis functions are localized by truncation such that each orbital is 0.1 eV higher than on the free atom, this may, for a typical main-group atom, cause a combined increase of the total energy on the order of 0.5 eV, which the BSSE can partially "regain" in a composite system. The BSSE can therefore be several tenths of an eV for isolated atoms with the standard cutoff, but can be improved by decreasing the orbital confinement energy to e.g. $\Delta\epsilon = 0.01\,\mathrm{eV}$.

4.6 Nonorthogonality and projected density of states

We will later calculate the projected densities of states (PDOS) on various states. Within the PAW method the projected density of states on an atomic orbital,

given as an all-electron partial wave ϕ_i^a, can be approximated by[37]

$$\begin{aligned}\rho_i^a(\epsilon) &= \sum_n |\langle \phi_i^a | \psi_n \rangle|^2 \delta(\epsilon - \epsilon_n) \\ &\approx \sum_n |\langle \tilde{p}_i^a | \tilde{\psi}_n \rangle|^2 \delta(\epsilon - \epsilon_n). \end{aligned} \tag{4.12}$$

This is the standard definition used in GPAW. To the extent that the partial wave–projector basis is complete, and augmentation regions of distinct atoms do not overlap, the projected density of states integrated over all energies should yield 1. Thus it is in practice only approximate, as neither requirement is exactly fulfilled in normal calculations. This limits the use of this definition for electron-counting purposes, particularly when the objective is to filter out the total number occupation on a given atom or something similar. The atomic orbital basis set provides a natural definition of projected densities of states which is guaranteed to integrate to the right number of electrons provided that nonorthogonality is properly accounted for. Within the space spanned by the atomic basis set, the identity operator is given by

$$\hat{I} = \sum_{\mu\nu} |\Phi_\mu\rangle \, [S^{-1}]_{\mu\nu} \, \langle \Phi_\nu| \,, \tag{4.13}$$

as can be verified by applying the operator on an arbitrary linear combination of atomic orbitals. Suppose we are interested the projected density of states on an arbitrary subset M of orbitals, such as all the orbitals on atom a, or all d-type orbitals on all Au atoms. A projection operator onto that space is given by

$$\hat{P}_M = \sum_{\mu\in M, \nu\in M} |\Phi_\mu\rangle \, [P_M^{-1}]_{\mu\nu} \, \langle \Phi_\nu| \,, \tag{4.14}$$

where $[P_M^{-1}]_{\mu\nu}$ is the inverse of the submatrix of $S_{\mu\nu}$ corresponding to the subspace M (not to be confused with a submatrix of the inverse). Then we define the projected density of states on M as

$$\rho_M(\epsilon) = \sum_n \langle \tilde{\psi}_n | \hat{P}_M | \tilde{\psi}_n \rangle \, \delta(\epsilon - \epsilon_n). \tag{4.15}$$

In the case where the subspace M corresponds to a single state, the normalization is simply a division by the squared norm $\langle \Phi_\mu | \Phi_\mu \rangle$ of the basis function.

Chapter 5

Development and parallelization

This chapter describes aspects of the implementation and parallelization of localized basis set calculations and to a lesser extent real-space calculations.

GPAW is implemented in a combination of Python and C. Python is a high-level language which allows complicated tasks to be programmed quickly and with high clarity. C, as a low-level language, is well suited for number crunching. Most code is therefore written in Python using the Numpy array library, while only expensive operations are delegated to C functions or external libraries such as BLAS.

Input files for DFT calculations are written as Python scripts using the Atomic Simulation Environment (ASE).[42] This provides enough flexibility that any calculated quantity, such as Hamiltonians or overlap matrices which we will use later, can be extracted directly from an input file without special-purpose compilation or intermediate file storage. MPI is used for parallelization. This is a distributed-memory framework where each CPU core runs a separate copy of the programme.

5.1 Overview of parallelization

GPAW supports parallelization over several quantities. For real-space grid calculations, the computational cost will normally be dominated by real-space operations on the wavefunctions $\tilde{\psi}_n^{\sigma k}(\mathbf{r})$. Roughly in order from the most efficient to the least efficient, parallelization can be performed over k-points, spins σ, real-space $\mathbf{r}$ and Kohn–Sham states n. Spin parallelization for many purposes resembles k-point parallelization, and we will only distinguish between these when necessary. These parallelization modes can be used in any combination simultaneously: to each CPU is assigned a particular set of k-points/spins, a real-space domain and a set of states. The latter two parallelization modes are normally called *domain decomposition* and *band parallelization*. For medium-sized real-space calculations one usually maximizes k-point parallelization and then uses domain decomposition with the remaining CPUs. However the computational cost within a single domain increases with the number of electrons.

Operation	Parallelization	Complexity	Eq.
Poisson, multigrid	$\mathbf{r}$	$\mathcal{O}(N)$	(3.33)
Density $\tilde{n}(\mathbf{r})$	$\mathbf{r}$, σ	$\mathcal{O}(N)$	(3.21)
XC potential $\tilde{v}_{\mathrm{xc}}(\mathbf{r})$	$\mathbf{r}$, σ	$\mathcal{O}(N)$	—
Atomic XC / ΔH^a_{ij}	$\mathbf{r}$, σ	$\mathcal{O}(N)$	—
Potential matrix $V_{\mu\nu}$	ν, $\mathbf{r}$, σ, k	$\mathcal{O}(N)$	(3.31)
Diagonalization of $H_{\mu\nu}$	μ, ν, σ, k	$\mathcal{O}(N^3)$	(3.28)
Density matrix $\rho_{\mu\nu}$	μ, ν, σ, k	$\mathcal{O}(N^3)$	(3.20)

Table 5.1: *Important operations in the self-consistency cycle and how the relevant data structures are distributed over domains* $\mathbf{r}$*, spins* σ*, basis functions* μ *and* ν *and* k*-points* k*. Only operations with the most significant computational cost have been included.*

For sufficiently large systems it therefore becomes increasingly relevant to parallelize over bands.

With the introduction of the localized basis set, or *"LCAO mode"*, the same degrees of parallelization can be used (band parallelization in this case then corresponds to parallelization over orbitals). However most of the computational cost will be associated with very different operations, particularly for large systems where the cubically scaling linear algebra operations, namely diagonalization of the Hamiltonian and calculation of the density matrix, will eventually dominate.* Since these are pure matrix operations, they not parallel over domains. Many other operations are only, or almost only, parallel over domains. An overview of the different operations and how they can be parallelized is shown in Table 5.1. Clearly, for sufficiently large systems a sparse method would be faster since the Hamiltonian and overlap matrix are in fact sparse.

The implementation of the more important individual steps of the calculation procedure will be described in the following.

5.2 Linear algebra

We parallelize matrix operations using *Scalable Linear Algebra PACKage*, a software library for parallel dense linear algebra.[44,45] ScaLAPACK relies on standard standard BLAS libraries for local operations and BLACS,[46] *Basic Linear Algebra Communication Subroutines*, for parallel communication.

Matrices in ScaLAPACK are distributed among CPU cores according to a *2D block cyclic* scheme: A matrix is divided into rectangular blocks of equal size. Each core holds a set of blocks from distinct parts of the matrix, and the ownership of consecutive blocks *cycles* between the available CPUs. The CPUs are *themselves* divided into a 2D grid such that rows and columns are blocks are shared by rows and columns of CPUs in the CPU grid. The distribution is illustrated on the left in Table 5.2. The algorithms in ScaLAPACK are optimized to emphasize communication between adjacent CPUs in the CPU grid.

*The Hamiltonian and overlap matrices are both sparse, and sparse methods will therefore be favourable for the larger systems. The advantage of the sparsity of the Hamiltonian is however limited by the lack of sparsity of the coefficients $c_{\mu n}$, as the Kohn–Sham formulation is inherently global in nature. True $\mathcal{O}(N)$ methods must be formulated by alluding to locality of e.g. the spatial density matrix $\rho(\mathbf{r}, \mathbf{r}')$, resulting in a quite different formalism.[43]

0	2	4	6	0	2	4	6
1	3	5	7	1	3	5	7
0	2	4	6	0	2	4	6
1	3	5	7	1	3	5	7
0	2	4	6	0	2	4	6
1	3	5	7	1	3	5	7

0	2	4	6

Table 5.2: *The two main matrix distributions used in calculations. Left: 2D block cyclic matrix distribution. A matrix is divided into 6×8 blocks, each represented by a cell. The cells are shared by a grid of 2×4 CPUs numbered 0–7. The number in each cell indicates which CPU stores that block. Each CPU stores 6 blocks in total. Adjacent CPUs in the grid should have fast interconnect. Right: 1D column distribution, perhaps of the same matrix. Only four of the eight CPUs are used in this case.*

Thus, operations on the matrix in the example will be fast if CPU 1 has a fast interconnect to CPUs 0, 3 and 7, but it does not need a fast interconnect to the other CPUs. A simpler distribution using only half the CPUs is shown to the right in Table 5.2. Such a column-based distribution is useful for calculations that are parallel over real-space domains and orbitals at the same time. CPUs 0, 2, 4 and 6 would in this case be responsible for one domain while 1, 3, 5 and 7 would have a copy of the same matrix, but apply it to a different domain.

Parallel operations can be invoked from Python through an object oriented Python interface with the following classes, each of which relies on the underlying parallel libraries:

- Communicator: An object resembling the standard MPI communicator interface for a set of CPUs.
- BLACS grid: Represents a 2D grid of CPUs. Each BLACS grid is associated with a communicator.
- BLACS descriptor: A template for matrices with a specific 2D block cyclic layout (matrix size, block size). Provides utility methods to build and perform operations on arrays. Each BLACS descriptor is associated with a BLACS grid.
- Redistributor: Redistributes matrices between different BLACS grids or descriptors. Is associated with two BLACS grids.

Python interface functions for diagonalization and matrix multiplication are implemented in terms of the above classes.

5.3 Grids and localized functions

The calculation of the density $\tilde{n}(\mathbf{r})$ and the potential matrix elements $\tilde{v}(\mathbf{r})$ involves basis functions as well as extended real-space functions. Because the basis functions are localized, these operations are $\mathcal{O}(N)$. In terms of grid points G, the potential matrix is calculated as

$$V_{\mu\nu} = \sum_G \Phi^*_{G\mu} \tilde{v}_G \Phi_{G\nu} \tag{5.1}$$

using an explicit outer loop over G and an inner loop over all pairs (μ, ν) of locally nonzero basis functions. The density, sampled on a grid, is calculated with a similar loop over grid points G, for each of which a similar inner loop

$$\tilde{n}_G = \sum_{\mu\nu} \Phi^*_{G\mu} \Phi_{G\nu} \rho_{\nu\mu} \tag{5.2}$$

is carried out.

The basis function values $\Phi_{\mu G}$ in each grid point are pre-tabulated during initialization by explicitly evaluating radial parts times spherical harmonics. Loops over pairs of nonzero basis functions are possible by first registering, for each basis function, the grid coordinates G_{z_1} to G_{z_2} along the z axis between which the basis function is nonzero, for all pairs of grid coordinates G_x, G_y along the other axes. This metadata allows us to maintain a list of locally nonzero basis functions when looping over grid points: Basis function indices are dynamically added and removed from this list as the loop enters and leaves their localization areas. The entry/exit point metadata is stored in one buffer, while the actual basis function values are stored in a different (much larger) buffer, in an order consistent with the list of currently nonzero basis functions for easy indexing.

The operations (5.1) and (5.2) are naturally parallel over domains. They are further parallelized over orbitals ν in $V_{\mu\nu}$ or $\rho_{\nu\mu}$ using the column layout from Table 5.2. Each CPU is responsible for one domain/column combination. After $V_{\mu\nu}$ is calculated, it must be redistributed from column form to block cyclic form, where it is used to construct the Hamiltonian. After the diagonalization and calculation of $\rho_{\mu\nu}$ from the coefficients, which happens in block cyclic form, $\rho_{\mu\nu}$ is then distributed back to column form to apply (5.2).

In the force expression (3.36), the derivative of the potential matrix $V_{\mu\nu}$ with respect to a rigid displacement of a basis function must be calculated. This can be done with a similar loop, except it is the derivatives

$$\frac{\mathrm{d}\Phi(\mathbf{r} - \mathbf{R}^a)}{\mathrm{d}\mathbf{R}^a} = -\frac{\mathrm{d}\Phi(\mathbf{r} - \mathbf{R}^a)}{\mathrm{d}\mathbf{r}} \tag{5.3}$$

which are evaluated through

$$\frac{\mathrm{d}\Phi(\mathbf{r})}{\mathrm{d}\mathbf{r}} = \frac{\mathrm{d}\varphi(r)}{\mathrm{d}r} \bar{Y}_L(\mathbf{r}) \hat{\mathbf{r}} + \varphi(r) \frac{\mathrm{d}\bar{Y}_L(\mathbf{r})}{\mathrm{d}\mathbf{r}}. \tag{5.4}$$

Circumflex denotes a unit vector. The notation $\bar{Y}_L(\mathbf{R}) = R^l Y_L(\widehat{\mathbf{R}})$ refers to the real solid spherical harmonics, which are polynomials in the cartesian coordinates. Their derivatives are therefore straightforward to evaluate.

5.4 Two-center integrals and derivatives

The geometry-dependent but otherwise constant overlap integrals $T_{\mu\nu}$, $S_{\mu\nu}$ and $P^a_{i\nu}$ are calculated through the procedure described by Sankey and Niklewsky[47] which is also used by SIESTA.[9] The matrices consist of two-center integrals between localized functions which are in all cases represented as a radial part on a one-dimensional grid times a spherical harmonic which is implied from an angular momentum quantum number.

Each localized function is Fourier transformed. The two-center integrals can then can be evaluated cheaply as convolutions between a pair of Fourier transformed functions. This function is then transformed back into real-space. Due to the Fourier transform of the spherical harmonics it becomes a sum of many spherical harmonics times different radial parts:

$$\int \Phi^*(\mathbf{r})\mathrm{X}(\mathbf{r}-\mathbf{R})\,\mathrm{d}\mathbf{r} \equiv \Theta(\mathbf{R}) = \sum_L \Theta_L(R)\bar{Y}_L(\mathbf{R}). \tag{5.5}$$

See also the master thesis by Vanin.[25] Overlap matrices such as $T_{\mu\nu}$ or their position derivatives are constructed by looping over all pairs of atoms which are close enough for the localized functions to overlap. This operation is parallelized according to where atoms reside: the overlap between atom a and atom b with $a \leq b$ is calculated on the CPU responsible for the domain in which a resides. $T_{\mu\nu}$ and $S_{\mu\nu}$ are then immediately distributed on the block cyclic grid.

The force expression (3.36) involves a number of derivatives of overlaps. These are evaluated as

$$\frac{\mathrm{d}\Theta(\mathbf{R})}{\mathrm{d}\mathbf{R}} = \widehat{\mathbf{R}}\sum_L \frac{\mathrm{d}\Theta_L(R)}{\mathrm{d}R}\bar{Y}_L(\mathbf{R}) + \sum_L \Theta_L(R)\frac{\mathrm{d}\bar{Y}_L(\mathbf{R})}{\mathrm{d}\mathbf{R}}. \tag{5.6}$$

The actual overlap derivative matrices in the force formula (3.36) are evaluated this way, except they must also be antisymmetric, reflecting that interchange of two basis functions changes the sign of $\mathbf{R}$ above.

5.5 Performance benchmarks

A few performance benchmarks are presented below. These are meant to provide an idea about the performance on real systems, and are applied to some of the clusters studied in later chapters.

Figure 5.1a shows a benchmark of localized basis set calculations on Au clusters. The figure is based on structure relaxations of Au clusters generated by simulated annealing with EMT. The precise procedure is described in Chapter 10. The tests run on one 8-core xeon node on Niflheim.[48] Performance is recorded on the master core. Parallelization is used with $2 \times 2 \times 2$ domain decomposition and a 4×2 core BLACS grid. The diagonalization uses the *divide & conquer* algorithm.

A breakdown of the walltime for different operations is shown on Figure 5.1b, accounting for the total relative time spent with each operation. ScaLAPACK is invoked for clusters larger than $N = 50$ explaining the sudden shift. Some parts of the calculation, most importantly the force calculations, have not yet been optimized well in combination with ScaLAPACK. *Grid ops* refers to the calculation of $V_{\mu\nu}$ and $\tilde{n}(\mathbf{r})$, which take roughly the same time; *network* represents communication including waits due to load imbalance; *atomic* represents PAW corrections, which is dominated by radial XC; *matrix ops* refers to calculation of $\rho_{\mu\nu}$ plus smaller operations such as two-center integral evaluation.

Figure 5.2 shows scaling of computational time of individual functions measured per self-consistency step (whereas the previous figure refers to an entire self-consistency loop; the number of necessary self-consistency steps increases weakly with system size). Scaling powers are calculated by logarithmic fitting

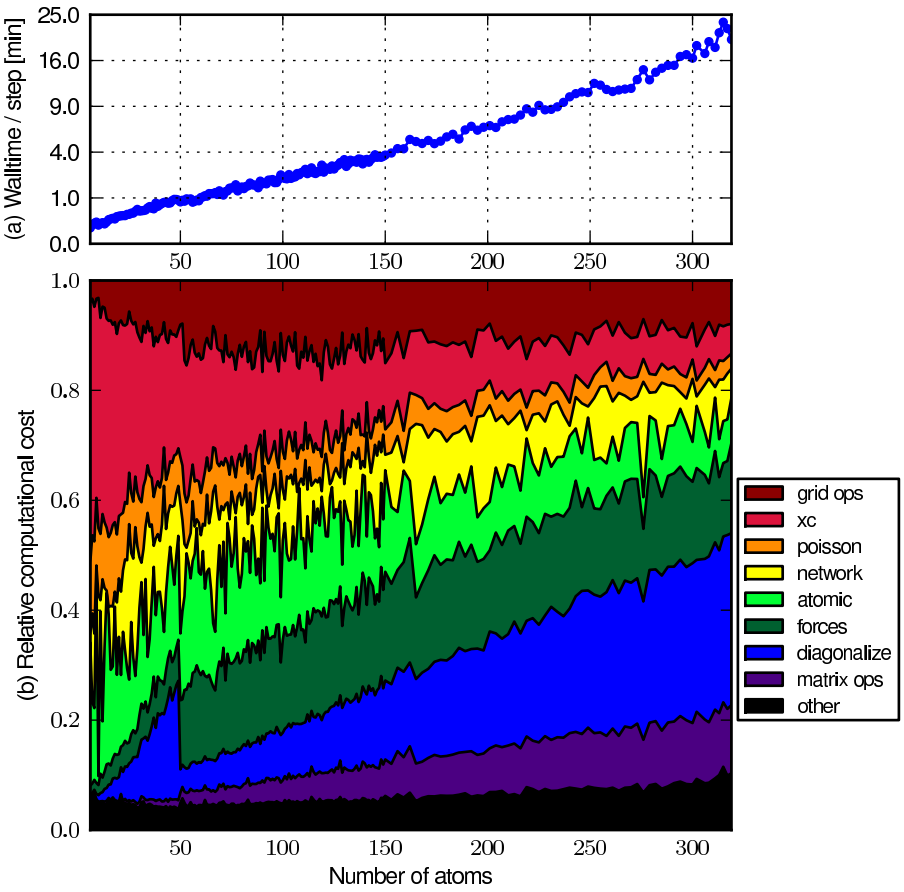

Figure 5.1: *Performance of basis set calculations on gold clusters. Top: Wall-clock time in minutes of one step in a structural optimization as a function of number of atoms. Note that the axis is quadratic. Below: Relative time spent in different parts of the code. The qualitative change at 50 atoms is due to a switch to parallel diagonalization.*

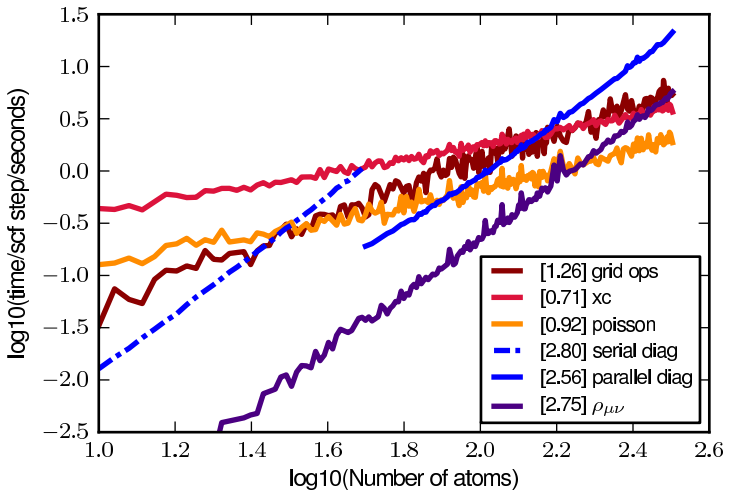

Figure 5.2: *Doubly logarithmic plot of time per SCF iteration for different operations. The scaling powers are indicated in the legend. Colours are consistent with Figure 5.1.*

for $N > 50$ except for the serial diagonalization. "Grid ops" is nominally linear, but superlinear in this case because of a gradual increase in the ratio of bulk to surface atoms with N. The increased density of orbitals around bulk atoms increases the cost. XC and Poisson performance appears sublinear because of the non-proportinal relationship between volume and number of atoms; for example, a system with one atom needs about as much vacuum as a system with two atoms.

Overall, the main limitation on parallel performance is the matrix diagonalization, as its non-local character implies significant communication. While calculations even for systems beyond 1000 atoms have been tested and are indeed faster than the real-space code, the time-consuming diagonalization is an obstacle which makes the approach practical only for systems up to around 400–600 atoms on the Niflheim cluster with the current interconnect.

5.6 Real-space calculations and parallelization

In real-space calculations, the number of variational degrees of freedom is too large to directly diagonalize the Hamiltonian like in the localized basis set. Instead an iterative procedure is used. For each self-consistency iteration, guesses for the pseudowavefunctions are improved until they converge alongside the density and potential.

The Hamiltonian is applied to the pseudowavefunctions in the real-space basis using a finite-difference stencil for the Laplacian:

$$\langle \mathbf{r}|\hat{\tilde{H}}|\tilde{\psi}_n\rangle = -\frac{1}{2}\nabla^2\tilde{\psi}_n(\mathbf{r}) + \tilde{v}(\mathbf{r})\tilde{\psi}_n(\mathbf{r}) + \sum_{aij}\tilde{p}_i^a(\mathbf{r})\Delta H_{ij}^a\,\langle\tilde{p}_j^a|\tilde{\psi}_n\rangle\,. \qquad (5.7)$$

The Hamiltonian in the basis of the current pseudowavefunctions, $\langle\tilde{\psi}_n|\hat{\tilde{H}}|\tilde{\psi}_m\rangle$, is then constructed by real-space integration. The operation involves all pairs of bands n and m, and hence the entire pseudowavefunction arrays must be passed around between band-parallelizing cores; this is why band parallelization is usually more expensive than domain decomposition, which involves communication at the domain boundaries. Following this step, the Hamiltonian matrix is diagonalized using the ScaLAPACK implementation described previously, involving redistribution to block cyclic form and back. The coefficients obtained from this diagonalization are then used to rotate the wavefunctions within their subspace so that they have definite eigenvalues.

The wavefunctions are improved by calculating the residual

$$R_n(\mathbf{r}) = \hat{\tilde{H}}\tilde{\psi}_n(\mathbf{r}) - \hat{S}\tilde{\psi}_n(\mathbf{r})\epsilon_n \tag{5.8}$$

and applying the residual minimization method described by Kresse and Furthmüller.[35] The wavefunctions are explicitly orthogonalized by constructing the overlap matrix $\langle\tilde{\psi}_n|\hat{S}|\tilde{\psi}_m\rangle$, and performing the rotation

$$\tilde{\psi}_n(\mathbf{r}) \leftarrow \sum_m \tilde{\psi}_m(\mathbf{r})[L^{-1}]_{mn}, \tag{5.9}$$

where L_{mn} is the Cholesky decomposition of S_{mn}. ScaLAPACK is used again for this inverse Cholesky decomposition of the overlap matrix. The remaining steps of the self-consistency cycle have for the most part been discussed in the previous chapter.

The computational cost for large systems is dominated by the cubically scaling and communication-intensive matrix element calculations, plus the subsequent rotations. Provided that the diagonalization is parallelized, it is not among the most expensive operations. Parallel diagonalization is also important for another reason: The double-precision floating point representation of a bands-by-bands matrix in a 10000-electron system (e.g. 1000 Pt atoms) requires about 200 MiB RAM. This is clearly unacceptable on a BlueGene/P with 512 MiB RAM per core.

This is the calculation procedure for the large-scale DFT calculations presented in later chapters. A scaling benchmark can be found in Paper II.[6]

5.7 Parallelization on BlueGene/P

It is our intention to perform DFT calculations on very large gold clusters using the accurate but expensive real-space grid methods in GPAW. For this purpose we use the IBM BlueGene/P supercomputer located at Argonne National Laboratory. In the limit of very large systems, some of the otherwise innocuous operations become quite expensive and must be taken into account in the implementation.

Supercomputers of small to medium size typically contain a number of distinct *nodes*, each containing a small number of CPU cores. The nodes might be connected by means of network switches, providing the usual star-shaped network topology where all CPUs can communicate with each other directly. For sufficiently large computers a network of this type will, however, suffer congestion because all data must pass through the same switch. An indefinitely

scalable computer therefore cannot have a star-shaped topology, but must make use of localization. The parallel structure of a programme must then take into account the network topology of the supercomputer on which it runs, so that communication takes place if possible only between neighbouring nodes.

In the BlueGene/P supercomputer which is our specific target, the nodes are connected in a three-dimensional grid. Each core is assigned a set of coordinates XYZT, where XYZ designate the position of the node in the grid, and T enumerates the cores within a node (and acts as a very short fourth dimension). A core is connected directly to its immediate neighbours along each of these four grid directions. The first and last CPUs in each direction are also directly connected. The network topology is therefore a four-dimensional torus, which has a maximal of size $40 \times 32 \times 32 \times 4$ cores, or 163840 CPUs. Calculations generally involve smaller sets (or *partitions*) of CPUs which are also wired to form a torus. Since solution of the Kohn–Sham equations is parallel over both the three spatial directions (x, y, z) and states n, the logical parallelization is to let the XYZT network torus correspond some permutation of x, y, z and n.

Part II

Electronic and chemical properties of metal clusters

Chapter 6

Metal nanoparticles

This chapter provides a short introduction to metal nanoparticles. An overview of the geometric structures formed by nanoparticles is given, and different simple models for their structure and properties are discussed.

Nanoparticles have important applications in catalysis, where size-dependent changes in chemical properties can have a big impact on catalytic activity. For example gold clusters become effective catalysts under some conditions. Of particular note is the ability of gold clusters, when deposited on surfaces of certain transition metal oxides, to oxidize CO at very low temperatures.[49] This has been observed for gold particles of around 4 nm in size.[50] The high catalytic activity has been attributed to a number of effects, such as non-metallic behaviour associated with flat "islands" of gold atoms.[51] Others attribute the increase in reactivity mainly to the availability of low-coordinated atoms and surface roughness, although many effects are understood to be involved.[52–56] Understanding the catalytic activity is part of the motivation for this work, although we focus on understanding the more fundamental properties of free-standing nanoparticles. These are much simpler systems than the complicated nanoparticle/support-based systems used in catalysis.

6.1 Packing and structural motifs in clusters

The lowest-energy shapes of very large nanoparticles are characterized by the combination of crystal planes which yields the lowest total surface energy, and can be obtained by the Wulff construction method. For smaller clusters, size effects will allow several different structural motifs to compete. A few such structures of particular relevance will be described below.

A number of highly symmetric structures can be constructed by successively adding shells of atoms. A simple such structure is the *cuboctahedron*. The first cuboctahedron is formed by adding 12 neighbours around a central atom, forming part of an fcc lattice. Further cuboctahedral structures can be formed by adding further such shells, resulting in clusters with 13, 55, 147, 309, 561, 923, 1415,... atoms. The first few cuboctahedral clusters are shown on Figure 6.1. The cuboctahedra are simple fcc-based clusters with (111) and (100) surfaces. By adjusting the number of (111) versus (100) surface layers, one can also obtain cubes, truncated cubes, cuboctahedra, truncated octahedra and octahedra—see

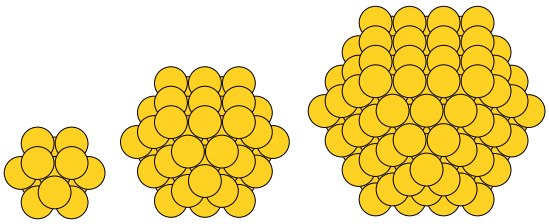

Figure 6.1: *The first three cuboctahedral clusters, having 13, 55 and 147 atoms.*

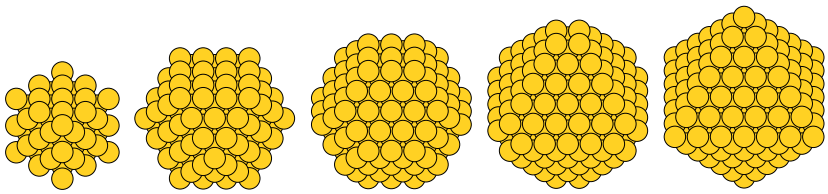

Figure 6.2: *A family of fcc clusters: 63-atom cube, 147-atom cuboctahedron, 201 and 225-atom truncated octahedra and 231-atom octahedron.*

Figure 6.2. Truncated octahedra are frequently the most stable structures for large clusters, including those of Au.[57]

The close-packed (111) surfaces of fcc structures tend to have the lowest surface energy. It is possible to form clusters with *only* (111)-like surfaces, although this happens at the expense of internally straining the cluster by breaking the fcc structure. This is the case for the icosahedral series of clusters. Like the cuboctahedra, these are generated by adding successive layers of atoms around a single atom, resulting in the same geometric shell closings at 13, 55, 147, ... atoms. The first few icosahedra are shown on Figure 6.3. The distance between atoms in neighbouring icosahedral shells differs from the distance between atoms within the same shell. This causes an overall $\mathcal{O}(N)$ increase in energy, while the decrease in energy from the change in surface structure must be proportional to the amount of surface $\mathcal{O}(N^{2/3})$. The icosahedral motif is therefore likely for medium-sized clusters. Many other lattice-based structures can be imagined, of which the most important for gold are probably truncated decahedra[58,59] which are, like the icosahedra, internally strained. A thorough classification of atomic shell structures has been written by Martin.[60] The free

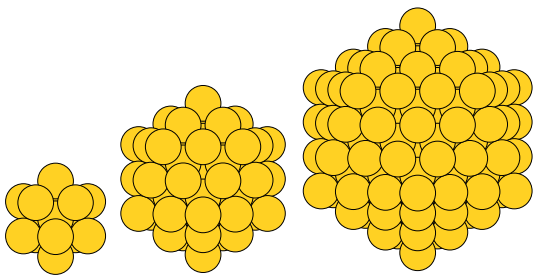

Figure 6.3: *Icosahedral clusters with 13, 55 and 147 atoms.*

energy of different structural motifs depends on size as well as temperature, leading to complicated phase diagrams with temperature-dependent preference for different structures.[61–63]

Due to the high computational cost of ab-initio methods, the structural properties of large metal clusters are usually studied through simple models. Several such models are based on pair potentials with energy terms that model the attractive and repulsive parts of atomic interactions formulated e.g. as an energy contribution for each pair of atoms. For example, the Sutton–Chen[64] and Gupta[65] potentials both predict highly stable Ag clusters with 13 (icosahedral), 38 (truncated octahedral), 55 (icosahedral) and 75 (decahedral) structure.[66] The low energy coincides with particularly regular atomic packing. Such many-body potentials can be well suited to describe the specific properties they were designed for, but make no reference to electronic structure, which limits their ability to describe small clusters.

6.2 Jellium clusters

A simple model of materials can be obtained by entirely neglecting atomic structure, and instead assuming that electrons are interacting in a smeared-out background charge so that the whole system is neutral. This fictitious material is called *jellium*. Jellium models of clusters have been studied extensively since the discovery that alkali metal clusters with specific "magic" numbers of electrons are particularly stable and can be understood through jellium models.[20,21,67–73] Below we describe the simplest imaginable jellium model of clusters, namely that of independent electrons in an infinite spherical well.

Assume that a cluster with N electrons is described by an infinite spherical well potential with radius $R = N^{1/3}$. By separation of variables one obtains distinct equations for radial and angular parts of the eigenstates, quite like in the atomic problem from Section 4.1, except for the shape of the radial potential. The radial equation is the spherical Bessel equation with zero boundary conditions, whose solutions are spherical Bessel functions $j_l(r)$ of the first kind.* The angular equation as always yields spherical harmonics $Y_{lm}(\theta, \phi)$. Thus

$$\psi_{lnm}(r, \theta, \phi) = \alpha_{ln} j_l \left(\frac{z_{ln} r}{R} \right) Y_{lm}(\theta, \phi), \tag{6.1}$$

where α_{ln} is a normalization factor and z_{ln} is the n'th zero of j_l. The energies of these solutions are

$$\epsilon_{ln} = \frac{1}{2} k_{ln}^2 = \frac{1}{2} \frac{z_{ln}^2}{R^2}. \tag{6.2}$$

Thus there exists a set of degenerate solutions for each zero z_{ln} of each spherical Bessel function $j_l(r)$, with degeneracy $2(2l+1)$, counting spin. The energy levels are ordered the same way as the zeros of the spherical Bessel functions. This results in an *Aufbau* rule like in the periodic table, except a higher angular momentum tends to be relatively more favourable for jellium clusters than additional radial nodes. Configurations with a full shell are particularly stable, and

*The spherical Bessel functions are related to the ordinary ("cylindrical") Bessel functions by $j_l(r) = \sqrt{\frac{\pi}{2r}} J_{l+\frac{1}{2}}(r)$.

2	**8**	**18**	20	**34**	40
58	68	90	**92**	106	132
138	168	**186**	196	198	232
254	268	306	312	**338**	380
398	428	**438**	**440**	486	508
542	556	562	612	638	...

Table 6.1: *Magic numbers of spherical non-interacting jellium clusters. Major magic numbers, having particularly large electronic gaps at the Fermi level, are highlighted.*

the cluster is said to contain a *magic number* of electrons. In order of increasing energy, the eigenstates are 1s, 1p, 1d, 2s, 1f, 2p, 1g, ..., which results in magic numbers at the shell fillings N=2, 8, 18, 20, ...; see Figure 6.4 and Table 6.1.

The spherical-well model above is the simplest possible jellium model. Many other jellium-based models have been formulated to describe alkali metal clusters. The inclusion of electronic interactions, typically through the solution of the Kohn-Sham equations using the local density approximation, yields magic numbers similar to those we found in the previous non-interacting model. The relative importance of the different magic numbers may shift depending on the exact model used, but the spherical shell closings are almost universally reproduced as listed in Table 6.1. Further insight is gained by considering jellium clusters of different shapes. Commonly, the jellium clusters are allowed to deform under some specified set of rules.[71,74–77] An important result is that jellium clusters with a non-magic number of electrons will deform into prolate (elongated along one axis) or oblate (flattened) shapes depending on the number of electrons. This allows non-magic clusters to obtain lower energies, which we will also see in Chapter 10 using DFT calculations. Different highly symmetric shapes such as tetrahedra also lead to strong magic numbers.[78]

The previously mentioned pair potentials are formulated only in terms of atomic separations, while jellium models completely neglect atomic structure. Both electronic and structural effects can be combined in tight-binding models, such as the Hückel model.[79–82] This model predicts electronic magic numbers in agreement with the jellium model.[83,84]

6.3 Noble metal clusters, relativity and gold

Since the noble metals have a fully occupied d-band and a half-filled s-band, they are electronically similar to alkali clusters. Jellium-like magic numbers have been observed in the mass spectra of noble metal clusters, indicating particular stability of clusters with closed electronic shells.[22] While clusters of the three noble metals show similar electronic shell structure, gas-phase gold clusters form especially remarkable geometric structures. The smallest gold clusters are predicted to be planar, with a transition between planar and 3-dimensional structures usually put between 8–15 atoms depending on charge and other circumstances.[18,85,86] The exact transition between planar and 3-dimensional clusters of various charge states has been discussed extensively within DFT methods and depends strongly on the XC approximation.[19,87–89] Larger gold

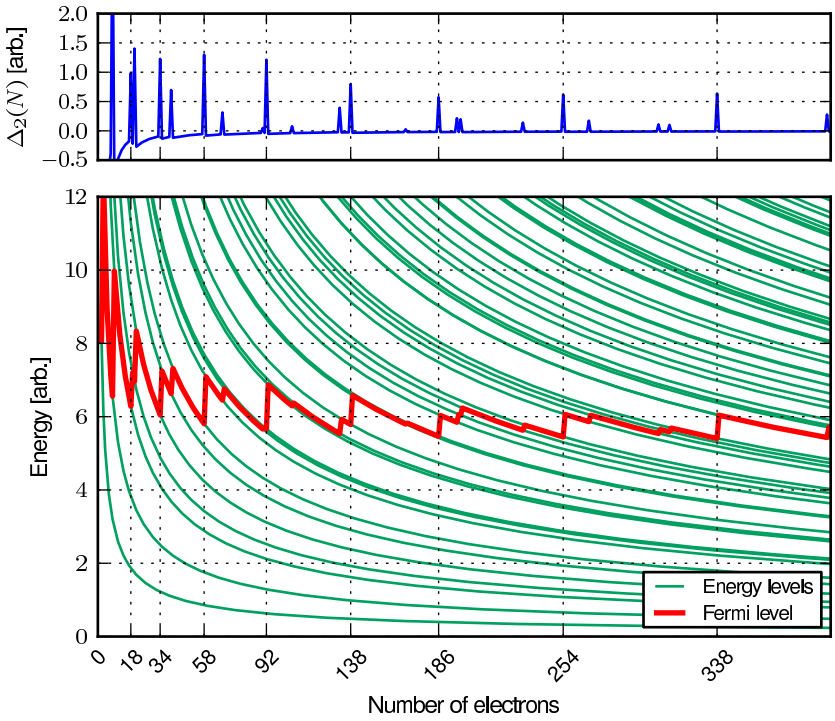

Figure 6.4: *Below: Energy levels and Fermi level of spherical-well jellium clusters as a function of number of electrons. Major magic numbers are indicated. Above: Second-order energy differences* $\Delta_2(N) = E(N-1) - 2E(N) + E(N+1)$*, a measure of the curvature of the total energy with respect to the number of electrons.*

clusters are predicted using DFT to form many more exotic structures, such as cages and tubes. This occurs even beyond 30 atoms, with the 32-atom cluster being a cage.[19,90,91] The stability of planar structures, along with practically all the peculiarities of subsequent Au clusters as compared to Ag or Cu, can be attributed to the relativistic behaviour of the Au core electrons. These effects change the screening of the outer electrons, leading to a contraction of s-states and an expansion of the d-states, and an increase in hybridization between the d-states.[17] Gold in particular has a tendency to form low-symmetry structures.[92] Even the 55-atom Au cluster does so rather than forming an icosahedron as has been found for Ag.[93,94] Determination of globally optimal structures of most larger clusters must to some extent rely on simpler methods, although limited studies of large clusters with DFT have been made.[95,96]

Chapter 7

Chemical properties of large clusters

In this chapter we examine the convergence of chemical properties of clusters with respect to cluster size. This is done by calculating binding energies of simple adsorbates on cuboctahedral clusters up to 1415 atoms. The cuboctahedra are not lowest-energy structures,[57,97] and particularly the small clusters Au_{13} and Au_{55} are known to form entirely different structures in the gas phase. However the cuboctahedra provide a simple geometry which can be compared at different sizes and with different metals. Here we compare Au and Pt clusters, where the main difference is that Au, unlike Pt, has a filled d-band.

7.1 Structure and calculation parameters

We calculate the binding energy of O and CO, each on two different adsorption sites, and on Au as well as Pt cuboctahedra. The motivation for specifically considering O and CO is the relevance of these adsorbates as intermediates in CO oxidation, although we make no attempt to model actual catalytic systems at this time. Figure 7.1 shows the adsorption sites. They are:

- O on the fcc hollow site closest to the center of an (111) facet

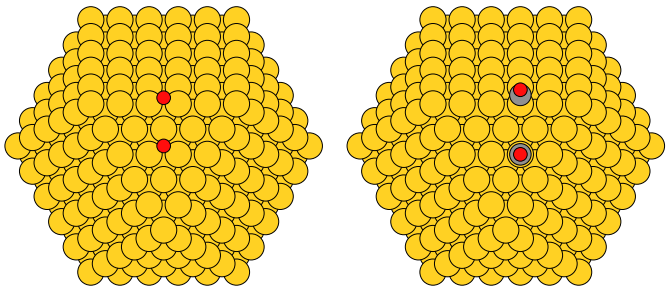

Figure 7.1: *Adsorption sites, shown two at a time, of O and CO on the Au_{561} cuboctahedron.*

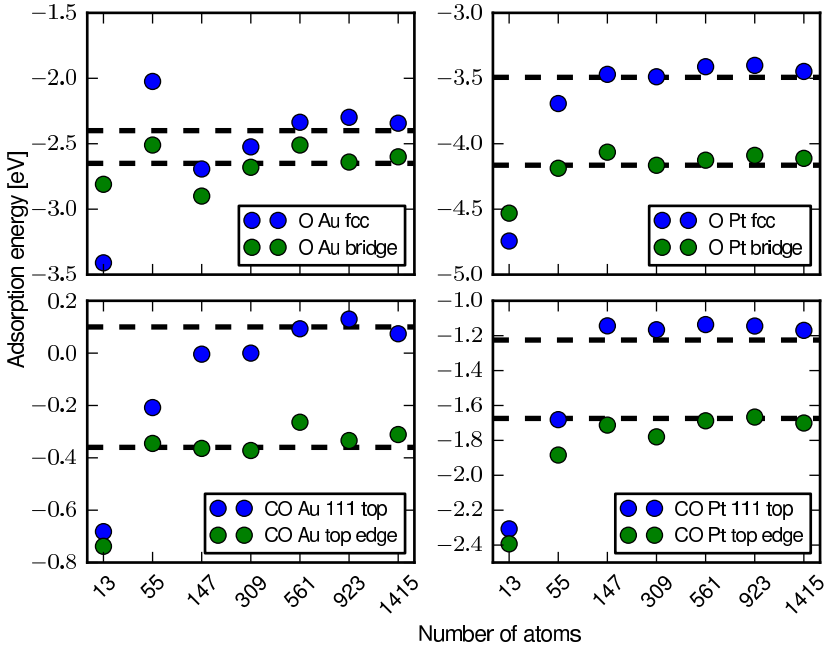

Figure 7.2: *Binding energy of O and CO on cuboctahedral Au and Pt clusters of different size. For each series of datapoints, the bulk limit is indicated.*

- O on the bridge site closest to the center of an edge
- CO on top of the atom closest to the center of an (111) facet
- CO on top of the atom closest to the center of an edge, with O pointing away from the cluster

The distance between adsorbate and metal atoms is in each case based on a relaxation of the adsorbate on an infinite metal surface locally similar to the cluster. Since no relaxation of the cluster is performed, we do not care to deeply about the exact geometry of the adsorbate either. In the limit of infinitely large clusters, the environment around each adsorbate approaches either that of a clean surface or a step configuration. Such configurations are used to obtain values for the bulk limits. The calculations are performed using the RPBE XC-functional with the real-space grid implementation in GPAW. A grid spacing of 0.175Å is used for Au clusters, and 0.140Å for Pt clusters. The lattice constants 4.218 Å for Au or 3.999 Å for Pt are used in the cluster construction. No structure relaxation is performed in these calculations. The effects of structure optimization on the adsorption energies to Au cuboctahedra has been found to be small; see Paper III.[98]

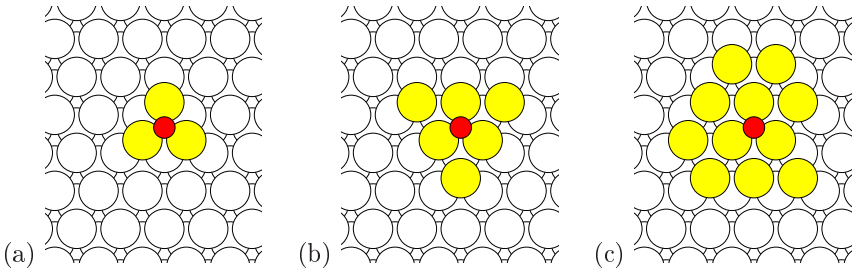

Figure 7.3: *O adsorption on adatom plateaus of sizes 3, 6 and 11 atoms. The colouring only serves to distinguish adatoms from surface atoms; adatoms and surface atoms are the same type.*

7.2 Adsorption energies

The calculated adsorption energies as a function of cluster size are shown on Figure 7.2. A common feature of both Pt and Au clusters is that small clusters tend to bind the adsorbates more strongly. A notable deviation from this trend is that the O on both (111) facet and bridge site of the Au_{55} binds extremely weakly, weaker even than the bulk limit (upper left on Figure 7.2). The low reactivity towards O of Au_{55} is consistent with existing observations,[99,100] although the real free-standing Au_{55} is known to have a quite different low-symmetry structure.[93,95] CO on Au exhibits a much more smooth convergence towards the bulk limit.

For Pt, the overall size-dependent change in adsorption energies is more uniform than for Au. Almost all variation stops after $N = 147$, except a slight fluctuating tendency which is slowly damped.

Variation in the cluster size will necessarily change both the local structure around of the adsorbate, and the overall cluster size. The changes in local structure can be studied separately from calculations on extended surfaces. This will be done in the next section. In the next chapter we will study electronic effects more closely.

Further analysis of the large-scale results for Pt are in progress (unpublished). A more thorough discussion of the results for Au can be found in Paper III.[98]

7.3 Geometric effects on adsorption

Part of the size trend in the previous calculations must be attributable to the change in size of the facets. To investigate this local, geometric effect we compare cluster adsorption energies with adsorption energies calculated on infinite surfaces with plateaus of various size. We concentrate here on O adsorption on Au and Pt.

We consider an fcc (111) surface slab with four layers of atoms and lattice constants 4.218 Å for Au or 3.999 Å for Pt, as before. On top of the slab we construct plateaus with different numbers of adatoms forming part of an extra surface layer. We start with an adatom trimer whose central (111) fcc site is locally consistent with the previously considered O adsorption site. The plateau

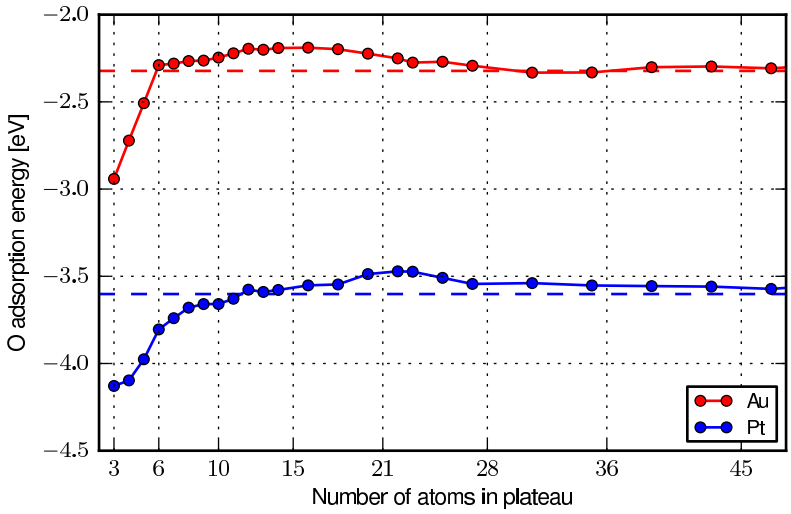

Figure 7.4: *Binding energy of O on central fcc site of Au and Pt one-layer adatom plateaus as a function of the number of atoms in the plateau. The bulk limit is indicated by a dashed horizontal line. Ticks on x axis are placed so they correspond to sizes of cluster facets (the 55-atom cuboctahedron or icosahedron has 6 atoms in an (111) facet).*

is then expanded by adding one atom at a time on sites consistent with the lattice. A few of the geometries are shown on Figure 7.3. Each time, the atom is added as close as possible to the adsorbate such that the adsorbate will always be close to the center of the plateau. In order to fit a plateau with 50 atoms in the cell (the 1415-atom cuboctahedral (111) facet contains 36 atoms), it is necessary to include a total of 365 atoms in the calculation. We use the localized basis set with the standard double-ζ polarized basis sets.

For each of these geometries we then calculate the adsorption energy without any structure relaxation. O is put at a fixed perpendicular distance of 1.37 Å (Au) or 1.28 Å (Pt) from the plateau atoms which is consistent with the fixed cluster geometries.

The adsorption energy of O as a function of the number of adatoms is shown on Figure 7.4. For Au the adsorption energy increases swiftly and linearly between plateau sizes of 3–6 atoms. Once the triangular 6-atom plateau on Figure 7.3 is completed, the energy remains largely constant. The 6-atom plateau is identical to the (111) facet on the Au_{55} cluster which binds O very weakly, but the geometric trend here is insufficient to explain the spectacularly weak binding on Au_{55}. Medium-sized plateaus up to 28 atoms (like the 923-atom cluster) bind slightly more weakly than bulk Au, after which the difference from bulk is tiny. This geometric trend thus accounts (partially) for the strong binding on the 13-atom cluster compared to subsequent clusters, but agrees with *none* of the behaviour of other clusters until near the bulk limit at 561 atoms and

larger.

For Pt the smallest plateaus also bind strongly, but the trend differs from that of Au since the binding energy varies much more smoothly over the small plateaus. The convergence of the Pt binding energy with respect to plateau size matches roughly that of the Pt clusters: after a plateau size of 10 atoms (147-atom cluster), most of the variation has stopped, and only weak oscillations remain.

In the next chapter we will consider the effect of electronic structure on adsorption energies.

Chapter 8

Electronic structure and chemisorption

The variation in adsorption energies for smaller clusters, and in particular the very weak adsorption of O on the Au_{55} cluster, remains to be explained. To study electronic effects on adsorption in greater detail, we will in this chapter construct a contiguous range of clusters up to several hundred atoms. This implies a quite large number of calculations. Since we are not interested in binding energies with high accuracy, but rather the overall trend, the localized basis set method is ideally suited for these calculations.

8.1 Construction of clusters

Consider two consecutive cuboctahedral clusters. We can get a contiguous range of intermediate clusters by stripping off the outermost shell of atoms in the larger cluster one atom at a time, so that eventually only the smaller cluster remains. The atoms can be removed in any order. To obtain reasonably realistic geometries, we choose to always remove at random one of the atoms with lowest coordination. Since we want to calculate an adsorption energy for each size of cluster, and since we are interested in overall electronic size effects rather than the effects of geometry, the local geometry around the adsorption site should remain unchanged during this procedure. This can be managed by effectively removing two shells from the side of the cluster opposite the adsorption site. This procedure is shown on Figure 8.1. Since atoms are removed at random, a pseudorandom number generator can be used to generate several series of clusters. This reveals how sensitive the procedure is to detailed structural differences, although the strictly cuboctahedral clusters always have the exact same geometry. The procedure can be used to generate any structure based on geometric shells, and we will use this to compare to icosahedral clusters. However because of the internal straining of icosahedra, the local geometry around the adsorbate cannot be conserved for all sizes of clusters. For convenience we therefore limit this study to cuboctahedra with the adsorbates located at the central (111) fcc site as indicated on Figure 8.1. The same site was also considered in our previous studies. The Au_{13} cuboctahedron does not have an (111) fcc site (only an hcp site), so this cluster cannot be generated from the discussed procedure; instead

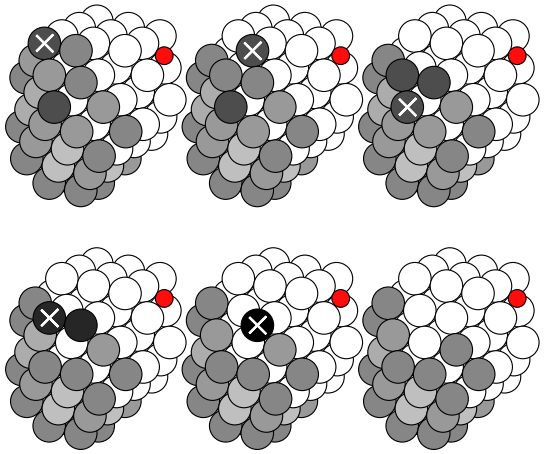

Figure 8.1: *Construction of clusters with arbitrary number of atoms. Atoms in the 55-atom cuboctahedron are white, while removable atoms are coloured according to their coordination. At each step, one of the removable atoms with lowest coordination is removed. An O atom is shown at the (111) fcc site.*

we use a 19-atom cluster which is the result of removing most of the atoms from the Au_{55} cuboctahedron without changing the immediate environment around the adsorbate.

Over the next sections we perform calculations on clusters up to 200 or 320 atoms in size. For clusters larger than 150 atoms we skip two thirds of the clusters to save CPU time. This may appear as pixelation in some of the figures, but does not represent any physical effect.

8.2 Calculation parameters

For four different series of randomly generated Au clusters we calculate the adsorption energy of O using the localized basis sets in GPAW. The calculations use somewhat coarse parameters to improve efficiency. The grid spacing is 0.2Å, and 5.0Å vacuum is added in all directions. Each atom has the standard double-zeta polarized basis set and the standard PAW setup package supplied with GPAW. The RPBE XC functional is used as in the previous calculations. A Fermi temperature of 0.01 eV is used. We do not consider spin-polarization except in atomic reference calculations.

For each cluster a structure optimization is performed with O located at the central (111) fcc site. The implementation of the BFGS structure optimization algorithm from ASE is used.[42] Structure optimizations terminate when the forces are no greater than 0.075 eV/Å.

Since we are not interested in high accuracy, but rather in a broad size-comparison of different clusters, we calculate adsorption energies in a more rough way than normally. First a structure relaxation of the combined system, cluster plus adsorbate, is performed, yielding a total energy. The binding energy is then calculated by subtracting the total energy of the isolated atom and the total energy of the isolated cluster. In the calculation for the isolated cluster we do

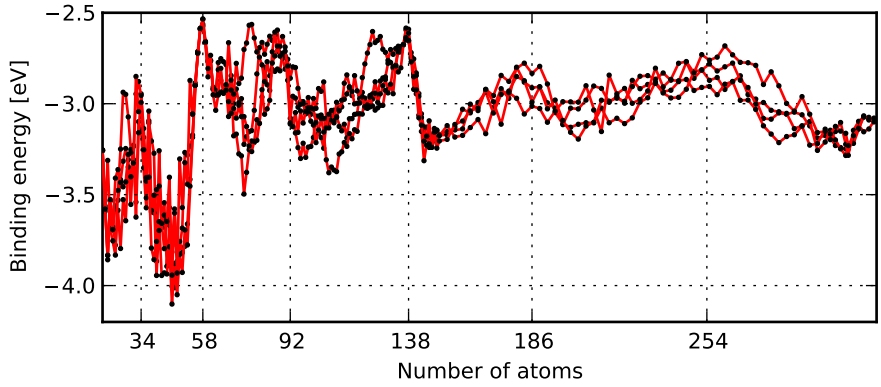

Figure 8.2: *Binding energies of O on Au clusters as a function of cluster size. Major jellium magic numbers are indicated.*

not perform a separate structure relaxation. Aside from saving time, the benefit of this procedure is that we do not have to worry about the *egg-box effect*: If we relaxed both the combined system and the isolated cluster, the atoms would have moved slightly relative to the grid points, which causes a small difference in evaluated energies. For large systems such an error will eventually be significant compared to a one-atom binding energy. The overall effect of not relaxing the isolated cluster is that *all binding energies are overestimated*. Furthermore, we shall not care to apply a basis set superposition error correction (Section 4.5). This error is similar for all the clusters since the local environment around the atom is similar, and therefore shifts all the energies by approximately the same amount.

8.3 Adsorption energy and magic numbers

Figure 8.2 shows the adsorption energy of O on the central fcc site on Au cuboctahedra as a function of number of atoms. Four different series of randomly generated clusters are shown. The binding energy oscillates with an amplitude of 0.5–1.0 eV. Minima in binding occurs at or close to the jellium magic numbers $N = 34, 58, 92, 138$, 186 and 254, in most cases followed by a sudden increase binding.

Figure 8.3 shows the density of states (DOS) of the Au cuboctahedra as a function of cluster size and energy. The d-band lies between -10 and -6, eV and changes relatively little. The s-states, however, split up into distinct electronic shells separated by gaps. As cluster size increases, shells are filled one electron at a time. When a shell is full, electrons must be filled into the next higher shell, resulting in an abrupt increase in Fermi level at the magic numbers 34, 58, 92 and 138 matching the jellium model. The subsequent magic numbers are not as clearly resolved, but the shell structure is still evident. This electronic shell structure is not specific to cuboctahedra. Figure 8.4 shows a closer view of the DOS of cuboctahedra compared and icosahedra near the Fermi level. The icosahedra are generated by the same procedure by stripping off atomic shells one atom at a time. The two types of structure have highly similar electronic

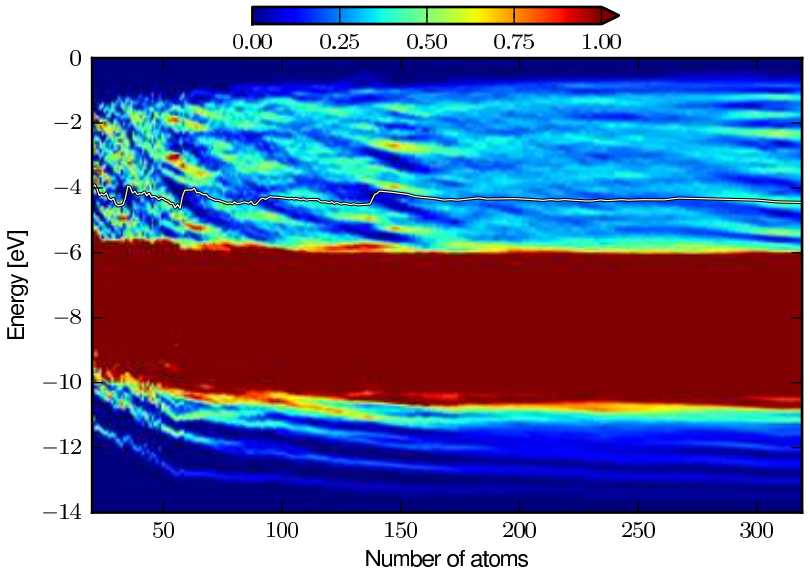

Figure 8.3: *DOS of Au clusters based on the cuboctahedral series as a function of cluster size and energy. The Fermi level is indicated by a white line. Magic numbers are associated with abrupt jumps in the Fermi energy.*

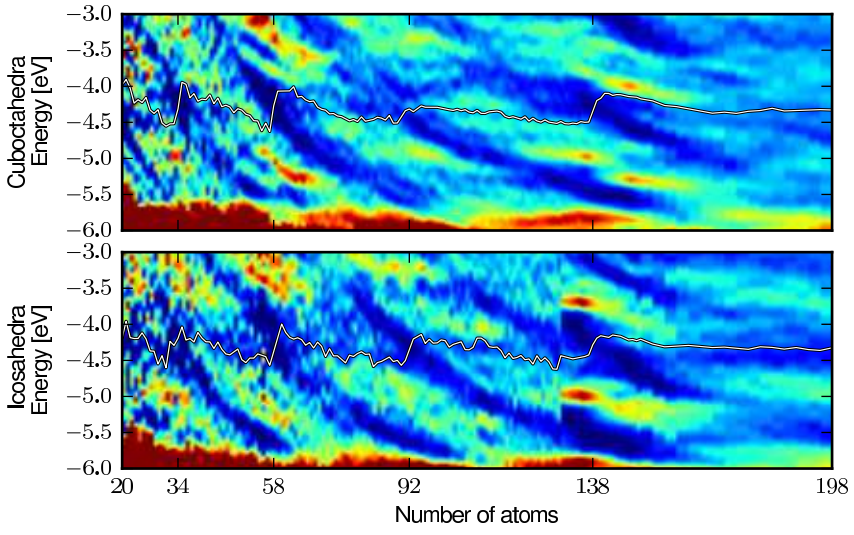

Figure 8.4: *DOS of cuboctahedral (top; a subset of the data in Figure 8.3) and icosahedral (bottom) Au clusters near Fermi level. The Fermi level is indicated.*

shell structure. It has previously been shown in models based on spherical, cuboctahedral and icosahedral potential wells that the DOS remains highly similar up to several hundred atoms in size.[101] In small jellium clusters the magic numbers are also known to be robust to geometric variations as long as the gaps between shells are large compared to the effect of distortion.[102]

The trend in adsorption energy is roughly consistent with the notion that the loosely bound electrons of a cluster just after a magic number are more easily donated to O, causing an abrupt increase in O binding energy at the magic numbers (this is most clearly seen at $N = 138$). As cluster size increases further, the energetic distance between subsequent shells decreases, causing the shell structure to become less well resolved. However we still see from Figure 8.2 how the magic numbers 186 and 254 correspond to particularly weak binding, even if no well-resolved magic number is immediately visible in the spectrum from Figure 8.3. In general, the electronic shell structure is very well resolved close to the geometric shell fillings (55 and 147 for both cuboctahedra and icosahedra), and for smaller clusters where the energetic separations between electronic shells are large. Au_{55} is just below a magic number, while Au_{147} os slightly above one. This accounts for the observations in the previous calculations that Au_{55} binds O much more weakly compared to Au_{147}.

Magic-number clusters far from geometric shell fillings, such as the $N = 92$ cluster, may be deformed significantly due to the generation procedure. This is probably why the magic number appears to be slightly smaller from the current results (minimal binding is found close to 88 atoms) than in the jellium model.

We note that structure relaxations tend to enhance the shell structure, and the magic number at $N \approx 92$ is only visible for cuboctahedra due to this relaxation. Evidently the effect of a clear shell structure is stabilizing. We will study stability more systematically in Chapter 10.

The current results suggest that the Fermi level acts as a descriptor for the reactivity with O. While variations in the oxygen binding energy do tend to correlate with in the Fermi level, this correlation is however far from perfect. Aside from geometric effects as we have seen, a large DOS near the Fermi level may also increase adsorption strength (e.g. near $N = 309$). A more complete picture would be that the overall accessibility of loosely bound electrons from the adsorption site plays an important role. Such an effect has previously been pointed out for the adsorption of molecular oxygen on Au clusters.[53]

On a side note, the clear relationship between the electronic shell structure clusters and the chemical properties of gold clusters raises the question of whether the previous conclusions, placing the convergence of adsorption energies with Au cluster size at about 600 atoms, might be wrong due to magic numbers in between the cuboctahedral geometric shell closings. The spectra from icosahedral and spherical potential-well models have been found to be highly similar as high as 1000 atoms, while cuboctahedral potential wells deviate much more quickly beyond a few hundred atoms.[101] Au clusters have been predicted to form truncated octahedra from somewhere around 500 atoms and above, preceded by decahedral clusters.[57,59] The lower symmetries of truncated octahedra and decahedra (compared to cuboctahedra and icosahedra) will to some extent disfavour the formation of large gaps.

Another effect which works to disfavour highly magic numbers for clusters much larger than 500 atoms, at least to the extent that the clusters can still be considered vaguely spherical, is the supershell structure. The relationship

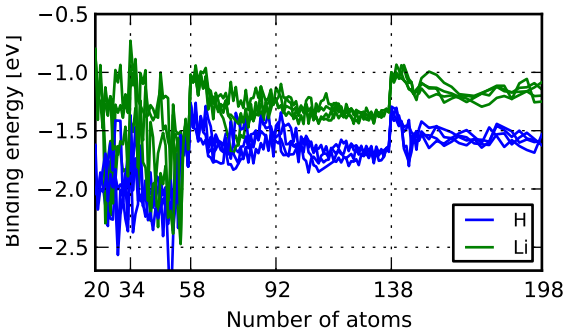

Figure 8.5: *Adsorption energy of H and Li on Au cuboctahedra as a function of cluster size. Clusters are generated with several different pseudorandom seeds.*

between electronic shells of different radial and angular dependencies results in a beat phenomenon such that major shell effects are mostly extinguished between 500-1000 atoms.[103] The supershell effect once again allows for well-resolved magic numbers for clusters larger than 1000 atoms, at which point it seems less likely for truncated octahedral clusters to have gaps. Electronic shell structure has however been observed in alkali metal clusters up to 1500 atoms, after which point geometric magic numbers corresponding to cuboctahedral or icosahedral shell closings take over.[104] This shift in character of magic numbers was attributed to solidification of the clusters. Another study has observed electronic shell structure as high as 3000 alkali atoms.[105] In conclusion it can be argued that large electronic gaps are unlikely beyond 500 atoms, but we cannot state with complete certainty that electronic effects are always insignificant.

8.4 Main-group atoms on gold

We can investigate the electronic shell effects more thoroughly by considering adsorption of several different atomic species. In this section we calculate adsorption energies of many different main-group atoms on gold cuboctahedra. These calculations are straightforward and use the same parameters as previously.

The binding energies of H and Li on Au clusters are shown on Figure 8.5. Again, magic-number clusters are universally unreactive. H and Li follow the opposite behaviour of O: past a magic number, a sharp *decrease* in binding takes place. This is not surprising for Li which has a loosely bound electron. However H would sooner be expected to receive partial charge, so this behaviour is somewhat perplexing. An existing study of H adsorption on very small Au clusters has found a similar behaviour which was deemed "anomalous".[106] We will look further into this in Chapter 9.

Figure 8.6 shows the adsorption energies of atoms of ten 2p and 3p elements. The behaviour near magic numbers is consistent with the picture of electron donation or electron acceptance: For a cluster slightly smaller than a magic number the Fermi level is low, and so the donation of an electron to an electronegative adsorbate is associated with weak adsorption energy, while

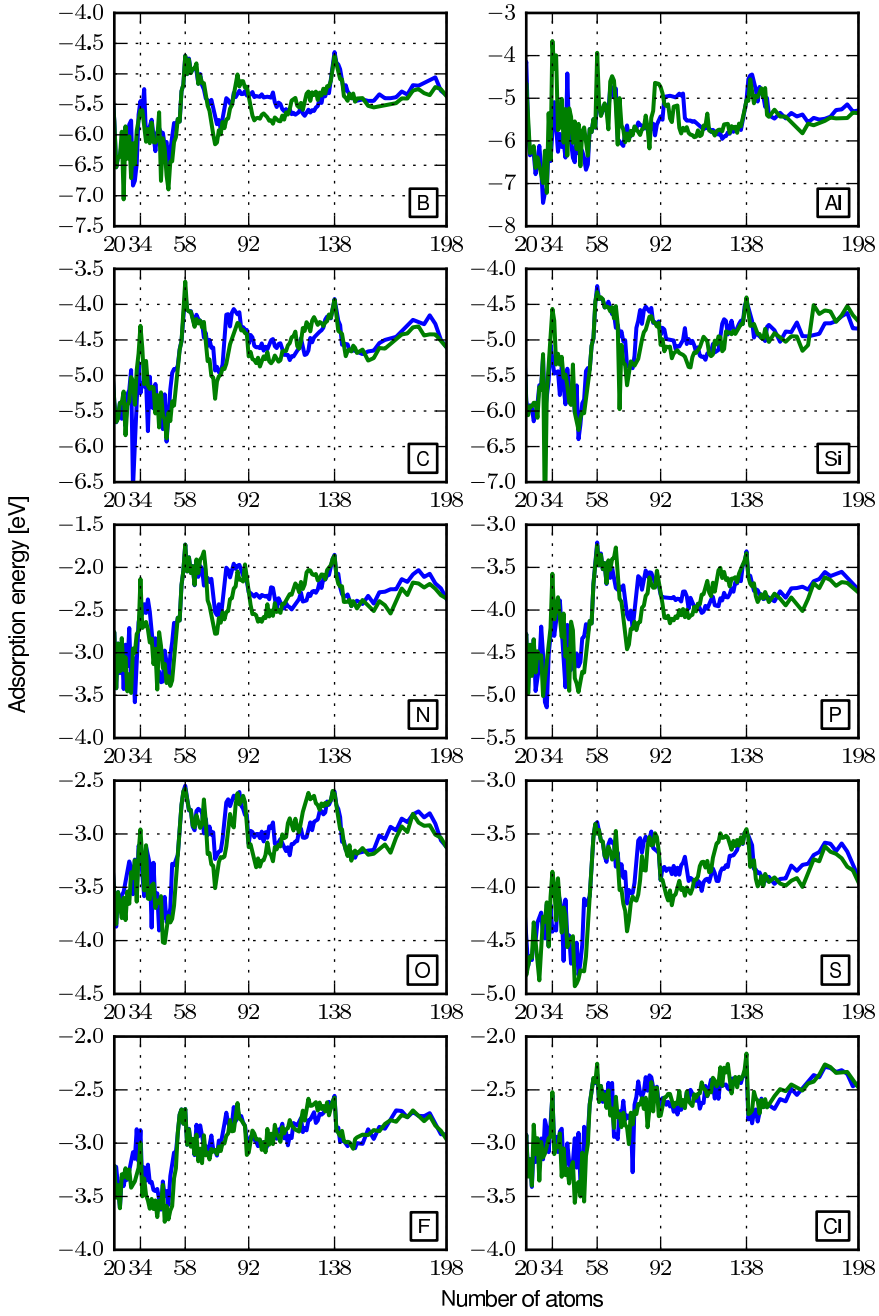

Figure 8.6: *Adsorption energy of main group elements on Au cuboctahedra as a function of cluster size. Two series of generated clusters are shown on each figure.*

the acceptance of an electron leads to strong adsorption. The opposite is the case after a magic number. The 2p elements generally have higher electronegativities than the 3p elements, and this is reflected in their adsorption energies on clusters. In general, Au clusters near magic numbers can in light of these observations be viewed as alkali-like or halogen-like. For the halogens F and Cl, the increase in energy just past a magic number is quite abrupt. For less electronegative elements (O and S) the change in energy is larger but more gradual, happening over the addition of several atoms to the cluster. This can be interpreted as a transfer of several electrons gaining more energy. Such a charge transfer interpretation should not be taken literally, however. The type of bond more closely resembles covalency as has been found for Au–S.[107] A closer analysis follows in Chapter 9.

In all cases, completion of the triangular 6-atom facet causes a sharp decrease in binding leading up to the $N = 55$ cuboctahedron. As we saw for oxygen before, $N = 92$ is not clearly distinguishable as an electronic magic number, but weak binding is generally found around $80 < N < 90$. The overall amplitude of variation can be several eV and tends to be higher for the electropositive adsorbates.

8.5 Oxygen on transition metal clusters

To expand our study in a slightly different direction, let us finally consider the trends in O adsorption for clusters of different metals. We compare the noble metals Au and Ag, plus several other transition metals with unfilled d-bands, using the same geometric series of clusters.

Figure 8.7 shows the adsorption energy of O on cuboctahedral clusters of various fcc transition metals. Pt adsorption energies are shown separately since some of the Pt clusters frequently reconstruct considerably, which causes a much more noisy trend. Structure optimizations of these Pt clusters require around three times as many steps as the 4d metals due to these significant reorganizations.

Au and Ag, having similar electronic structure, behave almost identically, with Au binding more weakly as expected. Evidently the relativistic effects of Au do not cause significant changes in the reactivity trend towards O on cuboctahedra (however the relativistic effects are known to have profound implications on cluster *structure*, and so would therefore be indirectly important in any case; relativistic effects could also be related to the tendency of Pt clusters to restructure much more than other d-band metals, although this has not been investigated).

The transition metals Ru, Rh, Pd and Pt show much simpler trend than the noble metals. Three overall size regimes can be identified.

- From around 160 atoms and above, the binding energy is mostly constant, varying by about 0.1 eV. This agrees well with the previous real-space calculations, where the changes in adsorption energy on Pt converged more smoothly with cluster size than for Au. In the d-band model, the binding energies of adsorbates is predicted to vary among transition metals. For the largest clusters (150–200 atoms), the binding strength very closely follows the filling of the d-band. The approximate fractional d-band fillings are 0.7, 0.8, 0.9 and 1.0 respectively for the series Ru–Rh–Pd/Pt–Ag/Au.

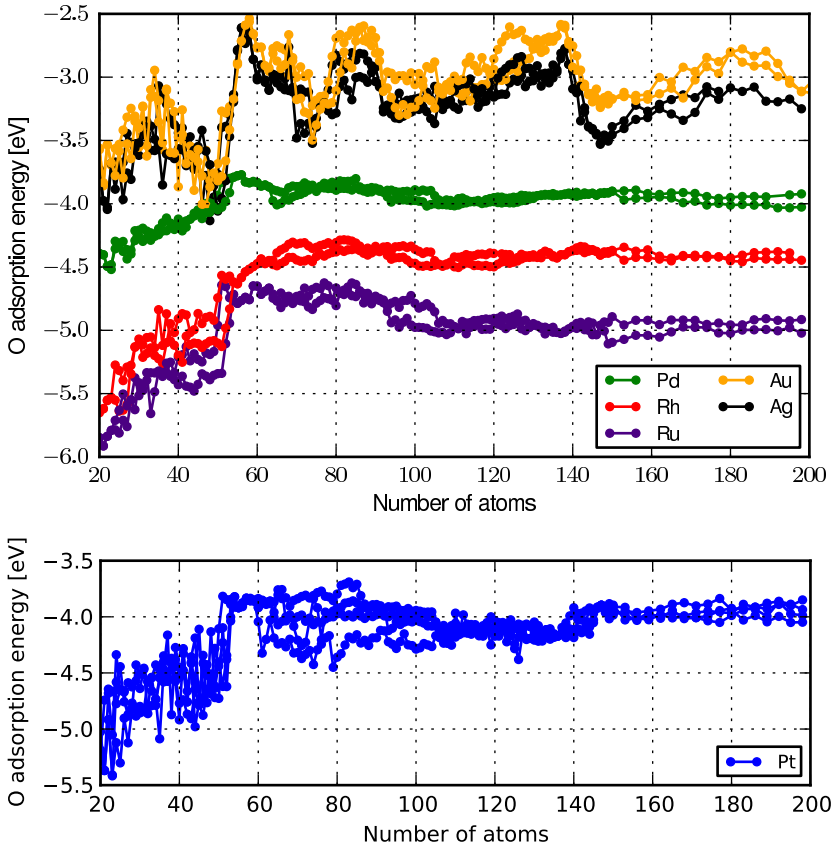

Figure 8.7: *Binding energy of O on cuboctahedral clusters of different metals as a function of cluster size.*

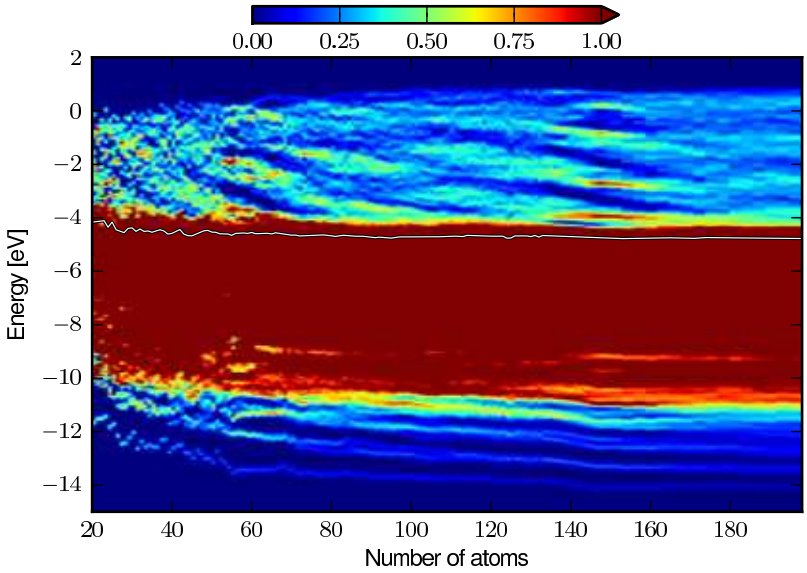

Figure 8.8: *DOS of Pt cuboctahedra as a function of cluster size and energy. The Fermi level is indicated.*

Higher filling leads to weaker binding in agreement with the d-band model (see however the discussion below).

- Between 55–100 atoms the binding is generally weaker than for smaller or larger clusters, but without any large variations (except for Pt). In this region the O atom binds to a 6-atom (111) facet. This specific site on that facet is apparently particularly unreactive: The increase in binding energy for larger clusters happens when the facet is further expanded, and the very steep change at $N \approx 50$–55 happens when the 6-atom facet is completed.

- Before the 6-atom facet is complete, the binding energy is much stronger, and generally binding energy increases steeply with size in the limit of small clusters. This can be a combination of several effects. In this region, the Fermi level and absolute d–band center both change in a similar way. The exact cause for this change may be attributable to some combination of movement of the d-band, location of the Fermi level and geometric nearest-neighbour changes. The variation of d-band location, and hence Fermi level which is pinned to the upper part of the d-band, takes place over roughly this same size range. For some reason Pd has a much weaker such variation than Ru, Rh and Pt.

The crucial chemical difference between the noble metal clusters and the remaining transition metals is clearly the electronic shell effects. Figure 8.8 shows the DOS of Pt clusters as a function of cluster size. The overall DOS is remarkably similar to that of Au, with the s-electrons forming gradually broadening subshells. However the Fermi level is located within the d-band where the DOS is very high, which locks it in place and this prevents the creation of any gaps. (Note that the atomic basis set is not expected to be accurate for

high-lying unoccupied states, and so these results do not conclusively prove persistence of shell structure among the unbound states.)

It is natural to ask to what extent the size-dependence of adsorption energies within a series of clusters of the *same* metal can be understood from the d-band model. The d-band model predicts that binding energies of adsorbates on transition metal surfaces can be understood from the filling of antibonding states on the adsorbate, with a high filling causing low binding energies.[108] A simple descriptor for the tendency of such states to be filled is usually taken to be $\epsilon_d - \epsilon_F$, the difference in energy between the weighted center of the d-projected density of states on the atoms next to the adsorbate and the Fermi level. If the Fermi level is high compared to the location of the d-band, antibonding states resulting from the hybridization of adsorbate states with the d-band will tend to lie below the Fermi level, which amongst other things explains the low reactivity of noble metals.[108] By itself this notion is clearly not sufficient to explain the trends for noble metal clusters Ag and Au, where the electronic shell structure and resulting size-dependent oscillations of the Fermi level appear to be the most important factors in the determination of adsorption energies.

For metals with unfilled d-bands, the smallest clusters have higher-lying d-bands as well as higher-lying Fermi level (this can be seen on Figure 8.8). The adsorption energy correlates to some extent with either of these quantities, but preliminary results we have not revealed any sensible or clear correlation from the combined descriptor $\epsilon_d - \epsilon_F$. The simple descriptor $\epsilon_d - \epsilon_F$ therefore does not explain the size variation of binding energies even for the metals with partially filled d-bands. The conclusion so far must be that a number of different size effects participate simultaneously to determine the adsorption energy, making the common $\epsilon_d - \epsilon_F$ descriptor less useful for clusters than for bulk systems.

Chapter 9

Analysis of chemisorption on gold clusters

We have seen how magic numbers affect the binding energy of various adsorbates on gold clusters, with clusters appearing alkali-like or halogen-like depending on the number of atoms. However a few questions are not resolved by the simple previous analysis. In particular the apparent donation of an electron by H, which would be expected to attract charge, is perplexing. A Newns–Anderson model will be applied below to better understand the bonding of different adsorbates.

9.1 The Newns–Anderson model

The Newns–Anderson model describes the chemisorption of an atom on a metal surface.[109] It is a tight-binding model which describes the hybridization of a single state $|a\rangle$ on an atom with the continuum of states $|k\rangle$ of a surface characterized by a Fermi energy ϵ_F. The model considers the Hamiltonian

$$\hat{H} = \hat{H}_0 + \hat{V}, \tag{9.1}$$

where $\hat{H}_0$ is the Hamiltonian of the uncoupled metal and adsorbate, and $\hat{V}$ describes the coupling. In the basis of uncoupled eigenstates $|k\rangle$ and $|a\rangle$, the Hamiltonian takes the form

$$\mathbf{H} = \left[\begin{array}{ccc|c} \ddots & & 0 & \vdots \\ & \epsilon_k & & v_{ka} \\ 0 & & \ddots & \vdots \\ \hline \cdots & v_{ak} & \cdots & \epsilon_a \end{array}\right], \tag{9.2}$$

where $\hat{H}_0$ and $\hat{V}$ correspond to the diagonal and off-diagonal blocks, respectively. The parameters are the uncoupled energy of the adsorbate ϵ_a, the energies ϵ_k of the metal states, and the adsorbate–metal couplings v_{ak}.

The strength of this model is, as we shall see in the following, that it can be used to attribute parts of the binding to different energy ranges, providing qualitative information which is not easily obtained from a DFT calculation. While DFT calculations themselves can provide accurate results, the self-consistency

procedure eventually results in every quantity depending on every other quantity. What we would like is a simple, more qualitative understanding, which is more easily obtained through a non-self-consistent model.

In the following we will describe a method to extract a Hamiltonian matrix from a DFT calculation using the localized basis set, which can be used within the Newns–Anderson model.

9.2 Newns–Anderson Hamiltonian from DFT

The Hamiltonian matrix calculated in the localized basis set is far from the Newns–Anderson form (9.2). In order to apply the model, we must find a way to transform the matrix.

Suppose we have calculated a Hamiltonian using DFT and apply a "small" perturbation which self-consistently would change both the Hamiltonian, density and wavefunctions. By the force theorem, since both wavefunctions and density are at variational minima, the change in energy due to this perturbation corresponds specifically to the change in Hamiltonian. Thus, from a small perturbation of a self-consistent Hamiltonian we can obtain the changes in adsorption energy knowing only the change in the Hamiltonian.

We will use this to perform a DFT calculation for a combined system including both cluster and adsorbate, then modify this Hamiltonian to obtain expressions for the uncoupled cases.

In the localized basis, the Hamiltonian calculated by DFT will consist of blocks $\mathbf{H}^M, \mathbf{H}^A, \mathbf{H}^{AM}$ and $\mathbf{H}^{MA}$ pertaining to the basis functions on the metal atoms, adsorbate and the interaction:

$$\mathbf{H}_{\mathrm{DFT}} = \begin{bmatrix} \mathbf{H}^M & \mathbf{H}^{AM} \\ \mathbf{H}^{MA} & \mathbf{H}^A \end{bmatrix}. \tag{9.3}$$

The metallic and the atomic submatrices can each be brought on diagonal form by diagonalizing them independently. Since the localized basis set is non-orthogonal, we solve the generalized eigenvalue equations involving also the overlap matrix $S_{\mu\nu}$:

$$\sum_\nu H^M_{\mu\nu} c^M_{\nu k} = \sum_\nu S^M_{\mu\nu} c^M_{\nu k} \epsilon_k, \tag{9.4}$$

$$\sum_\nu H^A_{\mu\nu} c^A_{\nu a} = \sum_\nu S^A_{\mu\nu} c^A_{\nu a} \epsilon_a. \tag{9.5}$$

Since the solutions $c^M_{\nu k}$ and $c^A_{\nu a}$ diagonalize each of the submatrices H^M and H^A, they can be used to transform the interaction blocks H^{AM}_{ak} and S^{AM}_{ak}:

$$v_{ak} = \sum_{a'k'} c^{A*}_{a'a} H^{AM}_{a'k'} c^M_{k'k}, \tag{9.6}$$

$$s_{ak} = \sum_{a'k'} c^{A*}_{a'a} H^{AM}_{a'k'} c^M_{k'k}. \tag{9.7}$$

By now the DFT-based Hamiltonian has been brought on the form (9.2) except for two issues: First of all there are several states on the atom, whereas Eq. (9.2) only allows one. We will assume that each of the atomic states hybridizes

independently, resulting in a separate Hamiltonian for each such state. This method has been used previously to describe the interaction of several molecular orbitals with metal surfaces. Second, the basis functions on the atom have an overlap $s_{ak} = \langle a|k\rangle$ with the metal states. Grimley has solved this problem in a non-orthogonal basis, and that approach will be used in the following.[110]

9.3 Binding energy from Newns–Anderson

The energy of the uncoupled metal can be written in terms of the metallic density of states $\rho(\epsilon)$, as an integral up to the Fermi level

$$E = 2\int_{-\infty}^{\epsilon_F} \rho(\epsilon)\epsilon \,\mathrm{d}\epsilon, \tag{9.8}$$

where the factor 2 denotes spin-degeneracy. Suppose now that a single atomic state couples to the metal surface, causing a change $\delta\rho(\epsilon)$ in the density of states. The change in energy can then be obtained by integrating $\delta\rho(\epsilon)\epsilon$ over the occupied states, except care must be taken to ensure that the right number of electrons is counted in this integration. First of all the adsorbate contributes a number n_a of electrons (probably 1 or 2), whose initial energy $n_a\epsilon_a$ must be subtracted. These electrons are deposited at the Fermi level ϵ_F.

Consider the integral of the induced density of states

$$\Delta N = \int_{-\infty}^{\epsilon_F} \delta\rho(\epsilon)\,\mathrm{d}\epsilon. \tag{9.9}$$

This is the number of states that have, by the chemisorption event, been introduced below the Fermi level. If this is nonzero, a number of electrons will have moved from the Fermi level down into these newly available states. Thus, a number $2\Delta N$ (counting spin) of electrons has been removed from the Fermi level. Taking these electron counting corrections into account, the adsorption energy can be written as

$$E_{\mathrm{ads}} = 2\int_{-\infty}^{\epsilon_F} \delta\rho(\epsilon)\epsilon \,\mathrm{d}\epsilon - 2\Delta N\epsilon_F + n_a(\epsilon_F - \epsilon_a). \tag{9.10}$$

The induced density of states, and thus the energy, can be calculated using Green's functions. The theory behind this will be briefly sketched next.

The Green's operator $\hat{G}(z)$ is defined for some Hamiltonian $\hat{H}$ by

$$(z - \hat{H})\hat{G}(z) = \hat{I}, \tag{9.11}$$

where $z = \epsilon + i\lambda$ is a complex number. The retarded Green's function is defined by taking the limit $\lambda \to 0+$, which will be implicit in all expressions from now on. With this convention, the matrix element $G_\alpha(\epsilon) \equiv \langle\alpha|\hat{G}(\epsilon)|\alpha\rangle$ corresponding to some state $|\alpha\rangle$ is related to the projected density of states $\rho^\alpha(\epsilon)$ through*

$$\mathrm{Im}\,\langle\alpha|\hat{G}(\epsilon)|\alpha\rangle = -i\pi\rho^\alpha(\epsilon). \tag{9.12}$$

*This uses the relation $\lim_{\lambda\to 0}\frac{1}{x+i\lambda} = \frac{\mathcal{P}}{x} - i\pi\delta(x)$, where $\mathcal{P}$ is the Cauchy principal value, known from complex analysis.

Therefore the full density of states can likewise be obtained from the trace as $\operatorname{Im}\operatorname{Tr}\hat{G}(\epsilon)$, allowing us to actually calculate binding energies. We need to calculate the Green's function $\hat{G}(\epsilon)$ of the combined system in order to be able to integrate the induced density of states and obtain a binding energy, a task which is made more complicated by the fact that the basis is non-orthogonal.

By making use of the projection operator for non-orthogonal basis sets, (4.13), the matrix elements of (9.11) are

$$\sum_{\xi\lambda} \langle\Phi_\mu|\epsilon - \hat{H}|\Phi_\xi\rangle\, S^{-1}_{\xi\lambda}\, \langle\Phi_\lambda|\hat{G}(\epsilon)|\Phi_\nu\rangle = \langle\Phi_\mu|\Phi_\nu\rangle = S_{\mu\nu}, \tag{9.13}$$

and hence in matrix notation

$$(\epsilon\mathbf{S} - \mathbf{H})\tilde{\mathbf{G}}(\epsilon) = \mathbf{I}, \quad \tilde{\mathbf{G}}(\epsilon) = \mathbf{S}^{-1}\mathbf{G}(\epsilon)\mathbf{S}^{-1}, \tag{9.14}$$

where $\tilde{\mathbf{G}}(\epsilon)$ is the usual non-orthogonal Green's function.[111] This can be rewritten as a perturbation series

$$\tilde{\mathbf{G}}(\epsilon) = \mathbf{G}^0(\epsilon) + \mathbf{G}^0(\epsilon)\mathbf{X}(\epsilon)\tilde{\mathbf{G}}(\epsilon), \tag{9.15}$$

with $\mathbf{G}^0(\epsilon)$ being the known Green's function of the uncoupled system, and

$$\mathbf{X}(\epsilon) = \mathbf{V} - \epsilon\mathbf{s}, \quad \mathbf{S} = I + \mathbf{s}. \tag{9.16}$$

Then $\mathbf{X}(\epsilon)$ contains only elements that couple between adsorbate and metal. Using the perturbation series, all matrix elements G_a, G_k, G_{ka}, G_{ak} are relatively straightforward to write down. With this change, the remaining part of the calculation mostly resembles the non-orthogonal case,[109] where the binding energy (9.10) becomes an integral

$$E_{\text{ads}} = \frac{2}{\pi}\int_{-\infty}^{\epsilon_F} \eta(\epsilon)\,\mathrm{d}\epsilon + n_a(\epsilon_F - \epsilon_a) \tag{9.17}$$

over a *phase shift* $\eta(\epsilon)$ calculated from the real and imaginary parts $\Lambda(\epsilon)$ and $\Delta(\epsilon)$ of the self-energy:

$$\tan\eta(\epsilon) = \frac{\Delta(\epsilon)}{\epsilon - \epsilon_a - \Lambda(\epsilon)}. \tag{9.18}$$

These functions are given by

$$\Delta(\epsilon,\epsilon') = \sum_k |X_{ak}(\epsilon)|^2\delta(\epsilon' - \epsilon_k), \tag{9.19}$$

$$\Lambda(\epsilon) = \mathcal{P}\!\int_{-\infty}^{\infty} \frac{\Delta(\epsilon,\epsilon')}{\epsilon - \epsilon'}\,\mathrm{d}\epsilon', \tag{9.20}$$

with the short-hand $\Delta(\epsilon) = \Delta(\epsilon,\epsilon)$.[110] The notation $\mathcal{P}\!\int$ refers to the Cauchy principal value. The ϵ and ϵ'-dependent factors in $\Delta(\epsilon,\epsilon')$ can be calculated directly from the couplings of the transformed DFT Hamiltonian and overlap matrix, and used to evaluate the rest of the quantities.

The phase shift $\eta(\epsilon)$, which determines the entire chemisorption energy except for the charge transfer terms, is related to the *cumulative induced DOS*

$$N(\epsilon) = \int_{-\infty}^{\epsilon} \delta\rho(\epsilon')\,\mathrm{d}\epsilon' = -\frac{\eta(\epsilon)}{\pi} \tag{9.21}$$

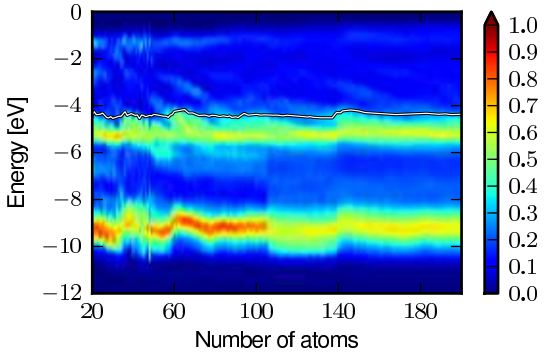

Figure 9.1: *PDOS (arb. units) for O on Au clusters as a function of energy and cluster size. The Fermi level is indicated. The most visible changes, such as the one at $N \approx 105$, happen when the local facet is modified. However the impact on binding energy is small compared to that of shell structure.*

The projected density of states on the adsorbate, which will be used in the following, can be calculated from

$$\rho_a(\epsilon) = \frac{\Delta(\epsilon)}{(\epsilon - \epsilon_a - \Lambda(\epsilon))^2 + \Delta^2(\epsilon)}. \tag{9.22}$$

9.4 Influence of d-band

Before using the full non-orthogonal model on DFT Hamiltonians, we can obtain a qualitative understanding of this model by playing around with a simple chemisorption function. The overall reactivity of different metals is well described by the d-band model, which attributes the variations to the position or filling of the d-band.

To do this we must choose the adsorbate level ϵ_a and the chemisorption function $\Delta(\epsilon)$. We will choose these values such that the projected density of states (PDOS) on the adsorbates match those calculated with DFT. Figure 9.1 shows the PDOS on the atomic basis functions of O using (4.15). The O states split into states on either side of the d-band, which can be understood as bonding and antibonding. The PDOS does not qualitatively change with cluster size, although some variations are seen near the magic numbers. In all cases, the antibonding states are largely occupied.

Assume first that the adsorbate couples to an idealized metallic s-band and d-band, where the coupling to each band can be approximated as semielliptic contributions $V_s^2\rho_s(\epsilon)$ and $V_d^2\rho_d(\epsilon)$ to $\Delta(\epsilon)$, where $\rho_s(\epsilon)$ and $\rho_d(\epsilon)$ integrate to 1. Thus

$$\Delta(\epsilon) = \pi V_s^2 \rho_s(\epsilon) + \pi V_d^2 \rho_d(\epsilon). \tag{9.23}$$

V_s and V_d determine the coupling strength. s and d bandwidths are chosen to roughly match those of real Au. On Figure 9.2a, $\Delta(\epsilon)$ (full lines) and corresponding $\Lambda(\epsilon)$ (broken lines) are shown for two different choices of semielliptic d-band.

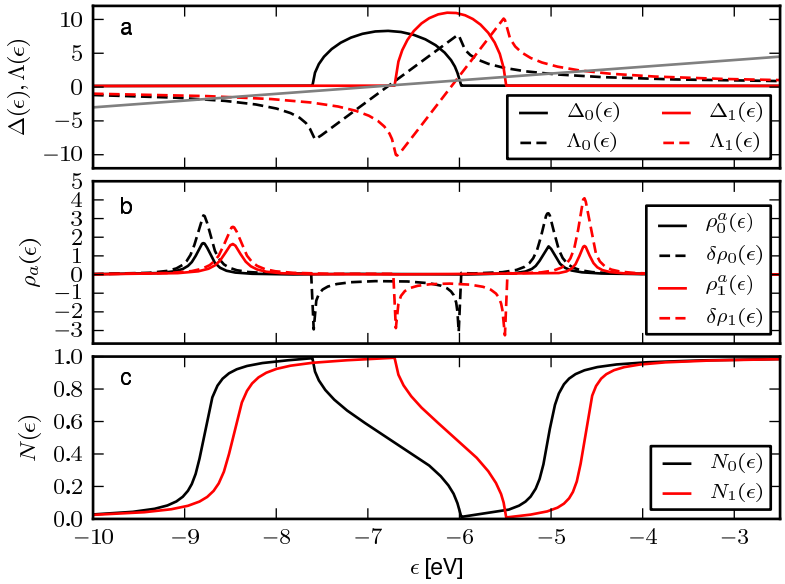

Figure 9.2: *(a) Two choices of semielliptic $\Delta(\epsilon)$ (full lines) and resulting $\Lambda(\epsilon)$ (broken lines). Bonding and antibonding states appear at intersections between $\Lambda(\epsilon)$ and the shown line $\epsilon - \epsilon_a$. (b) The projected density of states on the adsorbate showing bonding and antibonding states. (c) The cumulative induced DOS $N(\epsilon)$. (d) The adsorption energy as a function of the location of the Fermi level. If the Fermi level is located above the antibonding PDOS peak, d-band location no longer affects adsorption energy.*

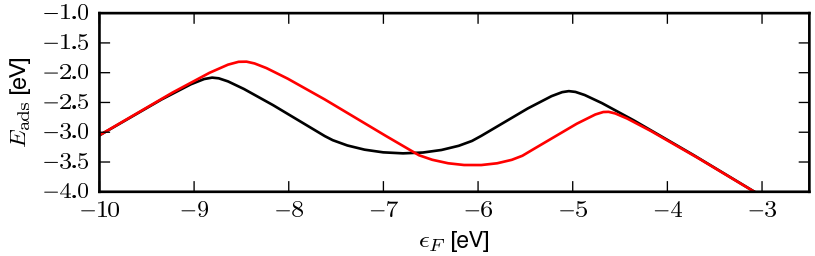

Figure 9.3: *Binding energy as a function of Fermi level for two different d-band locations. The adsorbate contributes a single electron in this example.*

One represents an ordinary Au surface while the other is shifted higher in energy and made more narrow, representing e.g. an undercoordinated site such as may be found on a cluster. The adsorbate energy level is set to $\epsilon_a = -7\,\mathrm{eV}$.

The coupling results in two states with the PDOS shown on Figure 9.2b. They correspond to clear bonding and antibonding states broadened into resonances by the s-band. Also shown is the induced DOS $\delta\rho(\epsilon)$. The bonding and antibonding states are, together and counting spins, capable of accepting four electrons. However a single state is eliminated from within the d-band, so that a total of only two extra electrons is induced. The cumulative induced DOS is shown on Figure 9.2c.

We can now calculate the binding energy, shown on Figure 9.3 as a function of the Fermi level. Clusters close to a magic-number cluster will presumably have almost the same chemisorption function, and vary only by having different Fermi levels. Considering the variation of the energy as a function of Fermi level therefore corresponds to the transition past a magic number. Since the Fermi level is located at approximately $-4.5\,\mathrm{eV}$ for Au, the binding energy varies with the Fermi level but is locally independent of the location and width of the d-band. In fact, in this simple case, *the location of the d-band affects the adsorption energy only if the Fermi level lies between the bonding and the antibonding states.*

This variation of binding energy with Fermi level agrees with the behaviour of O on Au clusters close to magic numbers. The adsorption of an O atom with two empty p-states creates states below the Fermi level that can accept two electrons in total. These two electrons are removed from the Fermi level, and therefore an increase of the Fermi level corresponds to an increase in adsorption energy by twice as much. An analysis of the occupation of the O p-states (using the DOS expression in terms of the basis functions, (4.15)) reveals that the effect of increasing the Fermi level on the cluster is not to transfer significantly more charge to the atom. Instead the increase in binding due to a higher Fermi level happens because the electrons which would *anyway* be going from the Fermi level into the induced states, can now do so from a higher-lying Fermi level.

9.5 Main-group elements

We now use the full non-orthogonal model with DFT Hamiltonians. Consider O as a first example. A DFT calculation is performed on one of the previously

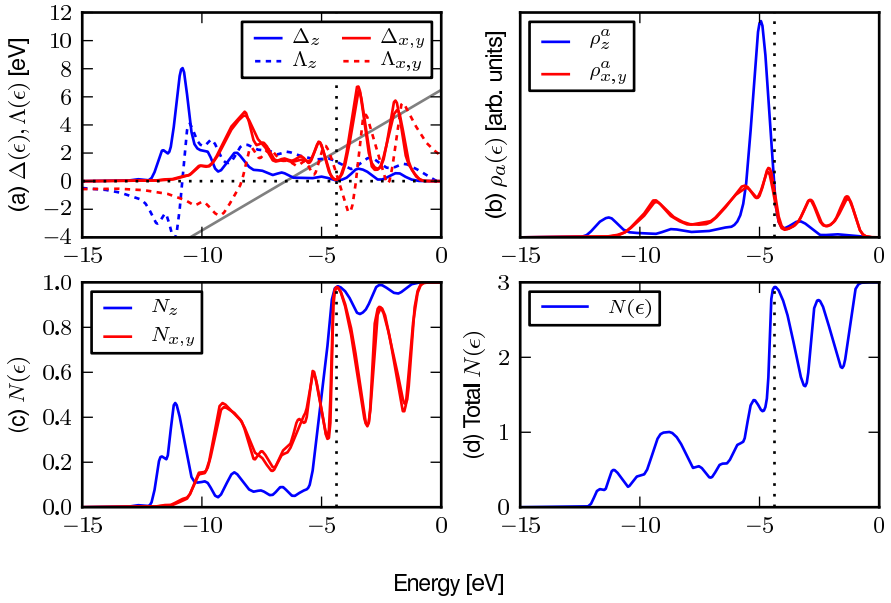

Figure 9.4: *Newns–Anderson model applied to O on Au_{58}. (a) $\Delta(\epsilon)$ and $\Lambda(\epsilon)$ for the three p states, with x and y being almost identical. The grey line is $\epsilon - \epsilon_a$ (ϵ_a of the three states lie close) whose intersections with $\Lambda(\epsilon)$ correspond to energies of created states. The Fermi level is indicated. (b) PDOS. (c) Cumulative induced DOS for each state. Total cumulative induced DOS $N(\epsilon) = N_x(\epsilon) + N_y(\epsilon) + N_z(\epsilon)$.*

relaxed Au_{58} clusters with O adsorbed on it. The DFT calculation uses the usual parameters, except we use only a single-ζ basis set for the atoms such that we only have functions for the actual atomic orbitals. From this calculation we export the overlap matrix and Hamiltonian and calculate chemisorption function and other quantities. We consider only the 2p states.

$\Delta(\epsilon)$ and $\Lambda(\epsilon)$ are shown on Figure 9.4a for the p_z state (blue) and the p_x and p_y states (red), which are degenerate and have the same coupling. The p_z state couples strongly in the region $\epsilon \approx -11\,\text{eV}$ while the two other states couple to higher energies, including the two peaks above the Fermi level that correspond to electronic shells. The resulting PDOS (Figure 9.4b) shows a clear state just below the Fermi level, like previously in Figure 9.1. Note that the exact behaviour of the PDOS above the Fermi level may not be realistic, as the atomic basis set is not well suited for higher-lying unbound states, and because the PDOS plotted here is based on (9.22) which does not account for non-orthogonality. The PDOS therefore does not cannot represent numbers of electrons, but does show in a sense the presence of states. Higher-lying peaks are generally exaggerated due to this effect.

The cumulative induced DOS $N(\epsilon)$ for each of the states is shown on Figure 9.4c. They behave in a manner consistent with the simple model considered

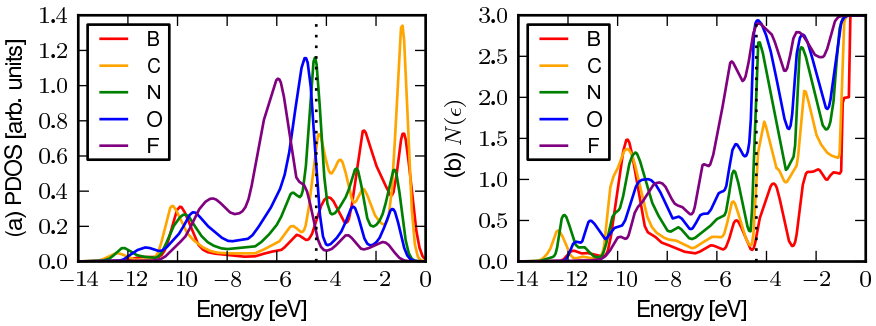

Figure 9.5: *(a) PDOS calculated as a sum over p_x, p_y and p_z for elements B–F. Splitting of the adsorbate state generally decreases with 2p filling. (b) Total $N(\epsilon)$ of the three 2p states for each of the elements B–F.*

previously: The additional states introduced into the spectrum with the bonding peaks are cancelled out by the elimination of metallic states, so that the $N(\epsilon)$ remains low e.g. at $\epsilon = -7.5\,\text{eV}$. The antibonding states, however, all lie below the Fermi energy which means a total of three extra states have been introduced in the spectrum below the Fermi level. The four electrons from O fill only two of these, and thus two electrons can be moved from the Fermi level down to the induced states. Increasing the Fermi level would thereby increase binding by twice that amount. The hybridization of each state with the unfilled electronic shells above the Fermi level can be understood as a slight movement of the states within the electronic shells. If the Fermi level had been located within these, the relationship between Fermi level and adsorption energy would have been more complicated. Thus, the simple relationship exists only because of the gap at the Fermi level. Figure 9.4d shows the sum of the cumulative induced DOS for each state, which therefore reaches 3.

Figure 9.5 shows the behaviour for the 2p elements B–F. The PDOS (Figure 9.5a) very high splitting between bonding and antibonding states for B, decreasing towards F which has only a fully occupied resonance peak. The filling of antibonding states is normally taken as the primary reason why Au binds adsorbates weakly. It is seen here that it is really $N(\epsilon)$ which contains all quantitative information, and from which conclusions can be drawn.

Finally the PDOS and $N(\epsilon)$ for H and Li are shown on Figure 9.6. Li induces a state above the Fermi level from which one electron is contributed, consistently with expectations. The H coupling is so strong that a low-lying bonding state appears at$-12\,\text{eV}$, the bottom of the s-band (a similar effect has been described in Ref. 112, while the antibonding state is above the Fermi level. Since one state is eliminated from the metallic DOS (at approximately $-10\,\text{eV}$), the total induced DOS up to the Fermi level integrates to approximately zero. The electron introduced by H therefore effectively goes on top of the Fermi level, explaining why it behaves like Li.

In conclusion, we understand from this model that the shift in adsorption energy across a magic number can be positive or negative depending on whether states are induced above or below the Fermi level. If excess states are intro-

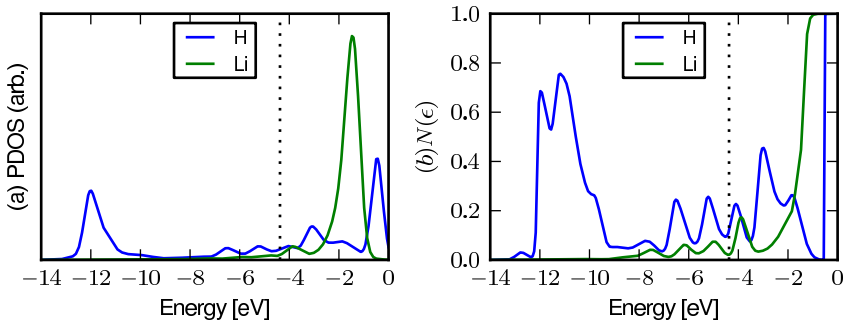

Figure 9.6: *(a) PDOS and (b) cumulative induced DOS of H and Li on* Au_{58}.

duced below the Fermi level, the increase in Fermi level associated with a magic number will allow electrons to transfer from the higher Fermi level, leading to stronger adsorption. If states are introduced above the Fermi level, the electrons controbuted by the atom must be deposited onto the Fermi level, instead leading to weaker adsorption. The case of hydrogen is explained by a strong splitting with the introduction of a low-lying bonding state far below the Fermi level, but the elimination of effectively one state from the metal below the Fermi level. Therefore hydrogen behaves like Li, though a more appropriate picture is that of a covalent bond.

Chapter 10

Electronic structure and geometry

Until now we have considered Au clusters which are based on regular structures. While these structures make it easy to compare adsorption energies since the local geometry around the adsorbate can be retained across different cluster sizes, it is not certain how well our conclusions apply to clusters with realistic structures. As previously mentioned, small Au clusters in particular form quite varied structures that are far from the regular structures considered previously. Optimizations of cluster structures based on ab-initio methods with the objective of finding the globally optimal structures are prohibitively expensive in the range of cluster sizes we are considering. However if our objective is to obtain a qualitative idea about the behaviour of real clusters (or even a realistic idea, given that finite-temperature ensembles will naturally consist of mixtures), then the exact determination of strict lowest-energy structures is not essential. In the following we perform simulated annealings on Au clusters using the simple EMT potential[113,114] implemented in ASAP,[115] and then with DFT using the localized basis sets.

10.1 Molecular dynamics

We will in the following use simulated annealing within molecular dynamics (MD) as a means to globally optimize structures. This method simulates that a collection of atoms is cooled down from above its melting point until it completely freezes, allowing the atoms to gradually arrange themselves the same way they would in nature. There exist much more efficient global optimization algorithms than simulated annealing, but since this method simulates a physical process, it will be guaranteed to produce structures which are at least in some sense physical. We acknowledge that due to the limited annealing employed here, there is a possibility that the determined shapes of clusters may be more like those found at higher temperatures. In particular the creation of regular lattices is disfavoured by this procedure.

MD simulations solve Newton's equations of motion for the atomic positions as a function of time. This requires subsequent calculations of the forces on each atom to update momenta and positions, and will preserve the total energy of

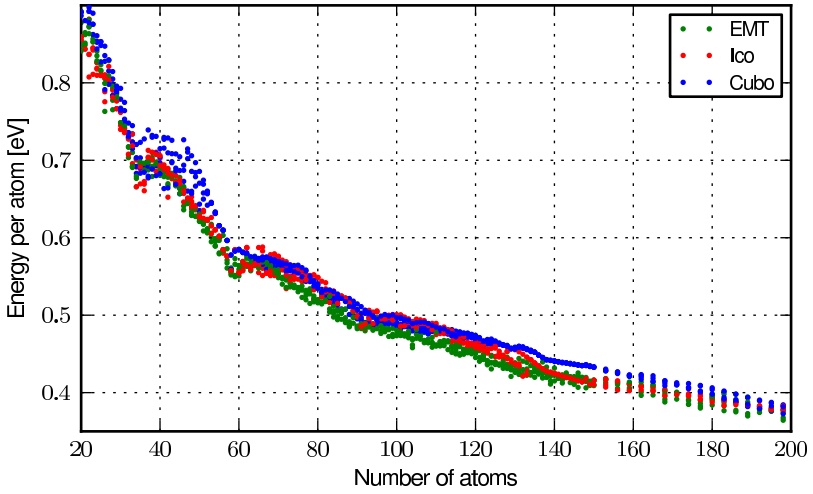

Figure 10.1: *Energy per atom of Au clusters based on simulated annealing with EMT, compared to regular cuboctahedra and icosahedra. The reference energy is bulk Au.*

the system, but not necessarily the temperature which it is more desirable for us to control. The temperature can be regulated or fixed by applying an artificial adjustment of atomic velocities on each iteration. Such a correction is called a *thermostat*. Here we use Langevin dynamics, adding a first-order damping term to Newton's equations, which for each iteration slightly adjusts the temperature towards the desired value.

10.2 Simulated annealing with EMT

For clusters of 6–200 atoms we perform a simulated annealing using the empirical potential in the ASAP code.[115] Since this is a classical potential, we would expect it to emphasize efficient atomic packing. The potential makes no reference to the concept of electrons, so the electronic structure for this series of clusters will strictly be a function of the geometric structure. The simulated annealing is performed from a starting temperature above the bulk melting point, and stops at 200 K. The temperature is lowered by 1 K for each 200 MD steps. After the annealing we perform a structure optimization using DFT with the localized basis and the usual calculation parameters. Thus we can obtain electronic spectra and total energies that can be compared to the those of previous chapters.

Figure 10.1 compares the energies of structures obtained with EMT to those of the regular cuboctahedra and icosahedra generated by the procedure from Chapter 8. Four independent annealings have been performed, and four different series of randomly generated icosahedral and cuboctahedral clusters are shown. The EMT structures generally have the lowest energies, with icosahedra being favourable to cuboctahedra within this size range. The electronic magic

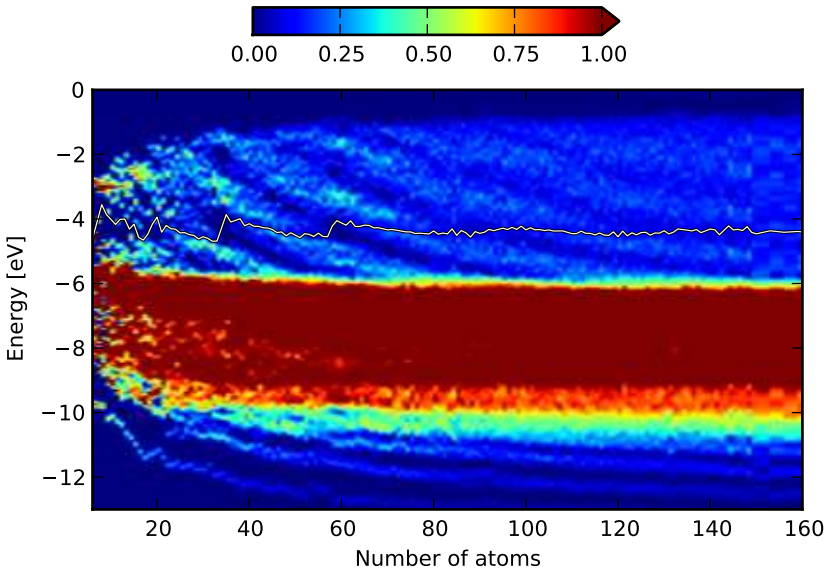

Figure 10.2: *DOS of Au clusters as a function of number of atoms and energy obtained by simulated annealing using EMT. The white line indicates the Fermi level.*

numbers 34, 58 and 92 are clearly visible as kinks with particularly low energies for all types of clusters. However, no increase in stability is seen near the geometric shell closings 55 and 147 of icosahedra and cuboctahedra. This suggests that the electronic structure is much more energetically important than efficient atomic packing, up to at least 100 atoms. Even beyond this point, the roughly optimized EMT-based clusters tend to have lower energies than the entirely regular icosahedra and cuboctahedra.

Figure 10.2 shows the spectrum as a function of cluster size, with shell structures in agreement with those of cuboctahedra and icosahedra from e.g. Figure 8.4. Large electronic gaps persists until around 90 atoms. Beyond this point the electronic shells start to overlap due to the lower symmetry compared to the icosahedra and cuboctahedra, although shell structure as a whole persists longer.

10.3 First-principles global optimization

EMT-based structures may in principle be correct to the extent that electronic structure can be somehow regarded as a strict function of geometric structure. But the results so far indicate that electronic structure is a more important factor in the total energy, and thus electronic effects are quite likely to affect the geometry even for the larger clusters. This prompts us to explicitly include electronic effects by using DFT to perform the annealing.

Due to the prodigious amount of calculations necessary, we have to make certain sacrifices of numerical precision. Several parameters lend themselves for such compromise. The annealing process itself can be shortened, the time step increased, and the temperature range narrowed. Also the DFT parameters

can be sacrificed: most importantly the grid spacing and basis set quality. The amount of vacuum surrounding the cluster must however be kept high to prevent systematically biasing compact structures. The choices described below are based on test runs for clusters about 30 atoms in size with the specific objective of determining the coarsest parameters that still yield a sane behaviour.

An MD simulation aiming for realism might use a time step of only a few fs. Higher time steps make it difficult to ensure energy conservation because of the large atomic movements with every step. We choose here to increase the time step and leave it to the thermostat to damp any energy instabilities by using a high friction coefficient of 0.06 with the Langevin implementation of ASE. Tests with the EMT potential have revealed that with a time step larger than about 30 fs, atoms will be randomly ejected from the cluster at high speed due to the poor detailed description of collisions. We have therefore chosen a time step of 24 fs, which does not exhibit such behaviour even during long simulations.

We choose the EMT-optimized clusters as starting points for the DFT annealing. The temperature must be high enough, and the number of MD steps large enough, for the end result to be independent of the initial structure. Au clusters melt at considerably lower temperatures than bulk Au. The thermodynamics of clusters have been investigated in many works, mostly based on MD simulations with empirical potentials.[61,116] The largest cluster we optimize has 150 atoms and melts at around 625 K,[63] so we start the annealing at 750 K and end it at 300 K. The temperature is high enough to entirely remodel the surface structure in all cases.

Two series of MD annealings are performed:

- A "high-quality" series for N=6–60 with grid spacing 0.24 Å and the standard dzp basis set. The temperature is lowered by 1 K every $5 + N/2$ MD steps.
- A "low-quality" series for N=6–150 with grid spacing 0.25 Å, and the same basis set except the second of the d-type orbitals is excluded. The temperature is lowered by 1 K every 20 MD steps.

Tests with further reduced basis set or grid quality tend to yield some highly picturesque structures, albeit of little scientific value. At the end of the annealing procedure, a structure relaxation is performed with the standard DFT parameters such that energies can be directly compared with previous calculations.

Many of the clusters exhibit recognizable structural motifs. The clusters with 6–9, 12 and 13 atoms are found to be planar. The clusters from 19–23 atoms consist of the extraordinarily stable Au_{20} tetrahedron[78,117,118] plus or minus a few atoms. Several of the larger clusters involve structures suggestive of tetrahedra in spite of many structural irregularities. The energy per atom as a function of the number of atoms is shown on Figure 10.3, comparing the two series of annealed clusters with the four previous series obtained from EMT. The small DFT-based clusters are, as can be expected, far lower in energy than those of EMT. The difference is smaller for larger clusters, where the short DFT annealing times tend to produce many imperfections*.

*An extremely long EMT annealing yields energies that are better than the DFT-based clusters from about 80 atoms, although the DFT clusters still prevail close to the magic numbers 92 and 138. However this procedure yields *worse* energies than those of the EMT

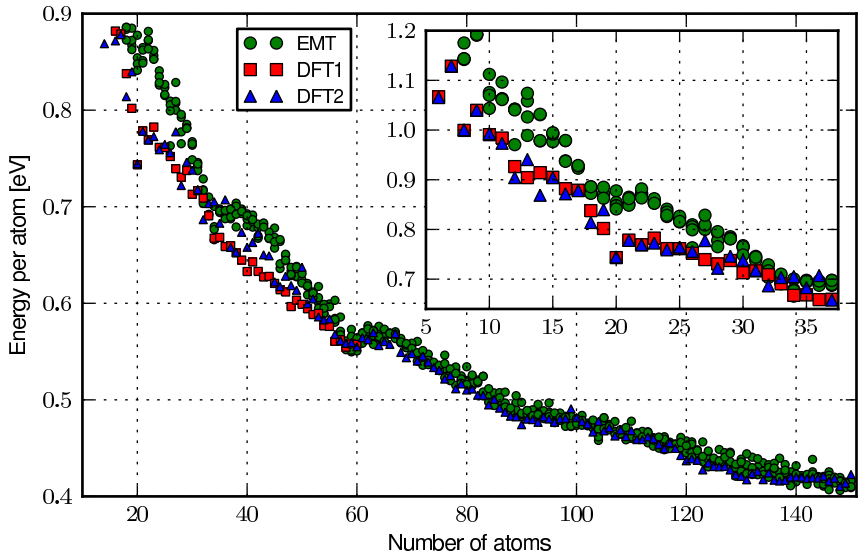

Figure 10.3: *Energy per atom for clusters obtained with simulated annealing with DFT and EMT. Inset: Magnified view for smaller clusters.*

Figure 10.4 shows the DOS as a function of cluster size and energy for the 6–60-atom series (top) and the 6–150 series (bottom). The optimization procedure tends to yield electronic gaps at the Fermi level not only at the magic-number clusters, but for almost *every* cluster. For uneven-numbered clusters, the half-filled state at the Fermi level is located in the middle of a gap between fully occupied and fully empty states. The same phenomenon has been found for other monovalent clusters.[82,119–121] The creation of such a gap is consistent with the *principle of maximum hardness*.[122,123] The energy is lowered by pushing all occupied states down, while unoccupied states are pushed up at no cost. The principle behind Jahn–Teller deformations is in many ways similar. Of particular note is the qualitative feature of the DOS that the electronic shells stay at constant energy levels for all sizes, rather than move continuously down in energy as seen for the EMT structures and regular geometries. The shell structure is greatly enhanced close to the magic numbers, resolving here into the same bands as in EMT-based or regular structures.

Figure 10.5 shows the gaps of the clusters calculated as a difference between states of charge +1 and −1. This reveals that the real magic numbers of these structures are, surprisingly, 90 and 132 rather than the expected 92 and 138. Both 90 and 132 are minor spherical shell closings of the simple jellium model presented in Chapter 6, differing respectively by an s-orbital and a p-orbital from the subsequent major shell closings. There are strong odd–even alternations due to the half-filled state for uneven clusters. These are well-known from a multitude of theoretical models.[124,125] The alternations can exist as long as the creation of a gap is possible, implying that they may be found in larger clusters as well. Alternations have been also shown in molecular adsorption energies for

annealings presented here for most of the smaller clusters. The EMT structures obtained in this range from long annealing times are mostly decahedral, with icosahedra close to $N = 147$

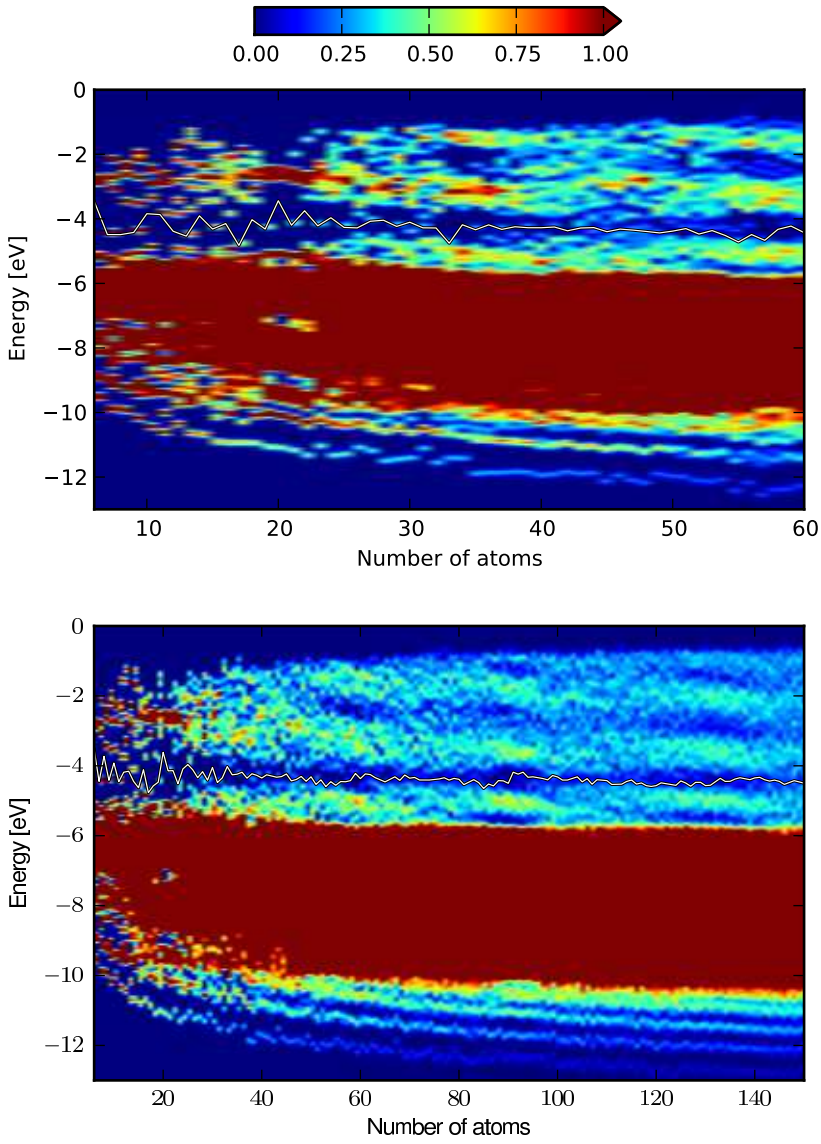

Figure 10.4: *DOS of Au clusters obtained by simulated annealing with DFT as a function of cluster size and energy. The white line indicates the Fermi level.*

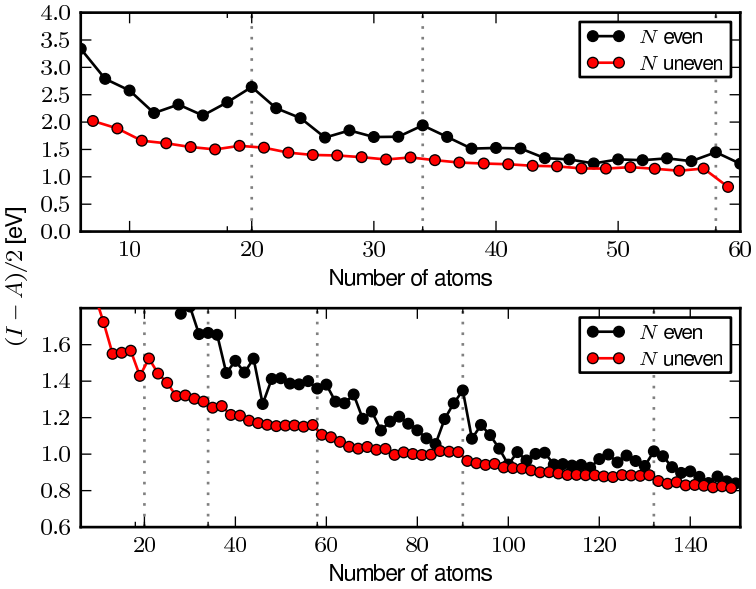

Figure 10.5: *Gaps, calculated as chemical hardness, for the two series of DFT structures. This is the difference $(I - A)/2$, where I is the ionization potential, and A is the electron affinity. Top: The 6–60-atom series. Bottom: The 6–150-atom series. For clarity, separate graphs for even and uneven clusters are shown. The dotted lines indicate the magic numbers 20, 34, 58, 90 and 132. The last two magic numbers differ from the usual major spherical jellium shell closings.*

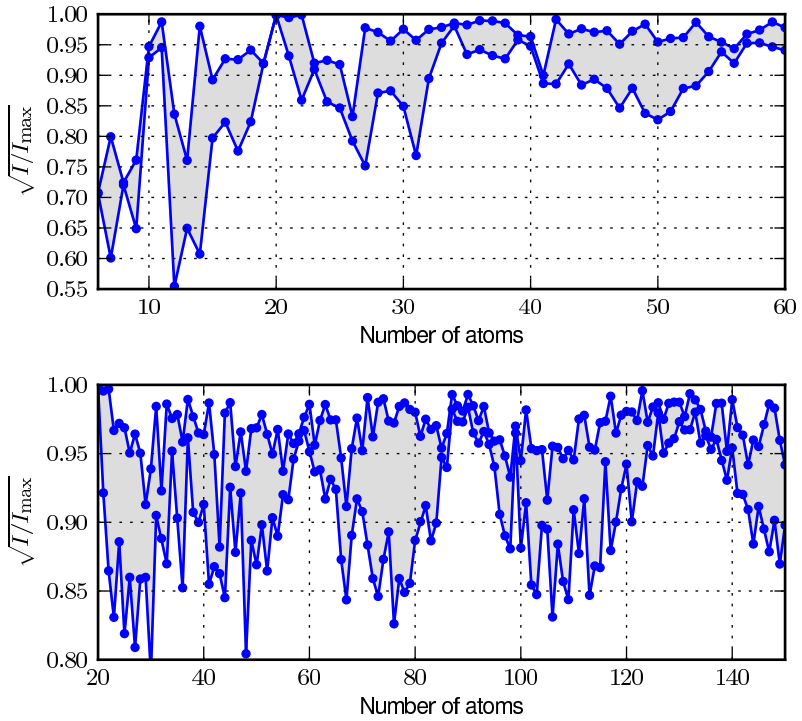

Figure 10.6: *Ratios of moments of inertia for the 6–60 (top) and 6–150 series (bottom) of DFT-annealed Au clusters. The area between the larger and the smaller moments is shaded for clarity.*

small clusters.[126–128] This would also be expected from our previous attribution of the Fermi level as a descriptor for reactivity.

Structural trends of the optimized clusters are revealed by considering their moments of inertia. For each cluster we calculate the three principal moments of inertia, $I_1 \leq I_2 \leq I_3$. Figure 10.6 shows the quantities $\sqrt{I_1/I_3}$ and $\sqrt{I_2/I_3}$ as a function of cluster size for the two series of clusters. Large deformations are characterized by large deviations of either ratio from 1. Small deformations indicate spherical or otherwise symmetric structures such as the Au_{20} tetrahedron. These deformations are similar to the well-known distortions of jellium clusters,[74] and can also emerge from tight-binding models.[119] The deformation due to shell structure is however a fundamentally non-local phenomenon which cannot be accounted for using simple atomic potentials. Recall from Figure 10.3 how the EMT potential generates structures of about the same energy as DFT *near magic numbers*, while the intermediate EMT-structures, particularly between 34 and 58 atoms, are systematically higher in energy than those obtained from DFT. The effects of electronic shell structure are essential to the determination of correct geometries of clusters well above hundred atoms in size, with deformations as large as 10–15 % even at $N = 150$ which is the largest cluster considered.

Chapter 11

Conclusion

A localized basis set implementation in GPAW has been presented which provides a very efficient alternative to the real-space code, as demonstrated by most of the results presented later in this work. More systematic testing of further of basis sets beyond dzp is desirable in the future. $\mathcal{O}(N)$ or other low-scaling methods would also be a logical next step to improve performance on systems beyond 200–300 atoms.

Using the real-space representation of GPAW, we have performed large-scale DFT calculations on Au and Pt clusters with up to 1415 atoms using 65536 cores on the BlueGene/P supercomputer at Argonne National Laboratory. From these calculations it appears that the size-dependent chemical properties of clusters, as measured by adsorption of O and CO, roughly converge with size at 600 atoms for Au and 200 atoms for Pt, although small variations within 0.1 eV of the bulk limit exist. The tendency of small clusters to bind more strongly can to some extent be understood as a geometric effect attributable to small facet sizes, although variations of adsorption energy on Au do not correlate with geometry because of profound electronic effects.

Using the basis set code, we have studied the trends in adsorption energy of atomic adsorbates on full ranges of Au cuboctahedron-based clusters, usually up to 200 atoms. It is revealed that electronic size effects relating to the jellium-like electronic structure entirely dominate the chemical properties of noble-metal clusters in this size range, with oscillations in adsorption energy on the order of 1 eV depending on adsorbate. While the DOS of the d-states varies little beyond 50 atoms, the s-states split into electronic subshells that fill one by one as cluster size increases. From calculations with several different atomic adsorbates, Au clusters can be categorized as alkali-like, noble or halogen-like depending on their number of atoms relative to magic numbers. At a magic number, the Fermi level jumps across the electronic gap into the next electronic shell, from which it is more easily donated to an adsorbate.

Transition metal clusters of Ru, Rh, Pd and Pt exhibit similar shell structure of the s-electrons, but the Fermi level is lodged within the d-band preventing any significant variation. Adsorption energies on such clusters therefore show no trace of shell structure. The main variation in binding energy on these clusters stops around 50–60 atoms when facets are sufficiently large that the local geometry around the adsorbate does not change considerably with cluster size anymore.

Using a Newns–Anderson model, we have found that the abrupt variations of adsorption energy at magic numbers can be understood from the location of adsorbate-induced states within the cluster relative to the Fermi level. For adsorbates that induce states only below the Fermi level, electrons will be transferred from the Fermi level down into the induced states, such that variations of the Fermi level directly correspond to variations of the adsorption energy. Adsorbates that only induce states above the Fermi level have the opposite behaviour. H displays a more complex behaviour, where a bonding state well below the Fermi level is cancelled by the elimination of one state from the cluster, which implies that H effectively adds an electron to the cluster.

We have performed simulated annealings of Au clusters with DFT using very coarse parameters. The shell structure is similar to the previously considered structures near the magic numbers, but differs markedly away from magic numbers. Electronic gaps at the Fermi level are created for all clusters up to 150 atoms, which is the maximum size studied. The opening of gaps is facilitated by large geometric deformations of the clusters, with magic-number clusters being spherical and other clusters being mostly oblate. The complex relationship between electronic and geometric effects persists with deformations of 10–15 % well beyond 100 atoms.

Bibliography

[1] P. Hohenberg and W. Kohn, "Inhomogeneous electron gas," *Phys. Rev.*, vol. 136, pp. B864–B871, Nov 1964.

[2] W. Kohn and L. J. Sham, "Self-consistent equations including exchange and correlation effects," *Phys. Rev.*, vol. 140, pp. A1133–A1138, Nov 1965.

[3] P. E. Blöchl, "Projector augmented-wave method," *Phys. Rev. B*, vol. 50, pp. 17953–17979, Dec 1994.

[4] P. E. Blöchl, C. J. Först, and J. Schimpl, "Projector augmented wave method: ab initio molecular dynamics with full wave functions," *Bulletin of Materials Science*, vol. 26, pp. 33–41, Jan. 2003.

[5] J. J. Mortensen, L. B. Hansen, and K. W. Jacobsen, "Real-space grid implementation of the projector augmented wave method," *Phys. Rev. B*, vol. 71, p. 035109, JAN 2005.

[6] J. Enkovaara, C. Rostgaard, J. J. Mortensen, J. Chen, M. Dułak, L. Ferrighi, J. Gavnholt, C. Glinsvad, V. Haikola, H. A. Hansen, H. H. Kristoffersen, M. Kuisma, A. H. Larsen, L. Lehtovaara, M. Ljungberg, O. Lopez-Acevedo, P. G. Moses, J. Ojanen, T. Olsen, V. Petzold, N. A. Romero, J. Stausholm-Møller, M. Strange, G. A. Tritsaris, M. Vanin, M. Walter, B. Hammer, H. Häkkinen, G. K. H. Madsen, R. M. Nieminen, J. K. Nørskov, M. Puska, T. T. Rantala, J. Schiøtz, K. S. Thygesen, and K. W. Jacobsen, "Electronic structure calculations with GPAW: a real-space implementation of the projector augmented-wave method," *Journal of Physics: Condensed Matter*, vol. 22, no. 25, p. 253202, 2010.

[7] A. H. Larsen, M. Vanin, J. J. Mortensen, K. S. Thygesen, and K. W. Jacobsen, "Localized atomic basis set in the projector augmented wave method," *Phys. Rev. B*, vol. 80, p. 195112, Nov 2009.

[8] E. Artacho, D. Sanchez-Portal, P. Ordejon, A. Garcia, and J. M. Soler, "Linear-scaling ab-initio calculations for large and complex systems," *arXiv:cond-mat/9904159*, Apr. 1999.

[9] J. M. Soler, E. Artacho, J. D. Gale, A. García, J. Junquera, P. Ordejón, and D. Sánchez-Portal, "The SIESTA method for ab initio order- n materials simulation," *Journal of Physics: Condensed Matter*, vol. 14, pp. 2745–2779, Mar. 2002.

[10] J. Chen, J. S. Hummelshøj, K. S. Thygesen, J. S. Myrdal, J. K. Nørskov, and T. Vegge, "The role of transition metal interfaces on the electronic transport in lithium–air batteries," *Catalysis Today*, vol. 165, no. 1, pp. 2 – 9, 2011.

[11] P. Pyykkö, "Theoretical chemistry of gold," *Angewandte Chemie International Edition*, vol. 43, no. 34, p. 4412–4456, 2004.

[12] P. Pyykkö, "Theoretical chemistry of gold. II," *Inorganica chimica acta*, vol. 358, no. 14, p. 4113–4130, 2005.

[13] P. Pyykkö, "Theoretical chemistry of gold. III," *Chemical Society Reviews*, vol. 37, no. 9, p. 1967–1997, 2008.

[14] P. Pyykkö and J. P. Desclaux, "Relativity and the periodic system of elements," *Accounts of Chemical Research*, vol. 12, no. 8, pp. 276–281, 1979.

[15] P. Pyykkö, "Relativistic effects in structural chemistry," *Chem. Rev.*, vol. 88, no. 3, pp. 563–594, 1988.

[16] H. Schmidbaur, S. Cronje, B. Djordjevic, and O. Schuster, "Understanding gold chemistry through relativity," *Chemical Physics*, vol. 311, pp. 151–161, Apr. 2005.

[17] H. Grönbeck and P. Broqvist, "Comparison of the bonding in Au_8 and Cu_8: A density functional theory study," *Phys. Rev. B*, vol. 71, p. 073408, Feb 2005.

[18] L. Xiao and L. Wang, "From planar to three-dimensional structural transition in gold clusters and the spin–orbit coupling effect," *Chemical Physics Letters*, vol. 392, no. 4-6, pp. 452 – 455, 2004.

[19] E. M. Fernández, J. M. Soler, and L. C. Balbás, "Planar and cagelike structures of gold clusters: Density-functional pseudopotential calculations," *Phys. Rev. B*, vol. 73, p. 235433, Jun 2006.

[20] W. D. Knight, K. Clemenger, W. A. de Heer, W. A. Saunders, M. Y. Chou, and M. L. Cohen, "Electronic shell structure and abundances of sodium clusters," *Physical Review Letters*, vol. 52, p. 2141, June 1984.

[21] M. Y. Chou, A. Cleland, and M. L. Cohen, "Total energies, abundances, and electronic shell structure of lithium, sodium, and potassium clusters," *Solid State Communications*, vol. 52, pp. 645–648, Nov. 1984.

[22] I. Katakuse, T. Ichihara, Y. Fujita, T. Matsuo, T. Sakurai, and H. Matsuda, "Mass distributions of copper, silver and gold clusters and electronic shell structure," *International Journal of Mass Spectrometry and Ion Processes*, vol. 67, pp. 229–236, Nov. 1985.

[23] M. Walter, J. Akola, O. Lopez-Acevedo, P. D. Jadzinsky, G. Calero, C. J. Ackerson, R. L. Whetten, H. Grönbeck, and H. Häkkinen, "A unified view of ligand-protected gold clusters as superatom complexes," *Proceedings of the National Academy of Sciences*, vol. 105, pp. 9157 –9162, July 2008.

[24] M. B. Knickelbein, "Reactions of transition metal clusters with small molecules1," *Annual Review of Physical Chemistry*, vol. 50, no. 1, pp. 79–115, 1999.

[25] M. Vanin, "Projector augmented wave calculations with localized basis sets," Master's thesis, 2007.

[26] A. H. Larsen, "Localized basis sets in the projector augmented wave method," Master's thesis, 2007.

[27] W. Kohn, "Nobel lecture: Electronic structure of matter—wave functions and density functionals," *Reviews of Modern Physics*, vol. 71, pp. 1253–1266, Oct. 1999.

[28] J. P. Perdew, K. Burke, and M. Ernzerhof, "Generalized gradient approximation made simple," *Physical Review Letters*, vol. 77, pp. 3865–3868, Oct. 1996.

[29] B. Hammer, L. B. Hansen, and J. K. Nørskov, "Improved adsorption energetics within density-functional theory using revised Perdew-Burke-Ernzerhof functionals," *Phys. Rev. B*, vol. 59, pp. 7413–7421, Mar 1999.

[30] C. Hartwigsen, S. Goedecker, and J. Hutter, "Relativistic separable dual-space Gaussian pseudopotentials from H to Rn," *Phys. Rev. B*, vol. 58, pp. 3641–3662, Aug 1998.

[31] L. Kleinman and D. M. Bylander, "Efficacious form for model pseudopotentials," *Physical Review Letters*, vol. 48, pp. 1425–1428, May 1982.

[32] M. Teter, "Additional condition for transferability in pseudopotentials," *Phys. Rev. B*, vol. 48, pp. 5031–5041, Aug 1993.

[33] X. Gonze, P. Käckell, and M. Scheffler, "Ghost states for separable, norm-conserving, ab initio pseudopotentials," *Physical Review B*, vol. 41, pp. 12264–12267, June 1990.

[34] D. Vanderbilt, "Soft self-consistent pseudopotentials in a generalized eigenvalue formalism," *Physical Review B*, vol. 41, pp. 7892–7895, Apr. 1990.

[35] G. Kresse and J. Furthmüller, "Efficient iterative schemes for ab initio total-energy calculations using a plane-wave basis set," *Physical Review B*, vol. 54, pp. 11169–11186, Oct. 1996.

[36] G. Kresse and D. Joubert, "From ultrasoft pseudopotentials to the projector augmented-wave method," *Physical Review B*, vol. 59, pp. 1758–1775, Jan. 1999.

[37] C. Rostgaard, "The projector augmented-wave method," *arXiv:0910.1921*, Oct. 2009.

[38] M. Kuisma, J. Ojanen, J. Enkovaara, and T. T. Rantala, "Kohn-sham potential with discontinuity for band gap materials," *Phys. Rev. B*, vol. 82, p. 115106, Sep 2010.

[39] P. Pulay, "Convergence acceleration of iterative sequences. The case of SCF iteration," *Chemical Physics Letters*, vol. 73, no. 2, pp. 393 – 398, 1980.

[40] T. Takeda, "The scalar relativistic approximation," *Zeitschrift für Physik B Condensed Matter and Quanta*, vol. 32, pp. 43–48, Mar. 1978.

[41] J. Junquera, O. Paz, D. Sánchez-Portal, and E. Artacho, "Numerical atomic orbitals for linear-scaling calculations," *Physical Review B*, vol. 64, p. 235111, Nov. 2001.

[42] S. R. Bahn and K. W. Jacobsen, "An object-oriented scripting interface to a legacy electronic structure code," *Comput. Sci. Eng.*, vol. 4, pp. 56–66, MAY-JUN 2002.

[43] S. Goedecker, "Linear scaling electronic structure methods," *Rev. Mod. Phys.*, vol. 71, pp. 1085–1123, Jul 1999.

[44] J. Choi, J. J. Dongarra, R. Pozo, and D. W. Walker, "ScaLAPACK: a scalable linear algebra library for distributed memory concurrent computers," in *Frontiers of Massively Parallel Computation, 1992., Fourth Symposium on the*, pp. 120–127, IEEE, Oct. 1992.

[45] L. Blackford, A. Cleary, J. Choi, E. D'Azevedo, J. Demmel, I. Dhillon, J. Dongarra, S. Hammarling, G. Henry, A. Petitet, *et al.*, *ScaLAPACK users' guide*, vol. 4. Society for Industrial Mathematics, 1997.

[46] E. Anderson, A. Benzoni, J. Dongarra, S. Moulton, S. Ostrouchov, B. Tourancheau, and R. van de Geijn, "Basic linear algebra communication subprograms," in *Distributed Memory Computing Conference, 1991. Proceedings., The Sixth*, pp. 287 –290, apr-1 may 1991.

[47] O. F. Sankey and D. J. Niklewski, "Ab initio multicenter tight-binding model for molecular-dynamics simulations and other applications in covalent systems," *Physical Review B*, vol. 40, no. 6, p. 3979, 1989.

[48] `https://wiki.fysik.dtu.dk/niflheim`.

[49] M. Haruta, T. Kobayashi, H. Sano, and N. Yamada, "Novel gold catalysts for the oxidation of carbon monoxide at a temperature far below 0.DEG.C.," *Chemistry Letters*, pp. 405–408, 1987.

[50] M. Haruta, S. Tsubota, T. Kobayashi, H. Kageyama, M. J. Genet, and B. Delmon, "Low-Temperature oxidation of CO over gold supported on TiO2, [alpha]-Fe2O3, and Co3O4," *Journal of Catalysis*, vol. 144, pp. 175–192, Nov. 1993.

[51] M. Valden, X. Lai, and D. W. Goodman, "Onset of catalytic activity of gold clusters on titania with the appearance of nonmetallic properties," *Science*, vol. 281, no. 5383, pp. 1647 –1650, 1998.

[52] H. Masatake, "Size- and support-dependency in the catalysis of gold," *Catalysis Today*, vol. 36, pp. 153–166, Apr. 1997.

[53] G. Mills, M. S. Gordon, and H. Metiu, "Oxygen adsorption on au clusters and a rough au(111) surface: The role of surface flatness, electron confinement, excess electrons, and band gap," *The Journal of Chemical Physics*, vol. 118, p. 4198, 2003.

[54] N. Lopez, T. Janssens, B. Clausen, Y. Xu, M. Mavrikakis, T. Bligaard, and J. Nørskov, "On the origin of the catalytic activity of gold nanoparticles for low-temperature CO oxidation," *Journal of Catalysis*, vol. 223, pp. 232–235, Apr. 2004.

[55] B. Hvolbæk, T. V. Janssens, B. S. Clausen, H. Falsig, C. H. Christensen, and J. K. Nørskov, "Catalytic activity of au nanoparticles," *Nano Today*, vol. 2, pp. 14–18, Aug. 2007.

[56] H. Falsig, B. Hvolbæk, I. S. Kristensen, T. Jiang, T. Bligaard, C. H. Christensen, and J. K. Nørskov, "Trends in the catalytic CO oxidation activity of nanoparticles," *Angewandte Chemie*, vol. 120, pp. 4913–4917, June 2008.

[57] A. S. Barnard, X. M. Lin, and L. A. Curtiss, "Equilibrium morphology of Face-Centered cubic gold nanoparticles >3 nm and the shape changes induced by temperature," *The Journal of Physical Chemistry B*, vol. 109, pp. 24465–24472, Dec. 2005.

[58] C. L. Cleveland, U. Landman, T. G. Schaaff, M. N. Shafigullin, P. W. Stephens, and R. L. Whetten, "Structural evolution of smaller gold nanocrystals: The truncated decahedral motif," *Phys. Rev. Lett.*, vol. 79, pp. 1873–1876, Sep 1997.

[59] F. Baletto, R. Ferrando, A. Fortunelli, F. Montalenti, and C. Mottet, "Crossover among structural motifs in transition and noble-metal clusters," *The Journal of Chemical Physics*, vol. 116, p. 3856, 2002.

[60] T. P. Martin, "Shells of atoms," *Physics Reports*, vol. 273, pp. 199–241, Aug. 1996.

[61] F. Baletto and R. Ferrando, "Structural properties of nanoclusters: Energetic, thermodynamic, and kinetic effects," *Rev. Mod. Phys.*, vol. 77, pp. 371–423, May 2005.

[62] C. L. Cleveland, W. D. Luedtke, and U. Landman, "Melting of gold clusters: Icosahedral precursors," *Phys. Rev. Lett.*, vol. 81, pp. 2036–2039, Sep 1998.

[63] C. L. Cleveland, W. D. Luedtke, and U. Landman, "Melting of gold clusters," *Physical Review B*, vol. 60, no. 7, p. 5065, 1999.

[64] A. P. Sutton and J. Chen, "Long-range finnis–sinclair potentials," *Philosophical Magazine Letters*, vol. 61, no. 3, pp. 139–146, 1990.

[65] R. P. Gupta, "Lattice relaxation at a metal surface," *Phys. Rev. B*, vol. 23, pp. 6265–6270, Jun 1981.

[66] X. Shao, X. Liu, and W. Cai, "Structural optimization of silver clusters up to 80 atoms with gupta and Sutton-Chen potentials," *Journal of Chemical Theory and Computation*, vol. 1, pp. 762–768, July 2005.

[67] M. Y. Chou and M. L. Cohen, "Electronic shell structure in simple metal clusters," *Physics Letters A*, vol. 113, pp. 420–424, Jan. 1986.

[68] M. P. Iñiguez, J. A. Alonso, and L. C. Balbas, "Magic numbers of sodium clusters," *Solid State Communications*, vol. 57, pp. 85–88, Jan. 1986.

[69] W. D. Knight, W. A. De Heer, W. A. Saunders, K. Clemenger, M. Y. Chou, and M. L. Cohen, "Alkali metal clusters and the jellium model," *Chemical Physics Letters*, vol. 134, pp. 1–5, Feb. 1987.

[70] Z. Penzar and W. Ekardt, "Electronic shell structure and metal clusters: the self-consistent spheroidal jellium model," *Zeitschrift für Physik D Atoms, Molecules and Clusters*, vol. 17, pp. 69–72, Mar. 1990.

[71] T. Hirschmann, M. Brack, and J. Meyer, "Spheroidally deformed sodium clusters in the selfconsistent jellium model," *Annalen der Physik*, vol. 506, no. 5, pp. 336–369, 1994.

[72] M. Brack, "The physics of simple metal clusters: self-consistent jellium model and semiclassical approaches," *Rev. Mod. Phys.*, vol. 65, pp. 677–732, Jul 1993.

[73] W. A. de Heer, W. Knight, M. Chou, and M. L. Cohen, "Electronic shell structure and metal clusters," in *Advances in Research and Applications* (H. Ehrenreich and D. Turnbull, eds.), vol. 40 of *Solid State Physics*, pp. 93 – 181, Academic Press, 1987.

[74] K. Clemenger, "Ellipsoidal shell structure in free-electron metal clusters," *Physical Review B*, vol. 32, p. 1359, July 1985.

[75] Z. Penzar and W. Ekardt, "The self-consistent spheroidal jellium model of open-shell monovalent metal clusters," *Zeitschrift für Physik D Atoms, Molecules and Clusters*, vol. 19, pp. 109–111, Mar. 1991.

[76] C. Yannouleas and U. Landman, "Electronic shell effects in triaxially deformed metal clusters: A systematic interpretation of experimental observations," *Physical Review B*, vol. 51, p. 1902, Jan. 1995.

[77] M. Koskinen, P. O. Lipas, and M. Manninen, "Electron-gas clusters: the ultimate jellium model," *Zeitschrift für Physik D Atoms, Molecules and Clusters*, vol. 35, pp. 285–297, Dec. 1995.

[78] S. M. Reimann, M. Koskinen, H. Häkkinen, P. E. Lindelof, and M. Manninen, "Magic triangular and tetrahedral clusters," *Physical Review B*, vol. 56, p. 12147, Nov. 1997.

[79] E. Hückel, "Quantentheoretische Beiträge zum Benzolproblem," *Zeitschrift für Physik A Hadrons and Nuclei*, vol. 70, pp. 204–286, 1931. 10.1007/BF01339530.

[80] E. Hückel, "Quantentheoretische Beiträge zum Problem der aromatischen und ungesättigten Verbindungen. III," *Zeitschrift für Physik A Hadrons and Nuclei*, vol. 76, pp. 628–648, 1932. 10.1007/BF01341936.

[81] Y. Wang, T. F. George, D. M. Lindsay, and A. C. Beri, "The Hückel model for small metal clusters. I. Geometry, stability, and relationship to graph theory," *The Journal of Chemical Physics*, vol. 86, p. 3493, 1987.

[82] H. Grönbeck and A. Rosén, "Chemisorption of molecular oxygen on small copper clusters and the Cu(100) surface," *Computational Materials Science*, vol. 2, no. 3-4, pp. 607 – 614, 1994.

[83] J. Mansikka-aho, M. Manninen, and E. Hammarén, "On the shell structure and geometry of monovalent metal clusters," *Zeitschrift für Physik D Atoms, Molecules and Clusters*, vol. 21, pp. 271–279, 1991. 10.1007/BF01426385.

[84] J. Mansikka-aho, M. Manninen, and E. Hammarén, "Level-spacing distribution in the tight-binding model of fcc clusters," *Physical Review B*, vol. 47, p. 10675, Apr. 1993.

[85] L. Xiao, B. Tollberg, X. Hu, and L. Wang, "Structural study of gold clusters," *The Journal of Chemical Physics*, vol. 124, no. 11, p. 114309, 2006.

[86] X. Xing, B. Yoon, U. Landman, and J. H. Parks, "Structural evolution of Au nanoclusters: From planar to cage to tubular motifs," *Phys. Rev. B*, vol. 74, p. 165423, Oct 2006.

[87] L. Ferrighi, B. Hammer, and G. K. H. Madsen, "2D-3D transition for cationic and anionic gold clusters: a kinetic energy density functional study.," *Journal of the American Chemical Society*, vol. 131, pp. 10605–10609, Aug. 2009.

[88] E. M. Fernández, J. M. Soler, I. L. Garzón, and L. C. Balbás, "Trends in the structure and bonding of noble metal clusters," *Physical Review B*, vol. 70, p. 165403, Oct. 2004.

[89] E. M. Fernández, J. M. Soler, I. L. Garzón, and L. C. Balbás, "Trends in the structure and bonding of neutral and charged noble metal clusters," *International Journal of Quantum Chemistry*, vol. 101, pp. 740–745, Jan. 2005.

[90] H.-Y. Zhao, H. Ning, J. Wang, X.-J. Su, X.-G. Guo, and Y. Liu, "Structural evolution of Au_n (n=20-32) clusters: Lowest-lying structures and relativistic effects," *Physics Letters A*, vol. 374, no. 8, pp. 1033 – 1038, 2010.

[91] W. Yin, X. Gu, and X. Gong, "Magic number 32 and 90 of metal clusters: A shell jellium model study," *Solid State Communications*, vol. 147, pp. 323–326, Aug. 2008.

[92] W. Huang, M. Ji, C. Dong, X. Gu, L. Wang, X. G. Gong, and L. Wang, "Relativistic effects and the unique Low-Symmetry structures of gold nanoclusters," *ACS Nano*, vol. 2, pp. 897–904, May 2008.

[93] H. Häkkinen, M. Moseler, O. Kostko, N. Morgner, M. A. Hoffmann, and B. v. Issendorff, "Symmetry and electronic structure of Noble-Metal nanoparticles and the role of relativity," *Physical Review Letters*, vol. 93, no. 9, p. 093401, 2004.

[94] H. Häkkinen and M. Moseler, "55-Atom clusters of silver and gold: Symmetry breaking by relativistic effects," *Computational Materials Science*, vol. 35, pp. 332–336, Mar. 2006.

[95] I. L. Garzón, K. Michaelian, M. R. Beltrán, A. Posada-Amarillas, P. Ordejón, E. Artacho, D. Sánchez-Portal, and J. M. Soler, "Lowest energy structures of gold nanoclusters," *Physical Review Letters*, vol. 81, no. 8, p. 1600, 1998.

[96] E. M. Fernández, J. M. Soler, and L. C. Balbás, "Planar and cagelike structures of gold clusters: Density-functional pseudopotential calculations," *Physical Review B*, vol. 73, p. 235433, June 2006.

[97] A. S. Barnard and L. A. Curtiss, "Predicting the shape and structure of Face-Centered cubic gold nanocrystals smaller than 3 nm," *ChemPhysChem*, vol. 7, pp. 1544–1553, July 2006.

[98] J. Kleis, J. Greeley, N. Romero, V. Morozov, H. Falsig, A. Larsen, J. Lu, J. Mortensen, M. Dułak, K. Thygesen, J. Nørskov, and K. Jacobsen, "Finite size effects in chemical bonding: From small clusters to solids," *Catalysis Letters*, vol. 141, pp. 1067–1071, 2011. 10.1007/s10562-011-0632-0.

[99] H. Boyen, G. Kästle, F. Weigl, B. Koslowski, C. Dietrich, P. Ziemann, J. P. Spatz, S. Riethmüller, C. Hartmann, M. Möller, G. Schmid, M. G. Garnier, and P. Oelhafen, "Oxidation-Resistant gold-55 clusters," *Science*, vol. 297, no. 5586, pp. 1533 –1536, 2002.

[100] M. Turner, V. B. Golovko, O. P. H. Vaughan, P. Abdulkin, A. Berenguer-Murcia, M. S. Tikhov, B. F. G. Johnson, and R. M. Lambert, "Selective oxidation with dioxygen by gold nanoparticle catalysts derived from 55-atom clusters," *Nature*, vol. 454, no. 7207, pp. 981–983, 2008.

[101] J. Mansikka-aho, E. Hammarén, and M. Manninen, "Shell structure in large nonspherical metal clusters," *Physical Review B*, vol. 46, p. 12649, Nov. 1992.

[102] L. Magaud, S. N. Khanna, and P. Jena, "Limitation on the success of the jellium model for metal clusters," *Chemical Physics Letters*, vol. 183, pp. 333–336, Sept. 1991.

[103] O. Genzken and M. Brack, "Temperature dependence of supershells in large sodium clusters," *Physical Review Letters*, vol. 67, p. 3286, Dec. 1991.

[104] T. P. Martin, T. Bergmann, H. Göhlich, and T. Lange, "Electronic shells and shells of atoms in metallic clusters," *Zeitschrift für Physik D Atoms, Molecules and Clusters*, vol. 19, pp. 25–29, Mar. 1991.

[105] J. Pedersen, S. Bjørnholm, J. Borggreen, K. Hansen, T. Martin, and H. Rasmussen, "Observation of quantum supershells in clusters of sodium atoms," *Nature*, vol. 353, no. 6346, p. 733–735, 1991.

[106] S. Buckart, G. Ganteför, Y. D. Kim, and P. Jena, "Anomalous behavior of atomic hydrogen interacting with gold clusters," *Journal of the American Chemical Society*, vol. 125, pp. 14205–14209, Nov. 2003.

[107] K. A. Kacprzak, O. Lopez-Acevedo, H. Häkkinen, and H. Grönbeck, "Theoretical characterization of cyclic thiolated copper, silver, and gold clusters," *The Journal of Physical Chemistry C*, vol. 114, no. 32, pp. 13571–13576, 2010.

[108] B. Hammer and J. K. Nørskov, "Why gold is the noblest of all the metals," *Nature*, vol. 376, pp. 238–240, July 1995.

[109] D. M. Newns, "Self-consistent model of hydrogen chemisorption," *Phys. Rev.*, vol. 178, pp. 1123–1135, Feb 1969.

[110] T. B. Grimley, "Overlap effects in the theory of adsorption using Anderson's Hamiltonian," *Journal of Physics C: Solid State Physics*, vol. 3, pp. 1934–1942, Sept. 1970.

[111] K. S. Thygesen, "Electron transport through an interacting region: The case of a nonorthogonal basis set," *Phys. Rev. B*, vol. 73, p. 035309, Jan 2006.

[112] J. K. Nørskov, A. Houmøller, P. K. Johansson, and B. I. Lundqvist, "Adsorption and Dissociation of H_2 on Mg Surfaces," *Physical Review Letters*, vol. 46, pp. 257–260, Jan. 1981.

[113] K. W. Jacobsen, J. K. Nørskov, and M. J. Puska, "Interatomic interactions in the effective-medium theory," *Phys. Rev. B*, vol. 35, pp. 7423–7442, May 1987.

[114] K. W. Jacobsen, P. Stoltze, and J. K. Nørskov, "A semi-empirical effective medium theory for metals and alloys," *Surface Science*, vol. 366, no. 2, pp. 394 – 402, 1996.

[115] `https://wiki.fysik.dtu.dk/asap`.

[116] Y. Wang, S. Teitel, and C. Dellago, "Melting and equilibrium shape of icosahedral gold nanoparticles," *Chemical Physics Letters*, vol. 394, pp. 257–261, Aug. 2004.

[117] J. Li, X. Li, H. Zhai, and L. Wang, "Au20: A tetrahedral cluster," *Science*, vol. 299, pp. 864 –867, Feb. 2003.

[118] E. S. Kryachko and F. Remacle, "The magic gold cluster Au20," *International Journal of Quantum Chemistry*, vol. 107, pp. 2922–2934, Jan. 2007.

[119] O. B. Christensen, K. W. Jacobsen, J. K. Nørskov, and M. Manninen, "Cu cluster shell structure at elevated temperatures," *Phys. Rev. Lett.*, vol. 66, pp. 2219–2222, Apr 1991.

[120] O. B. Christensen and K. W. Jacobsen, "The coupling between atomic and electronic structure in small Cu clusters," *Journal of Physics: Condensed Matter*, vol. 5, pp. 5591–5602, Aug. 1993.

[121] H. Häkkinen and M. Manninen, "Electronic-structure-induced deformations of liquid metal clusters," *Phys. Rev. B*, vol. 52, pp. 1540–1543, Jul 1995.

[122] R. G. Pearson, "The principle of maximum hardness," *Accounts of Chemical Research*, vol. 26, pp. 250–255, May 1993.

[123] M. K. Harbola, "Magic numbers for metallic clusters and the principle of maximum hardness," *Proceedings of the National Academy of Sciences*, vol. 89, pp. 1036 –1039, Feb. 1992.

[124] M. Manninen, J. Mansikka-aho, H. Nishioka, and Y. Takahashi, "Odd-even staggering in simple models of metal clusters," *Zeitschrift für Physik D Atoms, Molecules and Clusters*, vol. 31, pp. 259–267, Dec. 1994.

[125] H. Grönbeck and A. Rosén, "Analysis of the odd-even alternation in simple metal clusters," *Zeitschrift für Physik D Atoms, Molecules and Clusters*, vol. 36, pp. 153–157, 1996. 10.1007/BF01426630.

[126] E. M. Fernández, P. Ordejón, and L. C. Balbás, "Theoretical study of O_2 and CO adsorption on Au_n clusters (n = 5–10)," *Chemical Physics Letters*, vol. 408, pp. 252–257, June 2005.

[127] N. S. Phala, G. Klatt, and E. van Steen, "A dft study of hydrogen and carbon monoxide chemisorption onto small gold clusters," *Chemical Physics Letters*, vol. 395, no. 1-3, pp. 33 – 37, 2004.

[128] S. Klacar, A. Hellman, I. Panas, and H. Grönbeck, "Oxidation of small silver clusters: A density functional theory study," *The Journal of Physical Chemistry C*, vol. 114, no. 29, pp. 12610–12617, 2010.